Laser annealing irradiated silicon single-photon avalanche photodiodes for quantum satellite receiver

by

Jin Gyu Lim

A thesis
presented to the University of Waterloo
in fulfillment of the
thesis requirement for the degree of
Masters of Applied Science
in
Electrical and Computer Engineering

Waterloo, Ontario, Canada, 2018

This thesis consists of material all of which I authored or co-authored: see Statement of Contributions included in the thesis. This is a true copy of the thesis, including any required final revisions, as accepted by my examiners.

I understand that my thesis may be made electronically available to the public.

Statement of Contributions

Chapter 6 is based on an appendix of a publication [107] I co-authored. I performed the theoretical analysis for the appendix using data from [70] and wrote it with contribution from Prof. Vadim Makarov.

Section 4.4.4 and Chapter 7 are based on a publication [111] I co-authored. I performed the experiments, conducted data analysis, and wrote the manuscript with contributions from all authors. Dr. Elena Anisimova, Dr. Brendon L. Higgins, Dr. Jean-Philippe Bourgoin, Prof. Thomas Jennewein, and Prof. Vadim Makarov provided the samples and assisted with experimental setup and data analysis.

For the rest of the chapters, I declare that I am the sole author of them.

Abstract

Single-photon avalanche photodiodes (SPADs) are a practical option for space-based quantum communications requiring single-photon detection. However, radiation damage to SPADs significantly increases their dark count rates and thus reduces their useful lifetimes in orbit.

For Space-QUEST experiment, I analyzed the feasibility of using silicon SPADs inside the International Space Station for a 1-year mission. Adding a 1-year contingency margin and taking sample variations into account, Excelitas SLiK SPADs need to be cooled down to $-45\,^{\circ}\mathrm{C}$ and Excelitas C309021SH $-65\,^{\circ}\mathrm{C}$ to guarantee the dark count rate below 2000 Hz.

In the first round of laser annealing tests, we show that high-power laser annealing of irradiated SPADs of three different models (Excelitas C30902SH, Excelitas SLiK, and Laser Components SAP500S2) heals the radiation damage and several SPADs are restored to typical pre-radiation dark count rates. Of nine samples we test, six SPADs were thermally annealed in a previous experiment as another solution to mitigate the radiation damage. Laser annealing reduces the dark count rates further in all samples with the maximum dark count rate reduction factor varying between 5.3 and 758, depending on the sample and the radiation dose, when operating at $-80\,^{\circ}\mathrm{C}$. This indicates that laser annealing is a more effective method than thermal annealing. The illumination power to reach these reduction factors ranges between $0.8-1.6\,\mathrm{W}$. Other photon detection characteristics, such as photon detection efficiency, timing jitter, and afterpulsing probability, fluctuate but they are not sufficient enough to impact the overall performance of quantum communications. These results herald a promising method to extend the lifetime of a quantum satellite equipped with SPADs.

We then perform the second round of laser annealing tests. This starts off with radiation simulation to determine radiation dosages of different lifetimes in space for radiation test performed on Laser Components SAP300s. After proton irradiation, the samples from each damage group are laser-annealed using the same method in the first round of laser annealing tests (60 s continuous exposure) and the results show that they all recover the dark count rate close to the pre-radiation values at $22\,^{\circ}\mathrm{C}$. The optical power to achieve such reduction is between $800-1000\,\mathrm{mW}$. In addition, we explored new laser annealing

methods in order to learn about the causes of the laser annealing effect. We show that the 180 s continuous exposure and 50% duty cycle method for 60 s exposure can also return the dark count rate to pre-radiation levels when the average illumination power is between 800−1000 mW. These results imply that the thermal effect is the main contributor of laser annealing. However, we also show that forward-bias current annealing on one sample and its dark count rate drops at a much faster rate per power deposition than other laser annealing methods. As a result, more tests need to be done to investigate the causes of the laser annealing effect further. Furthermore, we find that the improvement from laser annealing is permanent.

Acknowledgements

I would like to thank Prof. Vadim Makarov for teaching me every aspect of research and providing helpful advice. I learned a lot over 3.5 years. I would also like to thank Prof. Thomas Jennewein for having discussions and giving me opportunities to participate in the QEYSSat project. I also thank Prof. Michal Bajcsy for being my co-supervisor, for reviewing this Thesis and providing feedback on my seminar, and for all administrative work for smooth change of supervisor. I extend my thanks to Prof. Alexander Ling from the National University of Singapore for offering collaboration and for being patient with my progress. I would like to thank Prof. Na Young Kim for reviewing my Thesis and attending my seminar and Prof. Catherine Gebotys for agreeing to examine the Thesis.

I would like to thank all group members of Quantum Hacking Lab. I thank Jean-Philippe Bourgoin for all the planning of our research trips, taking care of me between shifts, helping me move my experimental setup, for his excellent thesis template that has made my job a lot easier, and for comments on my Thesis. I think my research planning skills improved a lot after working with you. I also thank Brendon L. Higgins for helping me set up the data acquisition system for my experiments and for meticulous editing of my manuscript. I will try to follow your editing procedures for any future publications.

Last but not the least, I would like to thank my family, especially Mom and sister, for unconditional support that helped me finish this degree. I would not have been able to complete this without them. I also thank *Ahjumma* and *Soo-Dol* for looking out for me.

Dedication

For Mom and my future...

Table of Contents

List of Tables

List of Figures

List of Abbreviations

DCR Dark Count Rate 55, 81, 82, 86

DDD Displacement Damage Dose 41, 42, 56, 57

IQC Institute for Quantum Computing 45

ISS International Space Station 43, 44, 53, 55, 56, 59, 97

NUS National University of Singapore 43, 45, 48, 78, 93

PQC Post-Quantum Cryptography 2, 3

QBER Quantum Bit Error Rate 15, 18, 19, 21, 25–27, 69

QEYSSat Quantum Encryption and Science Satellite 43–45, 53

QKD Quantum Key Distribution 2–6, 8–11, 13, 15, 18–22, 25–30, 69, 75

SPAD Single-Photon Avalanche photoDiode 4, 15, 16, 28, 30–33, 35–41, 43, 45, 48, 53, 55, 57–59, 61, 63, 65–69, 71, 74, 75, 90, 97, 98, 113, 115

Chapter 1

Introduction

As the Information Age is progressing, we need to transfer more and more information through the Internet and between mobile devices. As a result, we have to develop faster processors and communication systems. Gordon Moore [1] projected that the number of transistors on an integrated chip would double every two years, thereby increasing the processor speed. Creating more dense chips leads to the development of smaller transistors, but there is a fundamental limit to how small a traditional metal-oxide-semiconductor field-effect transistor can be [2]. Thus, researchers are exploring alternative designs as we are headed for the limit. Another solution of increasing the processing speed is to develop quantum computers. Richard Feynman in 1982 [3] came up with the idea of using the advantages of quantum mechanics to create a computer. Our modern communication systems and computers use logical bits '0' and '1'. A logical bit is deterministic so it has to be either '0' or '1'. However, a quantum bit, or *qubit*, has the property of *superposition* that makes the qubit probabilistic, that is, it is p percent '0' and (1-p) percent '1', where p is controllable. Using this superposition principle, n qubits represent information equivalent to 2^n classical bits. Thus, the quantum computer can outperform the modern classical computer when a quantum processor with a sufficient number of qubits is developed.

The quantum computer gained a global attention when Peter Shor, then at Bell Labs, developed a quantum algorithm that can factor out a product of two very large prime numbers and solve discrete logarithm problems [4]. Unfortunately, current public-key cryptographic protocols, such as RSA [5], Diffie-Hellman [6], and elliptical curve [7, 8] encryption schemes, can be easily and completely broken by Shor's algorithm if we have a quantum computer now. This is a big problem because the security of every application or system – including online banking and shopping, e-mails, ATM, text-messages, and etc. – that relies on the aforementioned public-key encryption systems is in jeopardy. On the other hand,

Grover's search quantum algorithm [9] can be used to attack symmetric key encryption systems. The algorithm is capable of finding a solution from 2^n samples with a high probability by iterating it at most $2^{\frac{n}{2}}$ times. For example, Grover's algorithm can be executed at most 2^{64} times to find the secret key for AES-128 [10], reducing the security measure by half. Dr. Michele Mosca postulated a theorem to raise awareness of these security threats [11]. According to the theorem, let x be the number of years the cryptographic keys need to remain secure. Let y be the number of years to update current infrastructure or deploy new systems to achieve quantum-safe network. Let z be the number of years it takes to develop the quantum computer that breaks the security. If $x + y > z$, we need to worry because information can no longer be protected for the promised x years. Therefore, we need to come up with quantum-safe solutions that can be deployed soon.

Post-Quantum Cryptography (PQC) and Quantum Key Distribution (QKD) [12, 13] are two quantum-safe solutions. PQC is improved upon current classical cryptography. RSA [5], Diffie-Hellman [6], and elliptical curve [7, 8] public-key encryption schemes can be replaced by lattice-based (i.e. learning with errors [14]), multivariate [15, 16], or isogenies [17] public-key encryption systems. Symmetric key encryption systems, such as AES, need to double the key size to remain secure against quantum attacks, such as Grover's algorithm. PQC schemes are easy to deploy on the current infrastructure as they are simply computer algorithms. They are efficient because the key size does not need to be as long as the message. However, PQC does not have any security proofs, so there may be a loophole to break these new PQC schemes. Historically, cryptanalysis was able to defeat many cryptosystems [18]. On the other hand, QKD guarantees unconditional security based on quantum physics. In QKD, a communicating party (Alice) uses a random sequence of bits to encode a series of qubits by two randomly selected orthogonal bases with equal probability. She then sends the qubits to the other communicating party (Bob). During the transmission, the eavesdropper cannot completely copy the transmitted qubits due to *no-cloning theorem* [19] and she cannot determine which basis was used to encode each qubit due to *Heisenberg's uncertainty theorem* [20]. When the eavesdropper attempts to perform either copying or measuring of qubits, she can introduce errors in the received qubits, revealing her presence. After two communication parties extract a shared, secret key from qubits, they perform *one-time pad* encryption, which is the only secure encryption method proven by Claude Shannon [21], or other symmetric key encryption schemes. Drawbacks of one-time pad encryption scheme are that the key size must be as long as the message itself and the key must be used only once, so it is not as efficient as PQC counterparts. Other symmetric key encryption schemes can give up some security for improved efficiency while security confidence is still better than PQC. A disadvantage of QKD is that the

QKD network requires additional infrastructure. Therefore, the main trade-off between PQC and QKD is the security confidence and cost.

There are great efforts to build global QKD networks. Visible to near-infrared single-photons are used as qubits for the speed at which information is carried between two communicating parties, for long enough coherence time to preserve the encoded states during transmission, and for the availability of low-loss channels. Optical fibre-based [22–24] and quantum satellite-based [25, 26] networks are two potential solutions researchers are pursuing for a global connection. The optical fibre-based network has an advantage of using optical fibres already installed for classical communications links. However, the optical fibre has a relatively high intrinsic loss, limiting the distance for a single link for QKD. In addition, if the quantum channel is multiplexed with other classical channels, the quantum signals are buried in noise caused by Raman scattering. Thus, the development of the *quantum repeater* [27] and multiplexing methods are inevitable to establish a global network. Unfortunately, inventing the quantum repeater is as difficult and challenging as creating the quantum computer, so it is not a viable option for a global connection yet. However, Europe [28], China [29], Korea [30], Japan [31], U.K. [32], Switzerland [33], and U.S. [34–36] have built or are building metropolitan or nation-wide optical-fibre-based quantum networks. On the other hand, the quantum satellite in low-Earth-orbit is a feasible technology today for a global QKD network because the satellite technology is mature and because the free-space link is mostly in vacuum. The geometric loss of the free-space link grows quadratically with distance, while the optical fibre's absorption loss grows exponentially with distance. Various feasibility studies [37–41], ground tests [42–49], ground-to-air [50–52] and ground-to-satellite experiments [53–61] were performed by researchers from China, Germany, Austria, U.S., Canada, Japan, Italy, U.K., and Singapore. China successfully launched a quantum satellite in 2016 and proved that satellite-based QKD is indeed feasible [61]. In addition, China also showed that ground-to-satellite Bell's inequality test (via entangled photons) [62] and quantum teleportation experiment [63] are successful. These results are significant because more satellites can be launched into space to form a satellite constellation, and Bell's inequality test and quantum teleportation can help us establish the global-scale quantum Internet.

For ground-to-satellite quantum communications, the satellite can be designed as either a transmitter or a receiver. For instance, China launched its satellite as a transmitter and Canada is building it as a receiver [64]. Both designs have advantages and disadvantages but for building a quantum satellite network, it is necessary to research on both designs for inter-satellite communications. An external factor that needs to be considered for building a receiver satellite is radiation damage in low-Earth-orbit. The most popular single-photon

detector for free-space link is silicon Single-Photon Avalanche photoDiode (SPAD) for its high efficiency, its spectral response curve overlapping with the transmission window in the atmosphere, and no need for cryogenic cooling. However, studies [65, 66] show that proton radiation damages on silicon SPAD result in a significant increase in the background noise. When the noise exceeds a certain threshold, it is not possible to perform quantum communications protocols [67]. Thus, the satellite lifetime is limited by how long the noise can stay below the threshold. For radiation damage mitigation, metal shielding can block protons to slow down the damaging process and heating up silicon SPAD with its built-in thermoelectric cooler (TEC) can anneal silicon lattice and thus reduce the background noise [68–70]. Other alternatives that can suppress the noise further can prolong the lifetime of the quantum satellite.

In this thesis I present experimental investigations of the effects of high-power laser annealing on irradiated silicon SPADs as a solution to proton radiation damage mitigation. The samples were irradiated by 106 MeV protons with various fluences to simulate different lifetimes in space. Some of these samples were previously thermally annealed in another experiment [70], so the first round of laser annealing experiment focused on whether laser annealing is effective on decreasing the background noise and whether laser annealing can reduce the noise further after thermal annealing. The second round of laser annealing experiment performed a full cycle of radiation simulation, radiation test, and laser annealing procedure to directly check whether the background noise is returned to the pre-radiation values. Then, we attempted to explore the causes of the laser annealing effect with respect to the peak temperature produced on irradiated silicon SPAD, total exposure energy, and excess carrier flow. To investigate the excess carrier flow further, forward-bias current annealing was performed on one sample. Lastly, three samples were characterized for 58−59 hours after each laser annealing power to verify whether the effect is permanent. Before delving into the experimental results in Chapter 6-8, background information is explained throughout Chapter 2-5.

Chapter 2 goes over three quantum communications protocols: Bell's inequality test, quantum teleportation, and QKD. Chapter 3 goes over the history of free-space QKD experiments that led up to the launch of the quantum satellite. Chapter 4 illustrates how a silicon SPAD and various quenching circuits operate, while Chapter 5 discusses radiation damage in space, how to calculate it, and radiation test results on silicon SPADs. Chapter 6 analyzes the feasibility of using silicon SPADs insde the International Space Station for Space-QUEST experiment based on the radiation test results from Chapter 5. Chapter 7 and 8 show experimental results and the analysis of laser annealing of irradiated silicon SPADs. I conclude in Chapter 9.

Chapter 2

Quantum Communications

2.1 Introduction

Quantum communications may replace the current communications network backbone for unconditional security. Bell's inequality test, quantum teleportation, and Quantum Key Distribution (QKD) are three important quantum communication primitives for establishing a quantum network. Bell's inequality test [71–73] experimentally verifies the validity of entangled photon pairs that can be used for quantum teleportation and entanglement-based QKD. Using the entangled pairs, quantum teleportation [74] sends an unknown state from one place to another. This protocol is imperative for the development of the quantum Internet. QKD ensures the generation of unconditionally secure key for encrypting confidential messages and there are two different implementation styles [12, 13]. These three quantum communications protocols are explained further in the following sections.

2.2 Bell's inequality test

In 1935, Albert Einstein, Boris Podolsky, and Nathan Rosen's thought experiment [75] demonstrated through *quantum entanglement*[1] that the quantum mechanics theory is incomplete, if explained by a classical physics theory. They concluded that there should be *local hidden variables theory* to complete it. However, Bell's theorem [71] mathematically proved that local hidden variables cannot fully explain the quantum mechanics. This

[1] "Quantum entanglement is a quantum mechanical phenomenon in which the quantum states of two or more objects have to be described with reference to each other, even though the individual objects may be spatially separated." [76]

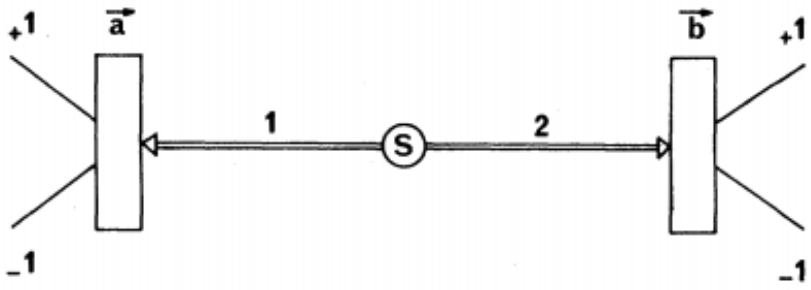

Figure 2.1: **Bell's inequality test experimental setup (Reprinted from [73]).** S is an entangled state $\frac{1}{\sqrt{2}}(|HH\rangle + |VV\rangle)$. $|H\rangle$ ($|V\rangle$) is a horizontally (vertically) polarized single-photon state. a and b are H/V basis polarization beam splitters. a (b) can be rotated by 0° (22.5°) or 45° (67.5°).

means that local realism[2] does not apply to quantum physics at all times, unlike classical physics. John F. Clauser, Michael A. Horne, Abner Shimony, and Richard A. Holt (CHSH) generalized Bell's theorem for an experiment proposal in 1969 [72]. Alan Aspect simplified the experiment further [73] and used Fig. 2.1 to test local hidden variables theory with entangled photons and linear optics.

The goal for this experiment is to calculate the correlation value S (Eq. (2.1)), where a, b, a', b' represent H/V basis polarization beam splitter rotated by 0°, 22.5°, 45°, and 67.5°, respectively, and E(x,y) is a correlation function. (N_{+-} in Eq. (2.2) represents the number of coincident detection events, measuring +1 at a side and −1 at b side[3].) If there are local hidden variables, $|S| \leq 2$ [72]. This inequality was generalized by CHSH from Bell's original inequality. However, entangled pairs violate such inequality, indicating that local hidden variables theory cannot explain the quantum mechanical phenomena. The maximum value each correlation function can obtain is $\frac{1}{\sqrt{2}}$. Thus, the maximum S value is $2\sqrt{2}$, violating $|S| \leq 2$.

$$S = E(a,b) + E(a',b) + E(a',b') - E(a,b') \tag{2.1}$$

$$E(a,b) = \frac{N_{++} + N_{--} - N_{+-} - N_{-+}}{N_{++} + N_{--} + N_{+-} + N_{-+}} \tag{2.2}$$

For quantum communications, entangled photons are required for quantum teleportation and entangled-based QKD protocols. These protocols will fail if the prepared photon

[2]Locality means that two objects that are far apart cannot affect each other instantly, while realism means that an object already has a pre-determined value before a measurement.

[3]+1: horizontal polarization, -1: vertical polarization

pairs are not sufficiently entangled. Therefore, the main purpose of Bell's inequality test in quantum communications applications is to verify the quality of entangled photon sources.

2.3 Quantum teleportation

Quantum teleportation [74] transfers an arbitrary qubit ($|\phi\rangle = \alpha|0\rangle + \beta|1\rangle$) from point A to point B using classical information and pre-shared entangled states between two communicating parties. This quantum communication primitive is crucial in establishing the quantum Internet.

Prior to sending an arbitrary state, the two communicating parties need to share an entangled state $\frac{1}{\sqrt{2}}(|0\rangle_a|0\rangle_b+|1\rangle_a|1\rangle_b)$. Then, Alice prepares an arbitrary state $\alpha|0\rangle_c+\beta|1\rangle_c$ and performs a Bell state measurement[4] with the arbitrary state and a qubit from the entangled pair. Three-qubit state can be written in the following manner:

$$|\psi\rangle = \frac{1}{\sqrt{2}}(\alpha|0\rangle_c + \beta|1\rangle_c)(|0\rangle_a|0\rangle_b + |1\rangle_a|1\rangle_b) \tag{2.3}$$

$$= \frac{1}{\sqrt{2}}(\alpha|0\rangle_c|0\rangle_a|0\rangle_b + \alpha|0\rangle_c|1\rangle_a|1\rangle_b + \beta|1\rangle_c|0\rangle_a|0\rangle_b + \beta|1\rangle_c|1\rangle_a|1\rangle_b) \tag{2.4}$$

$$= \frac{1}{\sqrt{2}}[(\alpha|0\rangle_c|0\rangle_a + \beta|1\rangle_c|0\rangle_a)|0\rangle_b + (\alpha|0\rangle_c|1\rangle_a + \beta|1\rangle_c|1\rangle_a)|1\rangle_b] \tag{2.5}$$

$$= \frac{1}{2}[\alpha(|\phi^+\rangle_{ac} + |\phi^-\rangle_{ac}) + \beta(|\psi^+\rangle_{ac} - |\psi^-\rangle_{ac})]|0\rangle_b \tag{2.6}$$

$$+ \frac{1}{2}[\alpha(|\psi^+\rangle_{ac} + |\psi^-\rangle_{ac}) + \beta(|\phi^+\rangle_{ac} - |\phi^-\rangle_{ac})]|1\rangle_b \tag{2.7}$$

$$= \frac{1}{2}|\phi^+\rangle_{ac}(\alpha|0\rangle_b + \beta|1\rangle_b) + \frac{1}{2}|\phi^-\rangle_{ac}(\alpha|0\rangle_b - \beta|1\rangle_b) \tag{2.8}$$

$$+ \frac{1}{2}|\psi^+\rangle_{ac}(\beta|0\rangle_b + \alpha|1\rangle_b) + \frac{1}{2}|\psi^-\rangle_{ac}(\alpha|1\rangle_b - \beta|0\rangle_b) \tag{2.9}$$

The modified three-qubit state shows that Alice can measure one of four Bell states with equal probability. Depending on the measured Bell state output, the qubit at Bob's side changes into the arbitrary input state with a phase difference and/or flipped states. This state is the same as Alice's input state with $\frac{1}{4}$ probability, so Bob needs to perform simple corrective operations to obtain the same arbitrary state Alice prepared ($\alpha|0\rangle_c + \beta|1\rangle_c$) at all times. The information on the order of and types of operations is sent from Alice via

[4]This measurement can distinguish four Bell states: $|\phi^+\rangle = \frac{1}{\sqrt{2}}(|00\rangle + |11\rangle)$, $|\phi^-\rangle = \frac{1}{\sqrt{2}}(|00\rangle - |11\rangle)$, $|\psi^+\rangle = \frac{1}{\sqrt{2}}(|01\rangle + |10\rangle)$, $|\psi^-\rangle = \frac{1}{\sqrt{2}}(|01\rangle - |10\rangle)$.

a classical channel by monitoring the classical outputs (bit string 'ab') of the Bell state measurement[5]. If a=1 (b=1), Z (X) operation is performed on Bob's qubit.

$$|0\rangle = \begin{bmatrix} 1 \\ 0 \end{bmatrix} \quad |1\rangle = \begin{bmatrix} 0 \\ 1 \end{bmatrix} \quad X = \begin{bmatrix} 0 & 1 \\ 1 & 0 \end{bmatrix} \quad Z = \begin{bmatrix} 1 & 0 \\ 0 & -1 \end{bmatrix}$$

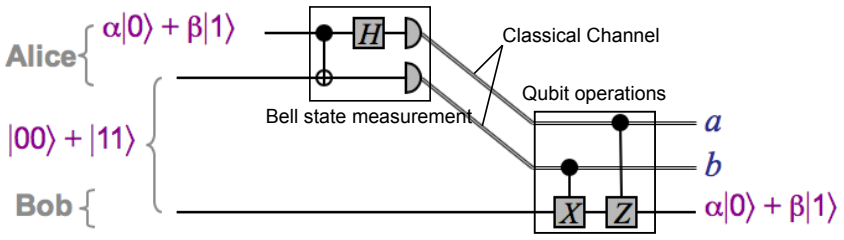

Figure 2.2: **Quantum teleportation (Reprinted from [77]).**

After these operations, Bob's qubit is the same as Alice's input state every time. Figure 2.2 summarizes the procedure.

2.4 Quantum key distribution

Two main categories of QKD schemes are the prepare-and-measure and entanglement-based protocols. For prepare-and-measure protocols, a communicating party (Alice) prepares quantum states and transmits them to the other communicating party (Bob) for measurement. For entanglement-based protocols, a third-party source sends a qubit from entangled pairs to Alice and Bob, and they perform measurements independently on each qubit.

2.4.1 Prepare-and-measure scheme

The very first prepare-and-measure QKD scheme (BB84 [6]) was proposed by Charles Bennett and Gilles Brassard in 1984 [12]. Two communicating parties, Alice and Bob, share a quantum channel for transmitting qubits and an authenticated classical channel[7] for the

[5] $|\phi^+\rangle : 00$, $|\phi^-\rangle : 10$, $|\psi^+\rangle : 01$, $|\psi^-\rangle : 11$

[6] The protocol name, BB84, is named after the first letter of their last names and the year the paper was published.

[7] A secure classical channel established between Alice and Bob. It cannot be tampered with but can still be overheard.

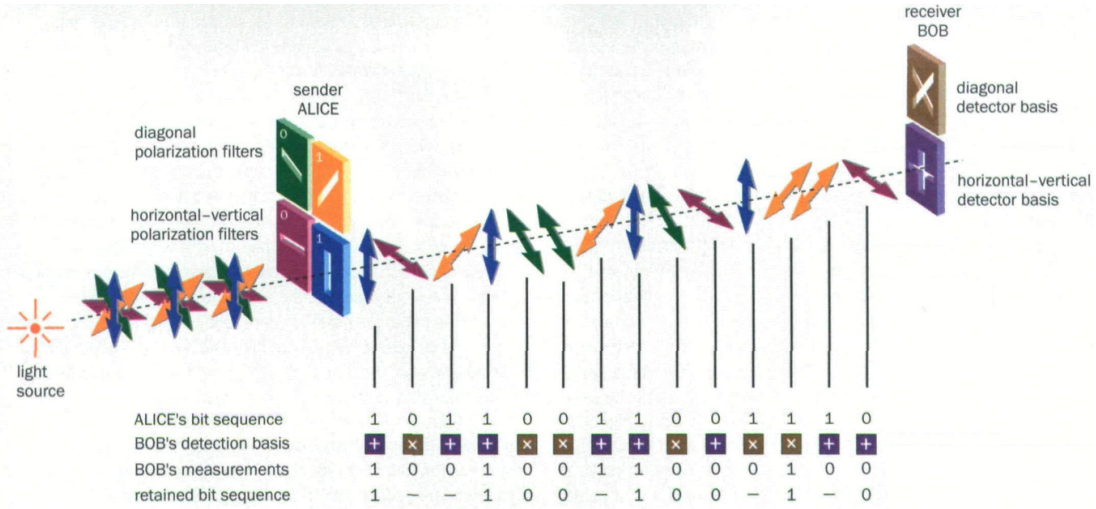

Figure 2.3: **BB84 QKD protocol (Reprinted from [78]).**

public communications needed to extract the final secret key after the key exchange. The 'quantum part' of QKD is therefore only the initial qubit distribution and the following procedures are all performed classically.

The full BB84 QKD protocol works as follows. Alice and Bob use polarized photons for encoding bit '0' and '1', and for security, two non-orthogonal basis are randomly selected for encoding. Rectilinear basis constitutes horizontal (bit '0') and vertical (bit '1') polarizations, while diagonal basis includes $+45°$ (bit '0') and $-45°$ (bit '1') polarizations. Alice randomly and independently selects a bit value and a basis for encoding a photon. The encoded photon is then transmitted in a quantum channel to Bob who randomly chooses either rectilinear or diagonal basis for qubit measurement and records his basis choice and output polarization/bit value. The shared key between Alice and Bob is called *raw key*. After a raw key is established, Alice and Bob each publicly announce via the authenticated classical channel which basis was used to encode and measure each photon. For each bit, Alice and Bob only keep the bits when they used the same basis. The resulting key is called *sifted key*. Subsequently, Alice and Bob reveal a portion of the sifted key for correcting any errors in the remaining key using error correction algorithms. If the error rate exceeds a certain threshold (typically $\leq 11\%$), Alice and Bob abort the operation and start anew. Otherwise, the error-corrected, sifted key is shortened by a hash function to further reduce possible information leakage to the eavesdropper. This process is called *privacy amplification* and the final, shortened key is called *secret key*. Alice and Bob use it to encrypt messages.

The unconditional security of this protocol relies on the *no-cloning theorem* that quan-

tum states cannot be duplicated completely without inducing error. Rectilinear and diagonal basis are not orthogonal, so, for example, if a horizontally polarized photon is measured in the diagonal basis by the eavesdropper, she obtains either $+45°$ or $-45°$ polarization with equal probability. If Bob chooses the rectilinear basis for measuring the resulting photon after the eavesdropper's measurement, he equally likely obtains a horizontally or vertically polarized photon, instead of getting a horizontally polarized photon with 100% probability. This induced error by the eavesdropper informs Alice and Bob of her presence during error correction stage.

2.4.2 Entanglement-based scheme

Prof. Artur Ekert independently invented another QKD scheme in 1991 [13]. This scheme utilizes polarization-entangled photon pairs during qubit distribution stage instead of prepared states at Alice, and extra Bell's inequality test guarantees the unconditionally secure key distribution in addition to no-cloning theorem.

Ekert's QKD scheme utilizes the singlet state[8] and sends each photon to Alice and Bob. Alice and Bob each have independent H/V basis polarization analyzers and they are randomly and independently rotated by $\phi_1^a = 0$, $\phi_2^a = \pi/4$, or $\phi_3^a = \pi/2$ at Alice's side, and by $\phi_1^b = \pi/4$, $\phi_2^b = \pi/2$, or $\phi_3^b = 3\pi/4$ at Bob's. After passing through the analyzers, the input singlet state changes to the following state[9]:

$$\frac{1}{\sqrt{2}}[sin(\phi_a - \phi_b)(|H\rangle_a |H\rangle_b + |V\rangle_a |V\rangle_b) + cos(\phi_a - \phi_b)(|H\rangle_a |V\rangle_b - |V\rangle_a |H\rangle_b)] \quad (2.10)$$

After the qubit distribution phase, Alice and Bob publicly announce selected analyzer rotation for each photon. If the rotation angles are the same[10], Alice and Bob include the bit in the raw key. Bob flips his bit value because the singlet state is anti-correlated. If they selected different angles[11], Alice and Bob also publicly announce the output value (± 1[12]) to calculate the correlation value (S) for Bell's inequality.

[8] $\frac{1}{\sqrt{2}}(|H\rangle_a |V\rangle_b - |V\rangle_a |H\rangle_b) = \frac{1}{\sqrt{2}}(|D\rangle_a |A\rangle_b - |A\rangle_a |D\rangle_b)$, $|D\rangle = |+45°\rangle, |A\rangle = |-45°\rangle$

[9] If Alice and Bob use the same analyzer, they will always get anti-correlated measurement values. Otherwise, they get correlated values with the probability of $\frac{|sin(\phi_a - \phi_b)|^2}{2}$ and anti-correlated values with the probability of $\frac{|cos(\phi_a - \phi_b)|^2}{2}$.

[10] (ϕ_2^a, ϕ_1^b), (ϕ_3^a, ϕ_2^b)

[11] (ϕ_1^a, ϕ_1^b), (ϕ_1^a, ϕ_3^b), (ϕ_3^a, ϕ_1^b), (ϕ_3^a, ϕ_3^b)

[12] +1: horizontal polarization, -1: vertical polarization

If the Bell's inequality is violated, Alice and Bob can confirm that the received photons were entangled. Furthermore, they can confirm that there was no eavesdropper in the quantum channel because, for the eavesdropper to gain information, she needs to measure the incoming photons and send new photons to Alice and Bob. However, measuring a photon of an entangled pair breaks entanglement, causing the Bell's inequality test to fail. Therefore, the Bell's inequality test adds the security verification to entanglement-based QKD. The subsequent error correction and privacy amplification processes are the same as the prepare-and-measure scheme.

2.5 Conclusion

Since the security threat for classical encryption algorithms due to the development of the quantum computer is a major issue and Bell's inequality test and quantum teleportation can be tested on QKD infrastructure, quantum communications applications focus more on QKD. The ultimate goal for researchers around the world is to build the global-scale quantum communications network to provide quantum-safe solutions everywhere. Fibre optics and free-space paths are two quantum channels for photons. Fibre optics have much higher intrinsic loss and quantum repeaters [27] are still in the development phase. Constructing a quantum satellite is another solution for the global connection. This technology is feasible as China recently launched a quantum satellite and successfully demonstrated the operation of Bell's inequality test [62], quantum teleportation [63], and QKD [61] with ground stations over >1000 km apart. The next chapter describes how initial 32 cm long free-space QKD experiment [79] advanced to the operation of a quantum communications satellite.

Chapter 3

Quantum Satellite

3.1 Introduction

The first full BB84 experiment was implemented in 1992 by Bennett *et al.* [79] over 32 cm free-space channel using polarization encoding. This proved that implementing Quantum Key Distribution (QKD) is not an unrealistic task and started to attract researchers to the field of QKD. In this chapter, I begin with early free-space experiments following [79], some of which already suggested a ground-to-satellite network for a global QKD connection. Following these recommendations, several groups around the world conducted detailed theoretical feasibility studies of quantum satellite [37–41]. Researchers also improved optical and other processing systems to extend the working distance to over 100 km for Bell's inequality test, quantum teleportation, and QKD [42–49]. Next, airplanes, a hot air balloon as a mock-up satellite, and retro-reflectors on satellites were used to experimentally verify the feasibility of ground-to-air/ground-to-satellite QKD with a moving object [50–52, 54–56, 58, 59]. Finally, Chinese research groups confirmed that ground-to-satellite quantum communications are indeed possible with their quantum satellite [61–63].

3.2 Initial free-space QKD experiments

Six research papers [25, 26, 80–83] published after the free-space QKD experiment by Bennett *et al.* [79] gradually improved the QKD systems to transmit photons over longer distances and some of these mentioned the possibility of a ground-to-satellite connection for QKD. Table 3.1 summarizes the results from the papers.

Table 3.1: **Summary of six early free-space QKD experiments and their performance.** For QKD distance, if a cell has only 1 value, it means that distance applies to both daytime and nighttime. Noise filtering refers to filtering of background photons from the Earth, Sun, and moon. TX: Transmitter, RX: Receiver, P2P: point-to-point, G2S: ground-to-satellite, QBER: quantum bit error rate, JHU: Johns Hopkins University, LANL: Los Alamos National Laboratory, LMU: Ludwig-Maximilian University.

	[80]	[25]	[26]	[81]	[82]	[83]
Year	1996	1998	1999	2000	2002	2002
Protocol	BB84	B92	B92	B92	BB84	BB84
TX & RX locations	Collocation	Collocation	P2P	P2P	P2P	P2P
Noise filtering	spectral, spatial, temporal	spectral, spatial, temporal	spectral, spatial, temporal	spectral, spatial, temporal	spectral, spatial, temporal	spectral, spatial
Distance (day/night)	75 m/150 m	-/950 m	0.5 km	1.6 km/-	10 km	-/23.4 km
Raw key rate	-	50 Hz	50000 detection events	-	1349 Hz (daylight)	1.5−2 kHz
Secret key rate	1 kHz	-	-	3 kHz	264 Hz (daylight)	few hundred Hz
QBER	2%	1.5%	0.4%	5.3%	3.2%	<5%
G2S QKD feasibility prediction?	No	Yes	Yes	No	No	Yes
Research Institute	JHU	LANL	LANL	LANL	LANL	LMU

Based on their results, W. T. Buttler *et al.* [25] and R. J. Hughes *et al.* [26] from Los Alamos National Laboratory estimated Quantum Bit Error Rate (QBER)[1] in nighttime and daytime between a ground station and a satellite at 300 km altitude. They predicted that ground-to-satellite QKD would be feasible at nighttime and maybe even in daylight if a very narrow spectral filter is employed. In addition, if the ground station is configured as a transmitter, they predicted the generation of a raw key rate of 250 Hz with a 10 MHz source.

C. Kurtsiefer *et al.* [83] from Ludwig-Maximilian University also predicted the possibility of ground-to-satellite QKD. Their QKD system could handle up to 27 dB in poor visibility. They estimated that if the receiver efficiency increases from 15%, the system could tolerate loss greater than 33 dB. At this loss, the authors believed that ground-to-satellite QKD in the range of 500−1000 km is feasible.

3.3 Feasibility studies

After the early free-space QKD experiments, a few theoretical studies [37–41] on the feasibility of quantum communication with satellites were published. The studies relied on simulations and the main focuses of them were atmospheric transmission window selection, satellite configurations, signal wavelength selection, and link attenuation analysis.

Atmospheric transmission window selection depends on atmospheric absorption and turbulence, diffraction, and commercially available lasers and single-photon detectors. Atmospheric absorption is caused by various molecules, such as Ozone, carbon dioxide, and water, blocking radiation at various wavelengths. The atmospheric transmission window of our interest is between 400−1600 nm because the only commercially available single-photon detectors for quantum communications are silicon-based and InGaAs/InP-based Single-Photon Avalanche photoDiode (SPAD), photomultiplier tubes and single-photon superconducting nanowires. Silicon-based SPADs are sensitive at 400−1100 nm, while InGaAs/InP-based SPADs and superconducting nanowire detectors are suitable for 1300−1600 nm [84, 85]. Photomultiplier tubes are sensitive in the visible to near-infrared range. Figure 3.1 shows the atmospheric transmission window of our interest and that choosing higher wavelength can reduce atmospheric absorption [41].

Currently, the performance of single-photon detectors narrows down the transmission window even further. InGaAs/InP-based SPADs have ∼10% efficiency and a high dark count rate (false photon counts) for 1300−1500 nm [84–86]. Superconducting nanowires

[1] QBER needs to be ≤11%.

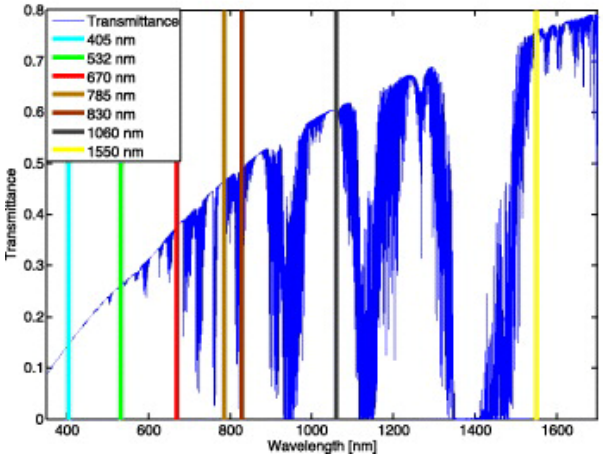

Figure 3.1: **Atmospheric transmission window (Reprinted from [41]).** Coloured vertical lines show a few selections of commercially available laser wavelengths.

have higher efficiency but they require cryogenic cooling, making it difficult to equip them on satellites. Photomultiplier tubes have 10−40% photon detection efficiency in the visible-near-infrared range , while thick-junction silicon SPADs have peak photon detection efficiency of 50−70% between 600−800 nm and a very low dark count rate. Silicon SPADs have the best performance, do not need cryogenic cooling, and are reliable, so these feasibility studies [37–41] all selected the signal wavelength between 600−800 nm and used photon detection efficiency and dark count rate of silicon SPADs in their calculations.

Atmospheric turbulence occurs in the lower 20 km of the atmosphere and is caused by the change in the refractive index due to temperature variations [41]. It leads to beam wandering and broadening, and scintillation. These effects can be reduced at higher signal wavelength [39–41]. Fortunately, turbulence does not affect polarizations [87].

Diffraction also contributes to transmission loss. It depends on the signal wavelength, transmitter telescope size, and the link distance [41], because the loss comes from the receiver telescope missing a portion of the incoming beam. Thus, to reduce diffraction-induced loss, either the diffraction angle should be minimized or the receiver telescope size increased. Following the diffraction equation (Eq. (3.1)), where D_T is the transmitter telescope aperture size, the angle can be reduced if either the wavelength is decreased or the transmitter telescope size is increased.

$$D_T sin(\theta) = \lambda \tag{3.1}$$

Transmittance due to diffraction in far field can also be roughly estimated using Eq. (3.2),

given that the transmitter telescope is diffraction-limited and that the transmitter and receiver telescopes are perfectly aligned and have no intrinsic losses [39].

$$T_{diffraction} \approx \frac{D_T^2 D_R^2}{L^2 \lambda^2} \tag{3.2}$$

The telescope apertures at both ends and signal wavelength can be optimized to compensate for the loss, but its gain is limited because satellites have mass restrictions, limiting the telescope sizes.

In summary, a longer wavelength would decrease losses from atmospheric absorption and turbulence, while shorter wavelength compensates for diffraction loss. This becomes important when choosing the signal wavelength in the $600-800\,\text{nm}$ range for different satellite configurations.

Two satellite configurations are possible for space-based quantum communications [38, 41]:

1. Ground station: signal encoding. Satellite: state analyzer and single-photon detectors. (*Uplink*)

2. Ground station: state analyzer and single-photon detectors. Satellite: signal encoding (*Downlink*)

Uplink and *downlink* configurations utilize one-way communication scheme, so the transmitter prepares either weak-coherent-pulses[2] or single photons. An advantage of the uplink setup is that the source type can be easily swapped for different experiments while the advantage of the downlink is faster key rate due to lower link loss.

Each configuration has a different main source of loss. For uplink transmission, atmospheric turbulence loss dominates over diffraction loss because the optical signals transmitted from a ground station encounter atmospheric turbulence in the first $20\,\text{km}$ so the divergence angle is larger than that from diffraction. Figure 3.2 shows that turbulence is the main source of loss for uplink transmission because increasing the transmitter telescope size beyond $40\,\text{cm}$ does not improve the link attenuation. It contradicts Eq. (3.2) and thus implies that diffraction is not the dominating factor. Since turbulence is the major source of loss, a longer signal wavelength is preferred.

For downlink transmission, diffraction is the main source of loss. Signals are affected by atmospheric turbulence in the last $20\,\text{km}$ of the optical path, which is less than 10%

[2]Highly attenuated coherent light pulses such that the number of photons per pulse follows the Poisson distribution.

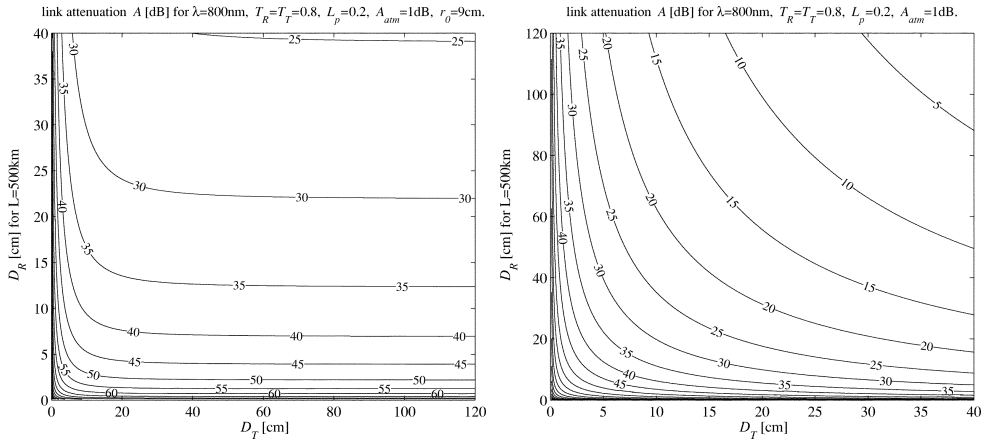

Figure 3.2: **Transmission link attenuation (Reprinted from [39]).** Left: uplink transmission, Right: downlink transmission. Signal wavelength is 800 nm. D_T: transmitter telescope aperture, D_R: receiver telescope aperture, T_T: transmitter telescope transmission factor, T_R: receiver telescope transmission factor, L_p: pointing loss, r_o: Fried parameter. The Fried parameter is used only for uplink transmission to estimate the effect of atmospheric turbulence over the entire optical path [40].

of the entire length. Thus, atmospheric turbulence causes less significant divergence. Figure 3.2 shows that increasing the transmitter telescope size does improve the transmission efficiency, indicating that diffraction is the major problem. A shorter signal wavelength should be selected for the downlink transmission to reduce the diffraction angle.

The factors that contribute to the overall communication loss are taken into account for link analysis. For the analysis, the telescope size equipped on a satellite is assumed to be 10 cm diameter, while that for the ground station is selected to be 30 cm diameter for uplink and 1 m diameter for downlink [38]. Using 650 nm signal wavelength and weak-coherent-pulses, the link attenuation for 1000 km is 34 dB for uplink and 24 dB for downlink. As a result, the downlink QKD can share a raw key at a faster rate than the uplink [37–39, 41].

3.4 Impact of dark counts on quantum communications

The goal for ground-to-satellite QKD is to extract a secret key over a single pass (∼300 s) [39]. The asymptotic secret key rate depends on the transmission loss, alignment error, single-photon sources, QBER, single-photon detectors' efficiencies, and its dark counts [47]. To overcome the overall transmission loss, a faster source clock rate and a higher detection timing resolution could be implemented. For a longer secret key generation per pass, it is also important to have low QBER not to waste many keys during the error

Table 3.2: **Effect of higher dark counts in the detectors on the key generation and on the maximum distances of fundamental experiments.** Wavelength 785 nm, 50 cm transmitter and a 30 cm receiver. Orbit 600 km, pointing error 2 µrad and rural atmosphere (5 km visibility) at sea level. Source rate: 300 MHz for weak-coherent-pulses (WCP) and 100 MHz for entangled photon source; detection time window: 0.5 ns. Table and caption are reprinted from [41].

Detector dark (cps)	WCP source key (Mbit per month)	Entangled source key (Mbit per month)	Max. Bell test distance (km)	Max. teleportation distance (km)
20	3.222	0.440	1359	683
100	3.109	0.426	1283	660
1000	2.292	0.322	1039	0
10000	0	0.012	660	0

correction stage and not to exceed the operation abortion threshold of 11%. In practice, a lower QBER threshold value could be used if the operators know the possible ranges of QBER fluctuations with the absence of the eavesdropper. Dark counts occur randomly, so as shown in Table 3.1, a narrow detection window (∼1 ns) could be applied only when incoming single photons are anticipated to decrease the chance of measuring an erroneous value in the window. The dark counts play a critical role in a QBER calculation. If they increase, QBER can also increase. Thus, it is important to analyze how high dark counts can degrade the performance of QKD.

Table 3.2 from Bourgoin *et al.* [41] shows how high dark counts impact the secret key generation rate for QKD and the maximum operational distances for Bell's inequality test and quantum teleportation. QKD with weak-coherent-pulses can produce a secret key for dark counts up to ∼1000 cps, while QKD with entangled photons and Bell's inequality tests can operate up to 10 000 cps dark counts with reduced performance. Quantum teleportation can work with dark counts up to ∼100 cps. Therefore, selecting single-photon detectors with very low dark counts and high efficiency is as important as optimizing equipment choices for link analysis of ground-to-satellite quantum communication channel. This analysis becomes important in Chapter 5.

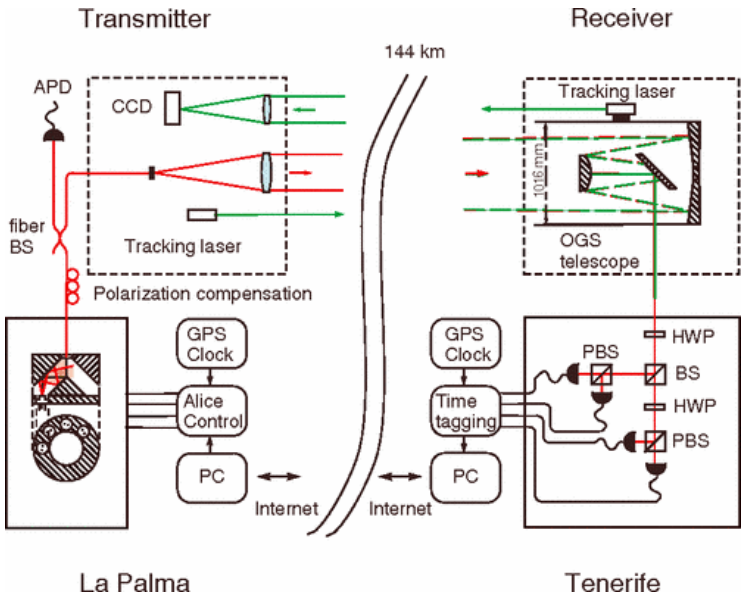

Figure 3.3: **Experimental setup for free-space QKD over 144 km (Reprinted from [42]).** Polarization encoding is used for this experiment, so each of four laser produces horizontal, vertical +45°, and −45°. The pulses are coupled into a single-mode fibre and then collimated at the exit of the telescope. Decoy states are generated by randomly selecting two laser diodes. The pulse width is 2 ns with the repetition rate of 10 MHz. 850 nm wavelength is chosen. The receiver uses a passive basis choice BB84 polarization analyzer. The half-wave plate before the analyzer is placed to compensate for any polarization rotation in the receiver telescope. For pointing and tracking system, two-way beacon lasers are monitored on charged-coupled device cameras to optimize the link efficiency. For time synchronization, the transmitter clock signal is synchronized with the receiver's to perform sifting. 10 Mbps Internet was used as a classical channel.

3.5 Ground-based experiments

Researchers in Europe performed free-space QKD using weak-coherent-pulses and entanglement sharing over 144 km between the Canary Islands of La Palma and Tenerife [42, 43]. The atmospheric distance for this link is longer than that between a low-Earth-orbit satellite and a ground station, so the experiments were in realistic settings for confirming the feasibility of quantum satellite technology.

The QKD experiment using the scheme in Fig. 3.3 was performed at night time but extra filtering was added to reduce the background counts. The receiver telescope had a variable iris to limit the spatial mode and only photon counts detected within the 5.9 ns window were included in the raw key string. Under good weather conditions, 28 dB link

loss was observed. 10 dB was from atmospheric loss, 14 dB from diffraction, and 4 dB from the transmitter telescope efficiency. In addition to 28 dB loss, the detector efficiency added 6 dB more. With ∼1 kHz dark count rate and 34 dB overall loss, the secret key rate of 12.8 bps with 6.48% QBER could be achieved. 3% of QBER came from the background counts, 3% from alignment errors, and 0.5% from the polarization analyzer.

At the same location, Ursin *et al.* [43] also tested polarization-entangled photons sharing between Alice and Bob. Alice replaced her weak-coherent-pulse source with a 710 nm Type-II energy-degenerate spontaneous parametric down-conversion. The output state was as follows:

$$|\psi^-\rangle = \frac{1}{\sqrt{2}}(|H\rangle_A |V\rangle_B - |V\rangle_A |H\rangle_B) \tag{3.3}$$

Alice also had the same polarization analyzer as Bob and polarization compensations were included before both polarization analyzers to ensure the reference frame of incoming photons were well maintained. The rest of the setup is the same as that from Fig. 3.3.

They obtained the value of $S = 2.508 \pm 0.037$, violating the inequality by 13 standard deviations and proving that the photon pairs were indeed entangled. Using the entangled-photon pairs, they also demonstrated QKD. For 75 s measurement time, 789 coincident counts could be detected, producing the secret key rate of 2.37 bps with QBER of 4.8%. Researchers from the Europe experimentally confirmed the feasibility of downlink quantum communication. Furthermore, they utilized these entangled sources and low-noise single-photon detectors to perform quantum teleportation experiment between La Palma and Tenerife [88]. Their results proved that ground-to-satellite quantum teleportation is feasible.

Researchers in China performed quantum teleportation and quantum entanglement distribution also for downlink configuration [46]. A scheme for quantum teleportation had Alice and Charlie placed next to each other and Bob 97 km away from them across a lake. Charlie generated polarization-entangled state, $|\phi^+\rangle = \frac{1}{\sqrt{2}}(|HH\rangle + |VV\rangle)$, and sent one photon to Bob. Alice randomly generated one of horizontal, vertical, $+45°$, $-45°$, clockwise circular, anti-clockwise circular polarizations and performed a Bell State Measurement (BSM) with the other entangled photon. For detection system, spatial, spectral, and temporal filtering were incorporated to reduce the background light. The total link loss varied between 35−53 dB depending on the weather condition across the lake. Quantum teleporation experiments lasted for four hours and the fidelity of the six states varied between 76-89%, averaging to 80%, which exceeds the classical limit of 2/3 [89].

For entanglement distribution experiment, Charlie was placed between Alice and Bob. The distance between Alice and Charlie was 51.2 km, between Bob and Charlie was 52.2 km, and between Alice and Bob was 101.6 km. Charlie generated the same $|\phi^+\rangle$. Total link loss of both channels combined varied between 66−85 dB, averaging to 79.5 dB, which was close to typical loss of 75 dB when a satellite at 600 km altitude uses 20 cm diameter transmitting telescope and both optical ground stations use 1 m diameter telescopes. They distributed entangled pairs for 32 000 s and obtained the correlation value of $S = 2.51 \pm 0.21$, successfully violating the Bell's inequality.

Dr. T. Jennewein and his team at the University of Waterloo (UW) in Canada, on the other hand, are interested in developing a quantum satellite for uplink configuration [45, 47]. The plan is to launch it in 600 km heliosynchronous orbit, with a simulated total link loss for 785 nm signal wavelength, 25 cm diameter transmitting telescope, and 30 cm diameter receiving telescope with an imaginary optical ground station at Ottawa, Ontario, Canada [45, 47]. The best satellite pass is when it travels directly above the ground station but it does not happen every time, so they simulated for 75th percentile of all passes occurring in a year [47]. The link loss then varied between 40−50 dB and they experimentally verified whether QKD system can tolerate such high loss and still generate secure keys using the setup in Fig. 3.4.

In a proof of concept QKD experiment, 256 pseudo-random bits were repeated for 1000 s and only sifting was performed as post-processing [45]. They obtained secure key rate at 57 dB losses, which includes 6 dB receiver loss. At 57 dB total loss, a secure key rate of 2 bps could be obtained when the source was clocked at 76 MHz repetition rate, showing that the key exchange is feasible between a ground station and a satellite receiver.

In a following experiment [47], full post-processing procedure was implemented and the receiver design was improved for testing the feasibility of secret key rate generation with total loss between 28.8−56.5 dB. The receiver loss was reduced to 4.5 dB, so the maximum link loss was similar to the previous experiment and everything else was the same. The new receiver design in Fig. 3.5 used a passive choice polarization analyzer because active basis choice added another complexity to the receiver design as it required time synchronization.

After sifting the raw key, error correction and privacy amplification were newly added in this experiment to extract the secret key that are actually used in encryption schemes. The asymptotic secret key rate of 0.5 bps was achieved with 56.5 dB total loss, confirming the feasibility of uplink configuration. The performance could be improved if high wavelength could be chosen to reduce the loss due to atmospheric turbulence effects.

Using the full uplink QKD setup, the UW research team also implemented a tracking

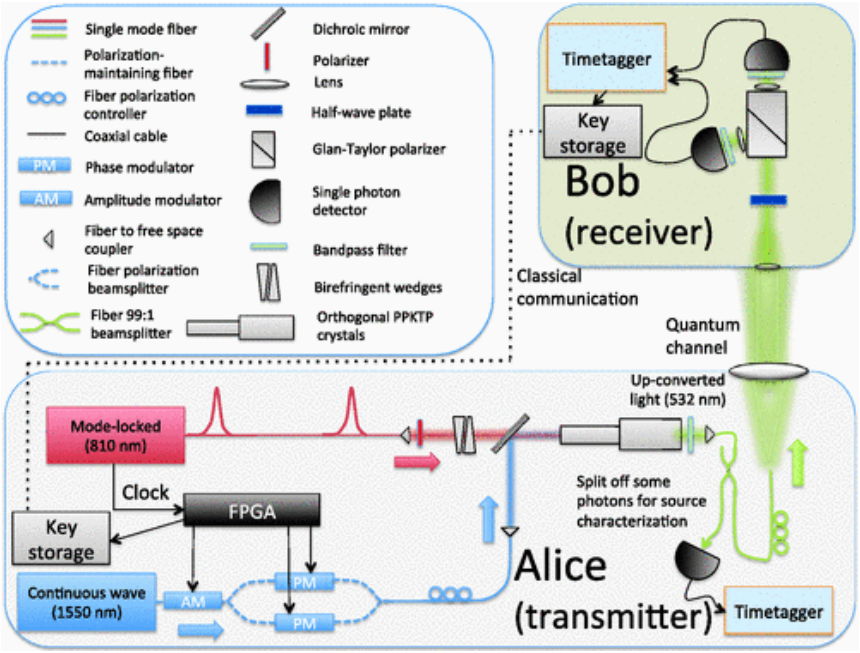

Figure 3.4: **Experimental setup for an uplink configuration feasibility test (Reprinted from [45]).** 532 nm signal pulses are generated by up-converting a 810 nm mode-locked laser with 76 MHz repetition rate and a 1550 nm continuous-wave laser. The output pulses have the mode-locked laser's repetition rate and short pulse width while their polarizations and intensities are controlled by the continuous-wave laser. The output signal wavelength is also converted to 532 nm. The signal pulses are then coupled into a single-mode fibre and collimated by a 3 in lens. This lens' position is adjusted to vary the diverging angle to simulate for different channel losses experienced at the receiver. The receiver uses an active choice BB84 polarization analyzer. The half-wave plate chooses the basis. The single-photon detectors have photon detection efficiency of 48% at 550 nm and the dark count rate of ≈20 Hz. The receiver causes additional 6 dB loss.

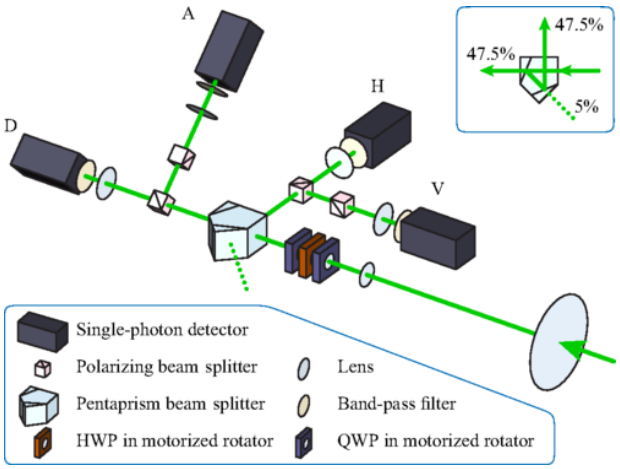

Figure 3.5: **New satellite receiver design for uplink (Reprinted from [47]).** In addition to changing the basis choice to passive, the new receiver incorporates spatial, spectral, and temporal filtering for background light. Quarter-wave plates and a half-wave plate can unitarily transform the incoming polarization state to any state.

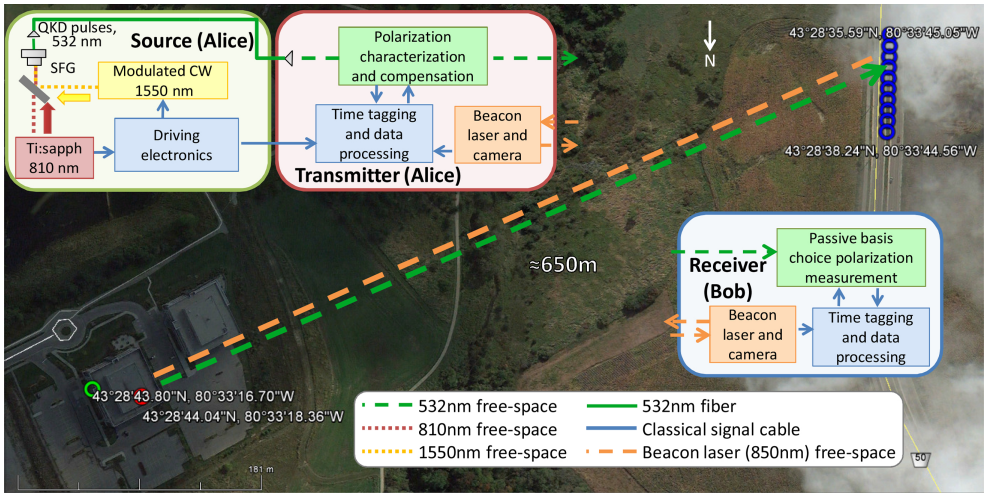

Figure 3.6: **Free-space QKD experiment with the receiver equipped on a moving truck (Reprinted from [48]).** In addition to changing the basis choice to passive, the new receiver incorporates spatial, spectral, and temporal filtering for background light. Half-wave plates and a quarter-wave plate can unitarily transform the incoming polarization state to any state. Blue circles on the top right corner indicate the distance the truck traveled.

and pointing system for a moving truck, traveling at the speed equivalent to the angular speed of the satellite at 600 km heliosynchronous orbit [48]. The maximum angular speed at the orbit is 0.72 °/s. This experiment tested the feasibility of uplink satellite

QKD with a receiver on a moving truck, whose angular speed was 0.75 °/s. Signal pulse generation, receiver design, and QKD protocol were the same from [47], except that polarization compensating waveplates are moved to the transmitter, as shown in Fig. 3.6. With 80 MHz signal repetition rate, the secret key rate of 40 bps was achieved. This research experimentally proved that QKD is feasible between a ground station and a moving object.

3.6 Ground-to-air/Ground-to-satellite experiments

A research group at LMU in Germany conducted a proof-of-principle airborne downlink QKD experiment [50]. The experiment had an airplane carry the transmitter and travel in a 20 km radius arc path at 290 km/h, which is equivalent to 4 mrad/s angular velocity, for 10 min. The transmitter sent four BB84 polarization states repeatedly because there was only one classical communication link for post-processing. Signal pulses with the mean photon number of 0.5 exited the transmitter telescope of 3 cm diameter aperture. The receiver had 40 cm diameter telescope and a passive choice polarization analyzer.

In order to perform such key exchange, the transmitter and receiver had to establish a link beforehand. As the plane entered the arc path, the transmitter and receiver share their global positioning systems (GPS) coordinates and orient their telescopes accordingly. The transmitter needs to be in the field-of-view (FOV) of the receiver before bidirectional beacon lasers are activated for fine pointing. The total link loss including the single-photon detection efficiency was 38 dB, and the mean sifted key rate of 145 bps with QBER of 4.8% was produced. The major difference between this experiment and other ground-based experiments was the need of the initial quantum channel establishment. This experiment required more upgrades on technology for full QKD operation but it proved the feasibility of exchanging quantum states with a flying object.

Researchers at UW in Canada much improved the technology and performed full uplink airborne QKD experiment [52]. They exchanged quantum states for 14 passes in both line and arc paths with channel link ranges of 3 km, 5 km, 7 km, and 10 km at the altitude of ≈1.6 km. The arc path length allowed longer key exchange time and more relaxed pointing, acquisition, and tracking (PAT) system, but the line path was a better representative of satellite paths.

Of 14 passes, 7 passes were successful at establishing a quantum link and 7 km line path and 10 km arc path were the longest links for each configuration. For 10 km arc path, the quantum link lasted for 269 s and 70947 secret bits with QBER of 3.39% were generated. The mean total loss was 42.6 dB. For 7 km line path, Alice and Bob could only exchange

quantum states for 158 s and 9566 secret bits with 3.58% QBER were produced. The mean link loss was 51.1 dB. Previous experiments [45, 47] showed that the channel link loss is between 40−50 dB for uplink QKD and this experiment demonstrated that it is feasible to generate secret keys with such channel loss and an airplane, whose angular velocity was similar to that of 600 km low-Earth-orbit satellite. The researchers noted that for the line path, faster PAT system will be necessary for performance improvement.

Researchers at the University of Science and Technology of China, Ningbo University, and Chinese Academy of Sciences in China experimentally verified three critical issues for satellite-based QKD: 1. rapid angular velocity and acceleration, 2. unwanted random motion of a satellite, 3. high link loss and atmospheric turbulence [51]. For angular velocity and acceleration verifications, they paced the transmitter on a turntable 40 km away from the receiver. The angular speed and acceleration of the turntable exceeded those of a low-Earth-orbit satellite. Polarization-encoding BB84 with decoy states with the repetition rate of 100 MHz was used. Total link loss for this test was ∼40 dB and the receiver could detect quantum states at 4200 Hz. For a platform with unwanted random motion test, they placed the transmitter on a floating hot-air balloon, 20 km away from the receiver. This verified the PAT system's ability to reestablish a quantum channel quickly whenever the line-of-sight was achieved and their system could recapture the hot-air balloon and exchange keys for 3−5 s. For high-loss free-space link, they placed the transmitter and receiver 96 km away from each other, having total channel loss of ∼50 dB. Post-processing was not performed but the receiver could detect 380 quantum states per second. For more realistic experimental verification for satellite-based communication, developing excellent PAT system is important.

Before China launched the first quantum satellite in 2016, researchers used retro-reflectors on already launched satellites to simulate quantum communications [54, 55]. Yin *et al.* [54] used a corner cube retro-reflector on CHAMP satellite (400 km low-Earth-orbit) to verify downlink single-photon transmission and detection feasibility. This experiment could test all three critical issues mentioned in the previous paragraph at once but QKD was not performed. Theoretical total link loss from the reflector to the receiving telescope was ≈41 dB, so the expected photon number per pulse at the receiver was 6.83×10^{-5}. The reflected mean photon number per pulse obtained from an experiment was 6.75×10^{-5}, which complies with the theoretical value. Therefore, this research proved the feasibility of sharing quantum states with a satellite.

Now that single-photon pulses reflected from retro-reflectors on a satellite can be detected at a ground station, Vallone *et al.* from Italy [55] sent BB84 polarization states (horizontal, vertical, clockwise circular, anticlockwise circular polarizations) to be reflected

off of Jason-2, Larets, Starlette, and Stella satellites. These satellites have corner cube retro-reflectors with polarization preservation coatings. For comparison, they also sent pulses to Ajisai satellite whose retro-reflector does not preserve polarizations. For the satellites with polarization preserving retro-reflectors, the average polarization measurement error was 4.6±0.8%, while the error from Ajisai is 40.5±0.7%. These results showed that single-photon polarization states can be obtained under different conditions and that polarization-encoding BB84 QKD is feasible.

In August, 2016, China launched 600 kg quantum satellite called *Micius* and performed the first QKD and entanglement distribution using downlink configuration, and quantum teleportation experiment using uplink configuration [61–63]. The satellite orbits at an altitude of 500 km and carries both entangled-photon pair source and weak coherent pulse source for all three experiments.

For QKD experiment, polarization-encoding BB84 with decoy states protocol was utilized [61]. 850 nm wavelength was chosen for transmission and eight laser diodes were implemented for producing four signal and four decoy polarization states. The satellite passes over Xinglong ground station once every night at 12:50 AM for 5 min [61]. 10 min before the satellite came into the view of the ground station, its attitude was adjusted to face the ground station. The satellite pass was a straight line path when observed by a ground station,so as shown in Fig. 3.7(a), the link distance between the satellite and the ground station varied from 645 km to 1200 km during the pass.

After 273 s of quantum key exchange, the sifted key rate obtained was 12 kbps at 645 km and 1 kbps at 1200 km. After error correction and privacy amplification, the secret key rate of 1.1 kbps was achieved with average QBER of 1.1% and total link loss of 40 dB at 1200 km. This is an incredible achievement proving that satellite-based QKD is indeed possible.

The technological challenge for satellite-based entanglement distribution was that the satellite needs to control two different transmitting telescopes to send entangled photons to two different optical ground stations [62]. Thus, two independent PAT systems were implemented. The entangled photons generated on the satellite were $|\psi^+\rangle = \frac{1}{\sqrt{2}}(|H\rangle\,|V\rangle + |V\rangle\,|H\rangle)$ and these were distributed between ground station in Delingha and Nanshan in Urumqi (1120 km) and between ground station in Delingha and Gaomeigu Observatory in Lijiang.

As two ground stations were separated by at least 1100 km, the satellite passed over each station at different times as shown in Fig. 3.8. Thus, the two-link channel length varied between 1600 km and 2400 km and the overall link loss fluctuated between 64 dB and 68.5 dB. (The ground-based experiment [46] experienced total channel link loss between

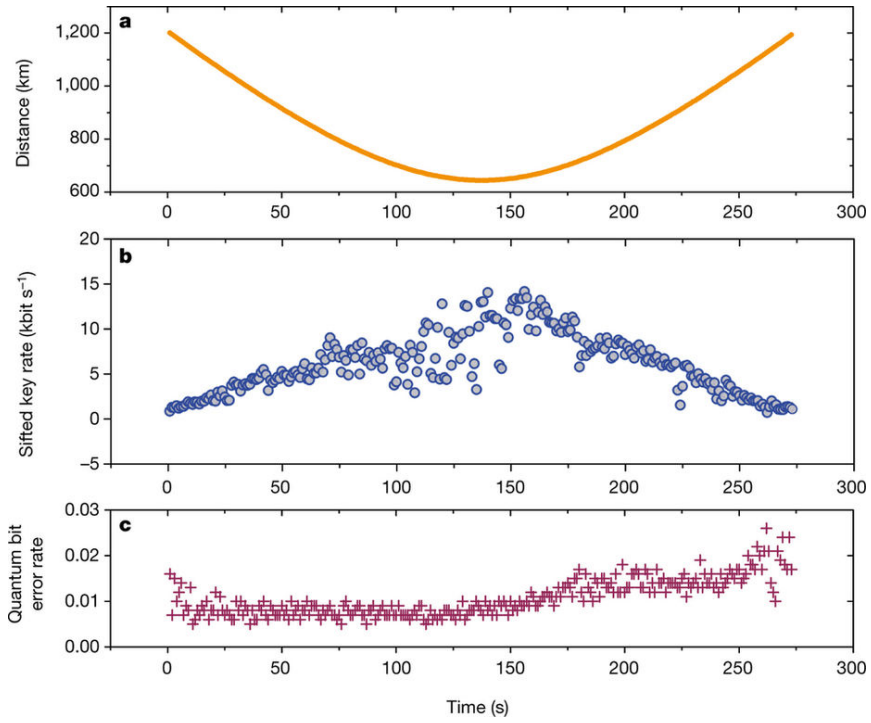

Figure 3.7: **Downlink satellite-based QKD using polarization-encoding BB84 with decoy states on December 19, 2016 between *Micius* and Xinglong optical ground station (Reprinted from [61]).**

66 dB and 85 dB for entanglement distribution.) Once again, the ground-based feasibility test verified the entanglement distribution for the correct channel link loss range. Fidelity of the received entangled pairs was $F \geq 0.87 \pm 0.09$ and the correlation value from CHSH inequality was 2.37 ± 0.09. Both values confirmed that the photon pairs are entangled.

For quantum teleporation experiment, the satellite functioned as a receiver and a transmitter at Ngari, Tibet generated a single qubit and teleported it to the satellite using $|\phi^+\rangle = \frac{1}{\sqrt{2}}(|H\rangle|H\rangle + |V\rangle|V\rangle)$ [63]. The ground station generated six polarization states in rectilinear, diagonal, and circular bases. The total link loss varied between 41 dB and 52 dB, as the link distance changed between 500 km and 1400 km. For each pass, photons from entangled pairs could be sent for 350 s, yielding an average fidelity of 0.8 ± 0.01. Satellite-based QKD, entanglement distribution (Bell test), and quantum teleportation were all successfully operated and silicon SPADs were utilized as single-photon detectors in all tests.

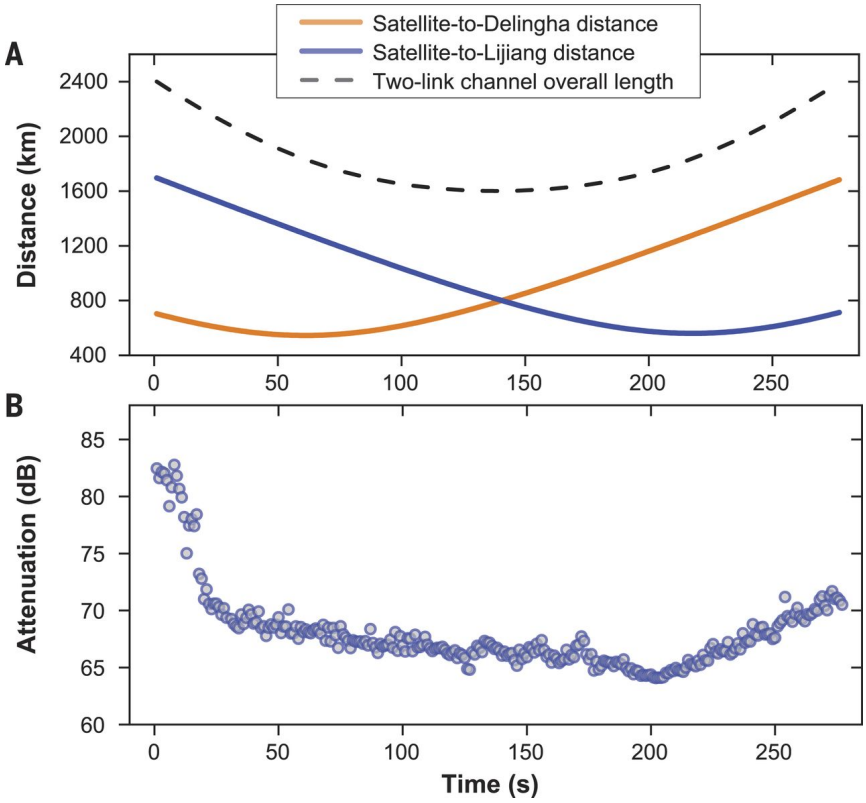

Figure 3.8: **Channel attenuation between the quantum satellite and two optical ground stations (Reprinted from [62]).**

3.7 Conclusion

It took 25 years from the first free-space QKD experiment [79] to the satellite-based quantum communications [61–63]. The launch of the Chinese satellite *Micius* is the first step towards establishing a global-scale quantum communication network. Now, there are efforts to perform quantum communications at daylight [44, 49], which require better background light filtering and PAT systems. There are also research on sending quantum satellites to medium-Earth-orbit (2000−36 000 km) [57] and geostationary orbit (>36 000 km) [60] to increase the communication duration and relax the complexity of the PAT system. In addition, studies on how the Doppler effect affect polarization states are conducted [53, 59] and time-bin encoding is proposed as another method for satellite-based QKD [58, 90]. There are also efforts to study the behaviour of quantum technologies under space conditions and launch a smaller payload using a Cube-Sat (10 cm × 10 cm × 10 cm satellite) [56, 64, 91, 92]. As the research on satellite-based quantum communications progresses, we may have a quantum satellite constellation network in the next 25 years. An immediate challenge to overcome to achieve such a network is radiation in space because it increases

the dark count rate of silicon SPADs [56, 65, 66, 68, 69]. As shown in Table 3.2, the dark count rate plays a critical role in the secret key rate generated by QKD and in determining the maximum operational distances for Bell's inequality test and for quantum teleportation. Without any radiation damage mitigation in SPADs in space, the useful lifetime of a quantum satellite is shortened. Therefore, before launching a quantum satellite, we must study how to reverse the radiation damage in space. Before explaining my radiation damage mitigation method, the next chapter describes how silicon SPADs operate and the following chapter discusses radiation in space and how it damages silicon SPADs.

Chapter 4

Silicon Single-Photon Avalanche Photodiode and Quenching Circuit

4.1 Introduction

Single-photon detectors are essential components in quantum communications and silicon Single-Photon Avalanche photoDiode (SPAD) have the best performance yet and are commercially available. This chapter describes how silicon SPADs operate as a single-photon detector and explains important parameters.

4.2 Operating principle

Silicon SPADs are diodes with the following structure:

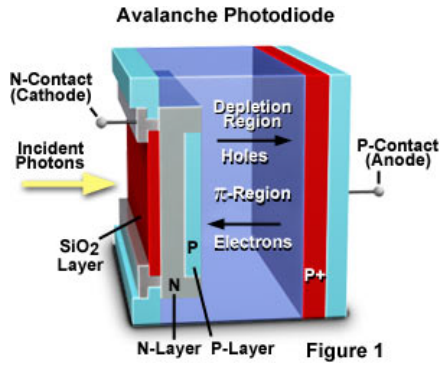

Figure 4.1: **P-type reach-through avalanche photodiode (Reprinted from [93]).**

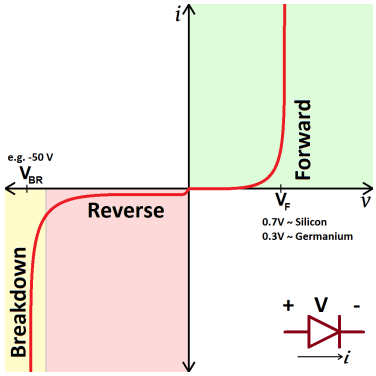

Figure 4.2: **Diode I-V curve (Reprinted from [94]).**

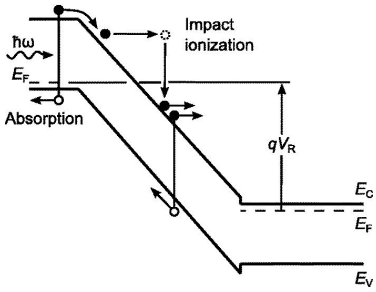

Figure 4.3: **Band diagram representation of impact ionization process (Reprinted from [96]).**

The structure is similar to the regular diodes and have the same I-V characteristics as them, as shown in Fig. 4.2. However, SPADs are only reverse-biased above the breakdown voltage (V_{br}) for photon detection operation. An incident photon is absorbed in the silicon bulk, called π-region in Fig. 4.1, and creates an electron-hole pair. Under the reverse bias, the electron-hole pair can be swept across π-region and reach the avalanche region, P+ layer, which is thin and thus has a very high electric field. When a carrier travels across the region, it may collide with a silicon atom and transfer the excitation energy, creating another electron-hole pair. This process is called *impact ionization*, as shown in Fig. 4.3. Now, each electron-hole pair can independently generate a new pair until they exit the junction. Under a high electric field, impact ionization can occur frequently, producing a macroscopic electric current (mA range) [95]. This process of generating a high current from an electron-hole pair is called *avalanche effect*.

SPADs can be in different operation modes. If the reverse bias is below the breakdown voltage, the diode is in *linear mode*. The generated electric current is proportional to input light intensity with a certain gain R. If it is above the breakdown voltage, it is in *single-photon detection mode*, which is also known as Geiger mode [97]. In Geiger mode, a

macroscopic current can be generated from a single photon, but this current needs to be quenched by an external circuit [95].

4.3 Quenching circuits

Figure 4.4 shows the typical passive quenching circuit. V_{bias} is set to $V_{\text{br}}+V_{\text{excess}}$. At rest, no current flows in the circuit [95]. A photon absorption closes the switch and causes the discharge of both capacitors C_{d} and C_{s}, producing $i(t) = (V_{\text{d}}(t) - V_{\text{br}})/R_{\text{d}}$ to flow. The macroscopic current increases the voltage across a high resistance, R1, and it automatically lowers $V_{\text{d}}(t)$ close to V_{br}. When $i(t)$ becomes smaller than $\sim$100 µA, the avalanche current stops to flow [95]. During this avalanche process, the SPAD is insensitive to any incoming photons and the time constant for the quenching process is $\tau_{quenching} \approx (C_{\text{d}} + C_{\text{s}})R_{\text{d}}$. Figure 4.5 shows an avalanche pulse of a silicon SPAD at V_{out}.

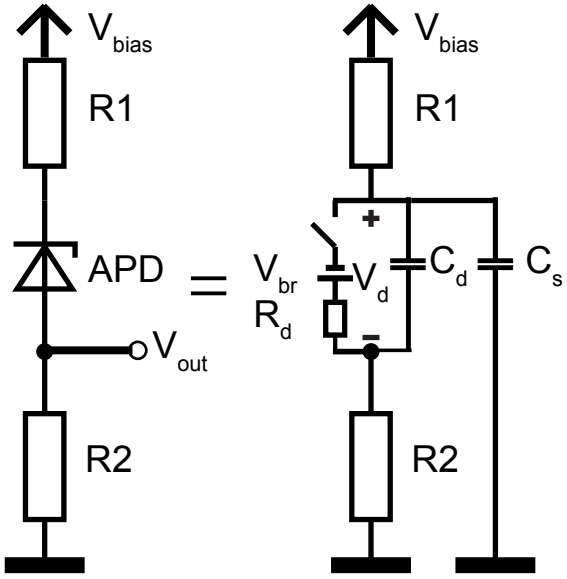

Figure 4.4: **Passive quenching circuit with SPAD modeling (Redrawn from [95]).** R1 is a high-impedance quenching resistor and R2 is a small impedance readout resistor. C_{d} (C_s) is the junction (parasitic stray) capacitance.

After the current flow is completely stopped, the SPAD switch is opened again and the capacitors are *recharged*. The SPAD becomes sensitive to single photons again during the recharge process, so Fig. 4.6 shows that it is feasible to trigger a current flow before fully reaching V_{bias}. Recharge time constant is $\tau_{recharge} = (C_{\text{d}} + C_{\text{s}})R1$. These time constants for the quenching process and the recharge time determine the speed of SPADs.

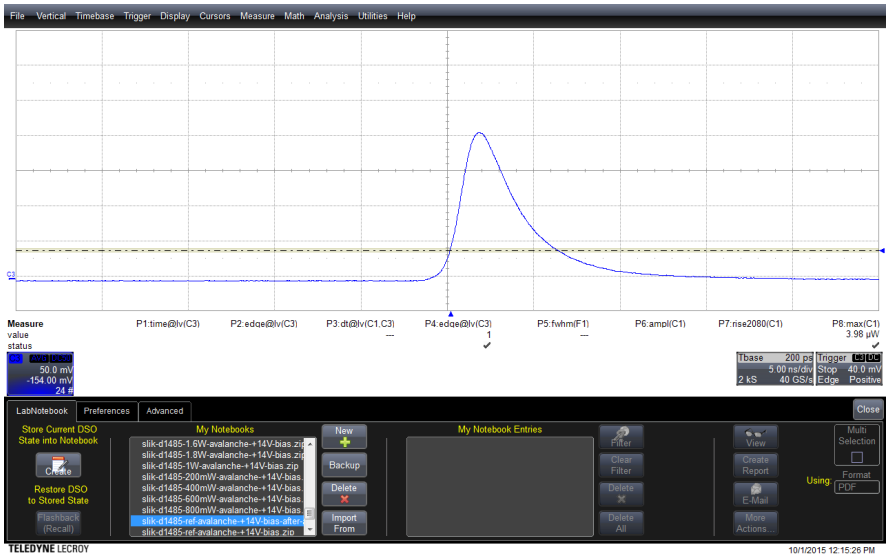

Figure 4.5: **Oscilloscope capture of an avalanche pulse.** The avalanche pulse is a voltage waveform measured at V_{out} in Fig. 4.5.

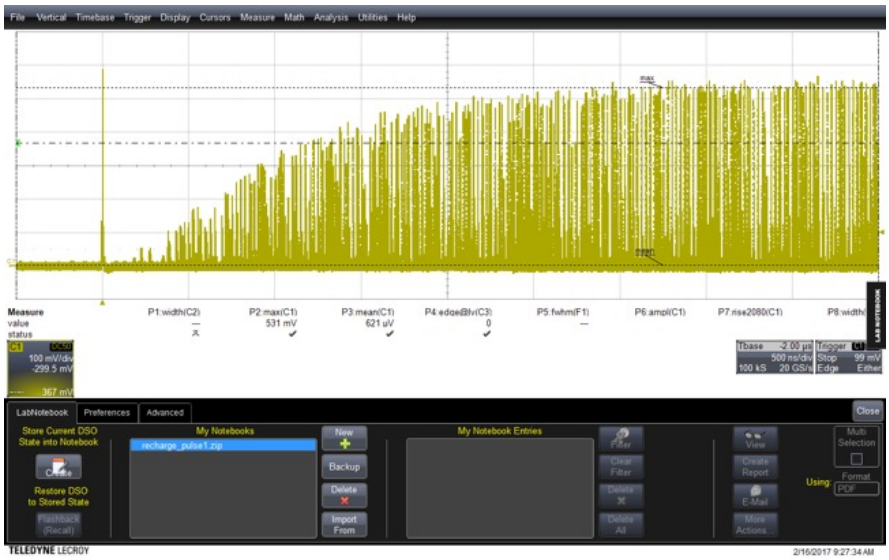

Figure 4.6: **Oscilloscope capture of the recharge process.** The avalanche pulses are measured at V_{out} in Fig. 4.5. The oscilloscope's trigger point is set to the leftmost reference avalanche pulse. It is visible that the subsequent avalanche pulses' amplitudes form an envelope of an exponential function. Its time constant should be $\tau_{recharge} = (C_{\text{d}} + C_{\text{s}})R1$. An avalanche pulse can be triggered anytime during the recovery of V_{d}, but since the macroscopic current, $i(t)$, is proportional to V_{d}, the output pulse amplitude is small when $V_{\text{d}} - V_{\text{br}}$ is small.

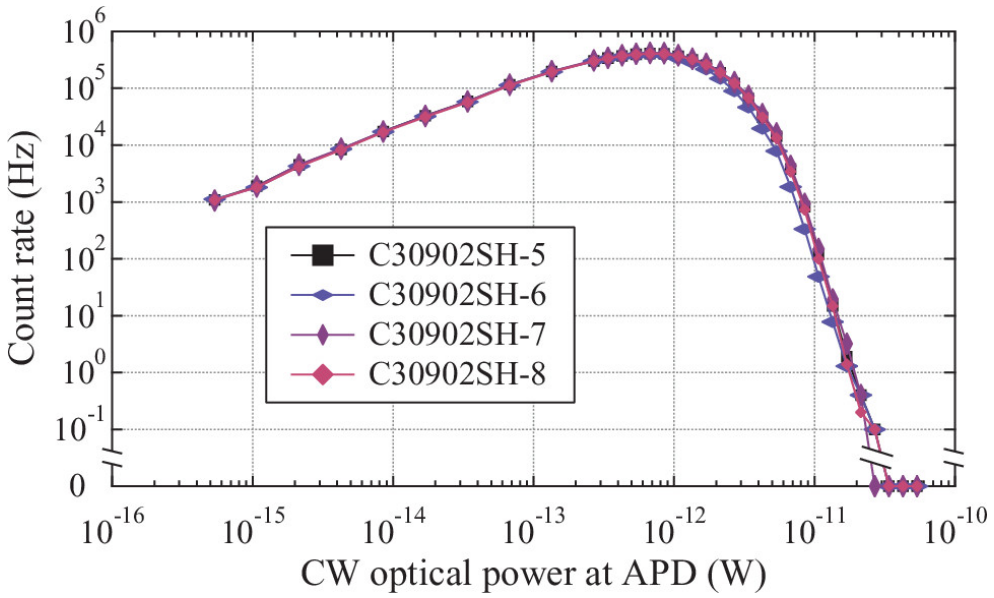

Figure 4.7: **Detector saturation curve as a function of calibrated optical power (Reprinted from [98].)** When the count rate exceeds the saturation level, the mean avalanche pulse amplitude becomes smaller, causing the counter discriminator with a fixed threshold voltage to miss avalanche pulses. As the input optical power increases, the count rate eventually drops to zero. Figure title is also copied from [98].

When the count rate exceeds the saturation level, an avalanche pulse is more frequently triggered before reaching V_{bias}. Thus, the mean amplitude of the avalanche pulses also becomes smaller and the pulse amplitude distribution widens. The passive quenching circuit uses a fixed discriminator threshold value to distinguish avalanche pulses from noise, so if the avalanche pulse amplitude is below the threshold, it is missed, resulting in a decreased count rate. Figure 4.7 shows how the count rate changes with increasing optical input power. The same over-saturation effect can occur for SPADs with a very high dark count rate (false photon count rate). Thus, it is important to measure the pulse amplitude distribution to verify the over-saturation effect.

Active quenching circuit uses a feedback loop to quench the avalanche pulse much quickly by lowering V_{bias} to V_{br} [95]. After a fixed hold-off time, V_{bias} is also quickly recovered. Therefore, active quenching circuit provides a faster detection rate than passive quenching circuit, but it requires more complex circuit.

Gated-mode operation is used if the receiver knows when to expect the incoming photons [95]. It sets the SPAD below V_{br}. Just before a photon is expected, an external circuit sends a narrow voltage pulse to place the SPAD in Geiger mode. The SPAD is quickly quenched when the voltage pulse comes back to zero. This mode has advantages of fast

quenching to limit the population of trapped electrons and of restricting dark count occurring only when the voltage pulses are applied. However, this mode requires synchronization between two communicating parties and extra signal filtering are necessary for removing the gate pulses from the detection output signals.

4.4 Parameters

4.4.1 Dark count rate

A dark count is a false photon count caused by thermally excited, tunneling, and trapped electrons [97]. Electrons are excited by thermal energy and defect levels in the bandgap increases the probability. Lowering temperature can exponentially decrease thermally excited electrons. Electron tunneling occurs at a very high bias voltage because the pn junction in the avalanche region in Fig. 4.3 is stretched out vertically, making the bandgap energy in the junction to be very thin. With the help of defect levels, electrons in the valence band can move to the conduction band. To reduce this effect, SPADs should not be biased too high. During an avalanche process, electrons can be trapped in deep defect levels produced by impurities. Given a fixed number of trap levels, the population of trapped electrons is proportional to the total charge passing through the SPAD. The trapped electrons can be released during or after V_{bias} is fully recharged and trigger a false avalanche effect, which is also known as an *afterpulse*. Usually, trapped electrons are released during the quenching process at room temperature. However, at lower temperature, trapped electrons have longer lifetimes, so afterpulses are more likely to occur during or after V_{bias} is fully recharged and trigger a false photon count. Thermal generation and afterpulses constitute the majority of the dark count rate.

4.4.2 Photon detection efficiency

The photon detection efficiency is comprised of three main factors [95]. The first factor is the internal quantum efficiency. It indicates the probability of an absorbed photon creating an electron-hole pair. Next is the photoelectron efficiency. This is the probability of the electron-hole pair reaching the avalanche region before recombination. Lastly, the avalanche efficiency measures the probability of the electron-hole pair triggering an avalanche effect to generate a macroscopic current, detectable as a photon count. Photon detection efficiency increases with V_{bias} because a stronger electric field can increase both

photoelectron efficiency and avalanche efficiency. In the linear (classical) regime, the photodiode is no longer sensitive to single photons due to the noise current, so the detection efficiency is defined by the external quantum efficiency (η_e):

$$\eta_e = \frac{h\nu I_{\text{ph}}}{qP_{\text{in}}} \tag{4.1}$$

where h is the Planck constant, ν input signal frequency, I_{ph} output photocurrent, q the electric charge, and P_{in} the input optical power.

4.4.3 Timing jitter

The timing jitter is the temporal variation of detection output signal with respect to a photon absorption at a reference time. This parameter becomes important when two communicating parties want to share accurate detection timestamps for classical post-processing. Timing jitter can be reduced by increasing V_{bias} because carriers under a high electric field travels much faster to reach the avalanche region.

4.4.4 Afterpulsing probability

Afterpulsing probability analysis calculates how often afterpulses occur in the dark count rate and what the lifetimes of trapped electrons are. For every detection event, our software adds all subsequent detection events occurring up to 10^{-2} s later to a histogram, with exponentially growing time bins [99], as shown in Fig. 4.8. Unlike the standard autocorrelation method, this improved analysis produces a plot that converges to the background count rate, instead of following an exponential decay. Using exponentially increasing bin sizes filters out statistical fluctuations in the tail and also resolves the fast changing avalanche peak.

The shape of this histogram (Fig. 4.8) presents four features: an SPAD's dead time, its recharge time, its trapped-electron time constants, and the background count rate. In Fig. 4.8, the *dead time* begins immediately after a photon detection (time 0) and ends when counts begin to reappear at roughly 0.8 µs. This is when the SPAD is insensitive to any input single-photons. The recharge time is the time it takes for the count rate to reach the peak value after the dead time. Trapping time constants can be found by fitting the exponentially decaying slope of the peak. The plot levels off to the background count rate and the black shaded area is the afterpulsing probability.

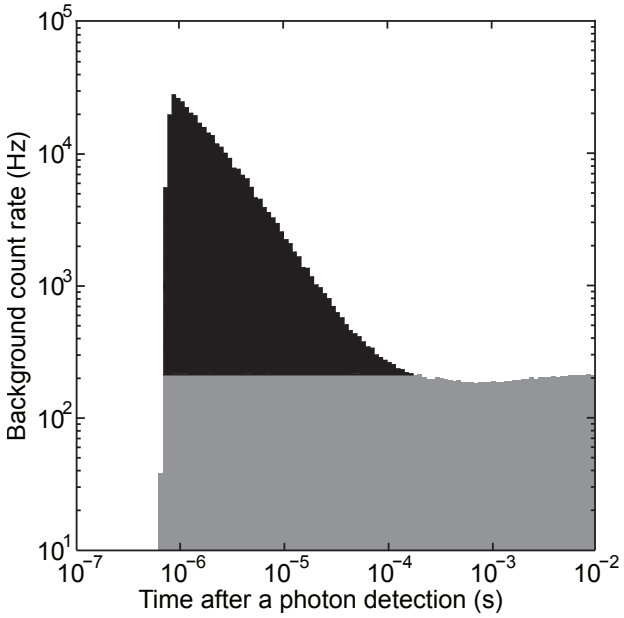

Figure 4.8: **Afterpulsing histogram example.** The histogram of the time difference between SPAD output pulses shows the SPAD's dead time from 0 to roughly 0.8 µs, followed by a recharge time of ≈150 ns. The following peak is formed of afterpulses. The count rates then settle down to the background count rate of ≈200 Hz. A possible reason for a slight increase in the count rate at the end is the high voltage supply rebounding after being slightly sagged by the charge being drawn by the single avalanche. The black shaded area is the afterpulsing probability.

4.5 Conclusion

A silicon SPAD can be biased above V_{br} to operate in Geiger mode, which enables single-photon detection. A detector is fully characterized from measured dark count rate, photon detection efficiency, timing jitter, and afterpulsing probability. For space applications, the bulk silicon in the SPAD is vulnerable to radiation damages. The next chapter explains why and shows radiation dose estimations and radiation tests on silicon SPADs to predict their behaviours in real space.

Chapter 5

Impact of Radiation Damage in Space

5.1 Introduction

Energetic electrons and protons trapped in Earth's magnetic fields and solar protons that penetrate the magnetic fields cause radiation damages to any equipment in the orbit. Electronics equipped on satellites should be manufactured to withstand such damages but silicon Single-Photon Avalanche photoDiode (SPAD) are particularly vulnerable to radiation damages. A few studies [65, 66, 68, 100] found that these radiation damages increase the dark count rate of silicon SPADs. However, for ground-to-satellite quantum communications, it is advised to keep the dark count rate below 200 Hz per detector to achieve good performance (See Section 3.3). As a result, it is important to estimate radiation doses accumulated over the operation period at a desired orbit and to experimentally check the rate of dark count rate increase for the mission time. This chapter explains how the energetic particles increase the dark count rate, how radiation dose was estimated for the two projects of this thesis, and how commercial silicon SPADs reacted to monochromatic proton radiation.

5.2 How does radiation in space affect a low-Earth-orbit quantum satellite?

In spite of the protection by Earth's magnetic fields, radiation exposure in low-Earth-orbit is due to a slight offset in Earth's rotational axis and magnetic pole. The offset causes the inner radiation belt to be pulled towards Earth's surface down to 200 km above the

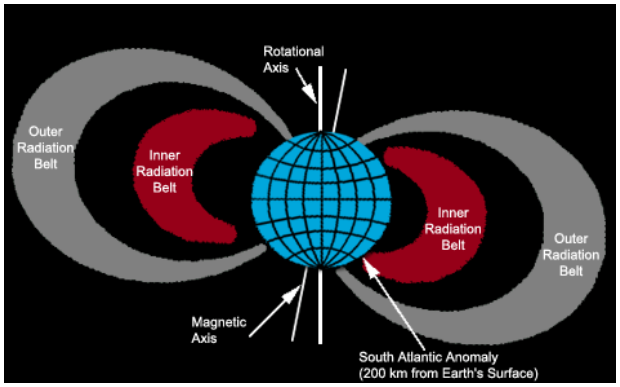

Figure 5.1: **Earth's radiation belts (Reprinted from [101]).** A slight offset in Earth's rotational axis and magnetic pole causes the inner radiation belt to be pulled towards Earth's surface down to 200 km above the sea level near South America.

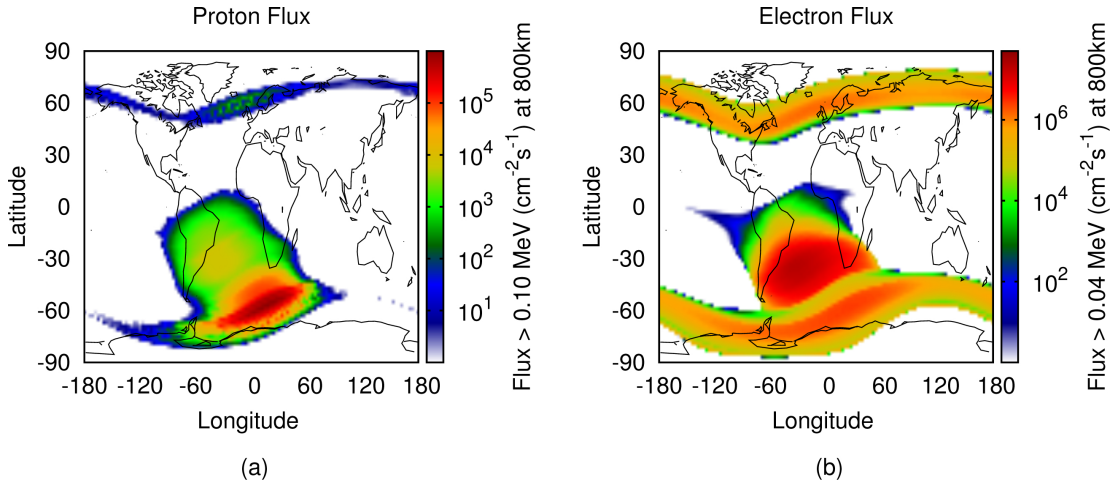

Figure 5.2: **Proton and electron fluxes at 800 km above the sea level (Reprinted from [69]).**

sea level near South America, as shown in Fig. 5.1. This region is called South Atlantic Anomaly (SAA). Figure 5.2 shows that radiation exposure is much higher in the southern hemisphere. Thus, devices equipped on satellites pass through the affected regions, so they need to be radiation-proof to remain operational for the entire mission time.

Trapped electrons cause ionization damage, while trapped protons cause displacement damage [65]. Ionization damage creates trapped charges in the insulation layers, so it is detrimental to devices such as complementary metal-oxide-semiconductor but its effect is negligible in silicon SPADs when compared to the damage done by trapped protons. The protons displace silicon atoms and create additional defects, forming extra energy levels in the bandgap. This allows more electrons to be excited with less thermal energy and thus

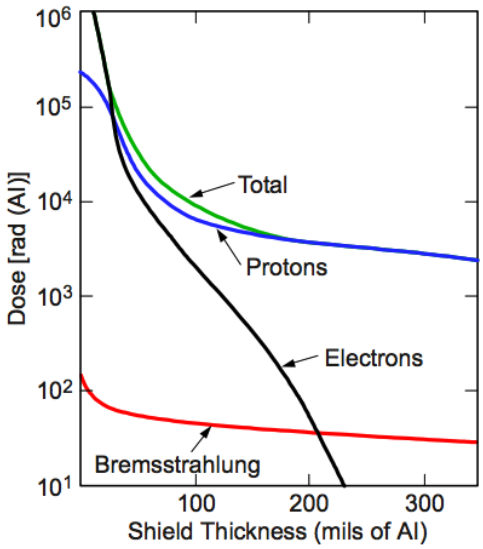

Figure 5.3: **Effect of aluminum shielding for radiation damage mitigation (Reprinted from [102]).** Total dose for a 5-year mission at 705 km polar orbit.

produce a higher dark count rate.

Shielding electronic devices with aluminum can reduce total radiation doses [102]. Ionization damage can be greatly reduced if more than 5 mm thick aluminum is used, as shown in Fig. 5.3. However, the reduction of displacement damage is not as significant and satellite mass restriction also limits the amount of shielding. Thus, understanding the impact of proton radiation damage on silicon SPADs is essential to predict how long they can operate in space and to identify radiation damage mitigation methods.

5.3 Radiation dose calculation

The SPENVIS software [103] is used for radiation dose calculation with custom orbit information and operation duration. For trapped protons, AP8-MIN and AP8-MAX models are used and they are based on real radiation data in space collected between 1960s and 1970s [104]. They are now accurate within a factor of two. For our calculation, AP8-MIN is used because the solar cycle 24 will be at the solar minimum in 2018-2020 and it gives worse radiation damage to the silicon SPADs [105]. For trapped electrons, AE8-MAX is used as it gives higher ionization damage. For long-term solar proton damage, the model developed by JPL is used for mission time longer than a year. Various aluminum shielding thickness can also be taken into account and the software outputs total Displacement Damage Dose (DDD).

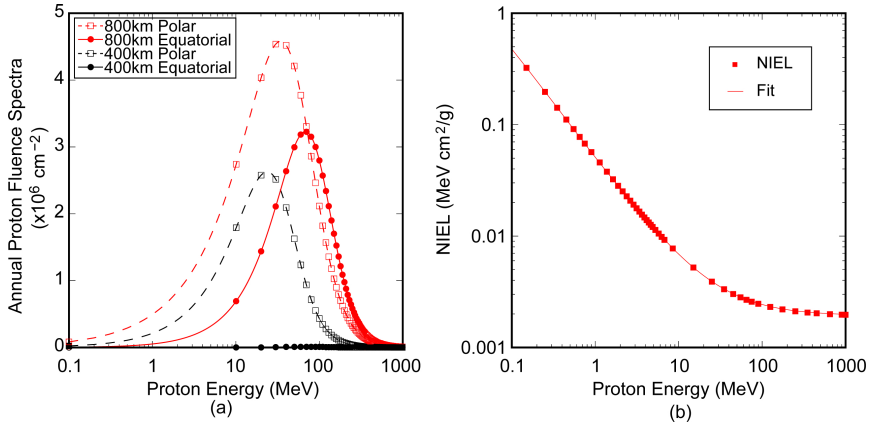

Figure 5.4: **Proton energy spectrum and corresponding non-ionization energy loss for silicon (Reprinted from [69]).**

Figure 5.4 shows that protons in space possess a spectrum of energy and each energy has a different non-ionization energy loss (NIEL), which is the damage impact factor. It also shows that protons with lower energies have higher NIEL, so more displacement damage occurs when the orbit changes from the equatorial to polar and when a satellite is farther away from the Earth due to the increased fluence of low energy protons. Total DDD can be calculated by integrating the product of proton fluences curve (Fig. 5.4(a)) and NIEL curve (Fig. 5.4(b)) over the entire energy spectrum.

$$DDD\ (MeV/g) = \int_0^\infty \phi_p(E) * NIEL(E)\ dE \tag{5.1}$$

where $\phi_p(E)$ is the proton fluences (cm^{-2}) and $NIEL(E)$ is NIEL ($\mathrm{MeV} * \mathrm{cm}^{-2}/\mathrm{g}$) at energy E.

For radiation testing at a facility, generated protons are monochromatic and their fluences are controlled. Thus, total DDD needs to be converted to proton fluences for a monochromatic energy. The SPEVNIS software allows a user to input a monochromatic energy and then uses the following equation [100] to also output equivalent proton fluences at the selected proton energy:

$$\phi_p(E_{selected}) = \frac{DDD(MeV/g)}{NIEL(E_{selected})} \tag{5.2}$$

Table 5.1: **Simulated fluences at 100 MeV protons and equivalent mission durations at QEYSSat orbit.** QEYSSat orbit is a heliosynchronous 600 km noon-midnight orbit.

Target fluence (p/cm^2)	**Equivalent mission duration at QEYSSat orbit (months)**
1×10^8	0.6
1×10^9	6
2×10^9	12
4×10^9	24

5.3.1 Radiation dose calculation for QEYSSat orbit for first laser annealing experiments

The samples (Excelitas SLiK, Excelitas C30902SH, Laser Components SAP500S2) that are tested in the first laser annealing experiments were initially irradiated for a recent study by Anisimova *et al.* [70]. The target orbit is a heliosynchronous 600 km noon-midnight orbit (Quantum Encryption and Science Satellite (QEYSSat) orbit) and 10 mm aluminum shielding is added for the calculation. Expected mission duration is 24 months, so fluences of 100 MeV protons are calculated for 0.6, 6, 12, and 24 months. Table 5.1 lists corresponding proton fluences. Two Excelitas SLiK and two Laser Components SAP500S2 are irradiated at each proton fluence level, while Excelitas C30902SHs are irradiated at $1 \times 10^9/cm^2$ only.

5.3.2 Radiation dose calculation for International Space Station orbit for second laser annealing experiments

Laser Components' new silicon SPAD model, SAP300, provided by Prof. Alex Ling's group at the National University of Singapore (NUS), is irradiated for further studies on the laser annealing effect. NUS is interested in the radiation environment in the International Space Station (ISS) orbit for its nanosatellite but they could also be used for the QEYSSat project, so proton fluences are carefully selected to cover both parties' mission durations at their targeted orbits. Table 5.2 shows simulated proton fluences and their equivalent

mission durations in the ISS and QEYSSat orbits.

Table 5.2: **Target fluences at 100 MeV proton energy and equivalent mission durations at ISS and QEYSSat orbits.** ISS orbit is 400 km low Earth orbit with the inclination angle of 51.64°, while QEYSSat orbit is a heliosynchronous 600 km dusk-dawn orbit. 1.8 mm aluminum shielding is chosen for the ISS orbit, while 10 mm aluminum shielding is selected for the QEYSSat orbit. Our results from SPENVIS shows that the QEYSSat orbit experiences about three times as much proton radiation as the ISS orbit.

Module Identifier	**Target fluence (p/cm^2)**	**Equivalent mission duration at ISS orbit (months)**	**Equivalent mission duration at QEYSSat orbit (months)**
LC-A	1.66×10^8	3	1
LC-B	1.66×10^8	3	1
LC-C	3.32×10^8	6	2
LC-D	3.32×10^8	6	2
LC-E	6.73×10^8	12	4
LC-F	6.73×10^8	12	4
LC-G	6.73×10^8	12	4
LC-H	6.73×10^8	12	4
LC-I	2×10^9	36	12
LC-J	2×10^9	36	12
LC-K	4×10^9	72	24
LC-L	4×10^9	72	24

5.4 Radiation testing

All proton radiation tests were performed at TRIUMF, Vancouver, Canada [106].

5.4.1 Samples for the first laser annealing experiments

The radiation test results are explained in detail by Anisimova *et al.* [70] but the notable results are that all detectors are saturated after proton fluences equivalent to one year mission time at the QEYSSat orbit when characterized at 0 °C. Highlighted section in Fig. 5.5 shows how the dark count rate changes during proton irradiation. For proper quantum communications operations, radiation damage mitigation methods are required to reduce the dark count rate.

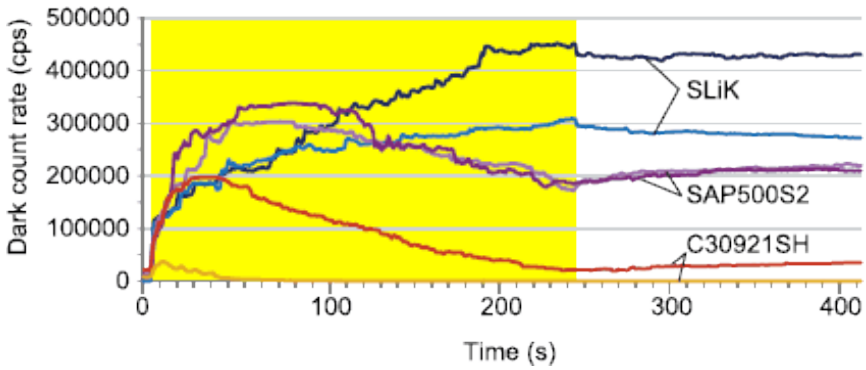

Figure 5.5: **Dark count rate of silicon SPADs during proton irradiation (Reprinted from [70]).** SPADs are biased at 20 V above the breakdown voltage and their base temperatures are kept at 0 °C. The dark count rate of C309021SH and SAP500S2 appear to decrease after some time, but this actually means that the dark count rate exceeded the saturation level, so avalanche pulses are too small for the discriminator circuit to distinguish them (See Section 4.3).

5.4.2 Samples for the second laser annealing experiments

Table 5.3 shows initial characterizations performed by NUS using its passive quenching circuit and by Institute for Quantum Computing (IQC) using a custom detector module, shown in Fig. 5.6, at TRIUMF. Breakdown voltage, dark count rate, and average avalanche pulse height are measured at room temperature. The discrepancies in the data are due to different electronics used for characterization and temperature variations. At TRIUMF, SPADs are connected to the detector module via receptacles to avoid a soldering iron thermally annealing SPADs after proton radiation. A metal plate holds SPAD packages in place (see Figure 5.7) and we placed black metal tape on SPAD glass windows to block light. In addition, the detector module is then placed on a metal bracket inside a desk drawer at TRIUMF (see Figure 5.8) to provide as dark environment as possible for proper characterization.

Table 5.3: **Initial characterization performed by NUS and IQC.** NUS characterized the samples at 22 °C. It was not possible to control the operating temperature at TRIUMF, so a Platinum temperature sensor (Pt 100) connected to an industrial controller (JUMO dTRON) in 4-wire configuration monitors the temperature of the metal plate. The temperature during characterization is noted down as operating temperature. The discrepancy in the mean pulse amplitude is due to different readout resistor values used by NUS and IQC. V_{br}: Breakdown voltage, V_{bias}: Bias voltage, V_{ex}: Excess voltage ($V_{bias} - V_{br}$), DCR: Dark count rate, MPA: Mean pulse amplitude, OT: Operating temperature.

Module Identifier	NUS					IQC					
	V_{br} (V)	**V_{bias} (V)**	**V_{ex} (V)**	**DCR (Hz)**	**MPA (mV)**	**OT (°C)**	**V_{br} (V)**	**V_{bias} (V)**	**V_{ex} (V)**	**DCR (Hz)**	**MPA (mV)**
LC-A	162.9	173.4	10.5	12000	510	21	161.2	171.7	10.5	10518	135.4
LC-B	163.9	174.4	10.5	14300	530	21.3	161.1	171.6	10.5	12090	122.6
LC-C	157	167.5	10.6	14600	604	24.7	155.6	166.2	10.6	15243	125
LC-D	166.6	177.3	10.7	16800	538	24.7	167	177.7	10.7	19652	130
LC-E	165.5	176.5	11.1	13800	531	22.9	165.1	176.2	11.1	14612	136.5
LC-F	167	177.7	10.6	15700	511	23.1	165.5	176.1	10.6	15958	116.2
LC-G	160.2	171.3	11.1	15800	587	22.2	159.6	170.7	11.1	15617	157.7
LC-H	163.8	175	11.2	17800	642	22.2	161.8	173	11.2	16262	151.5
LC-I	157.5	168	10.6	16500	590	22.4	155	165.6	10.6	13632	131
LC-J	159.5	170.2	10.6	16500	553	22.4	157.8	168.4	10.6	15027	126
LC-K	160.7	171.8	11.1	16800	600	22.7	158.2	169.3	11.1	15107	131.5
LC-L	156.5	167.5	11.1	16500	553	22.5	155.3	166.4	11.1	16385	124.8

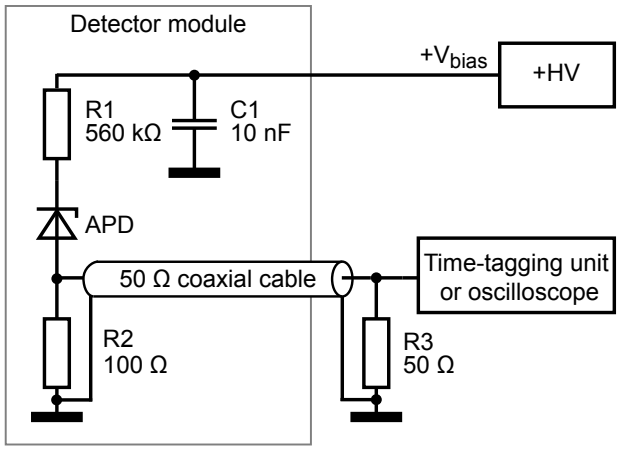

Figure 5.6: **A schematic of a detector module.** The detector module can house six SPADs but only one channel is shown here. Each channel contains a passive quenching circuit, is connected to an external high-voltage supply, and outputs to a time-tagging unit or an oscilloscope. (See Section 4.3 for the description of how the detector module works.)

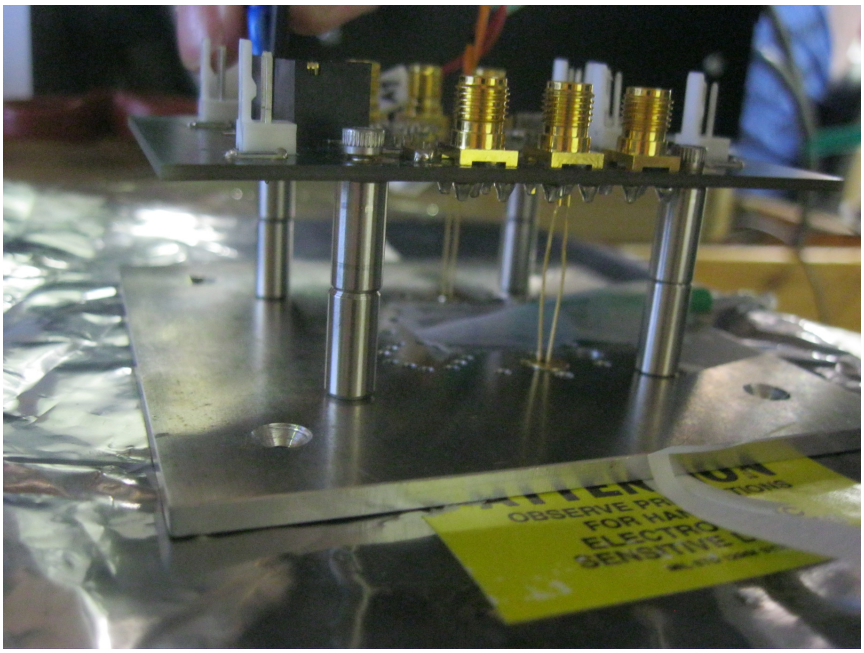

Figure 5.7: **Photo of the Laser component SPAD mounted on a detector module.**

After proton irradiation, all samples are characterized at TRIUMF. Table 5.4 shows that high-energy protons increase the dark count rates of most samples while those of LC-A, LC-E, LC-I, and LC-K are decreased when they are characterized at TRIUMF. The reduction is due to saturation in electronics, as explained in Section 4.3. After returning from the trip to TRIUMF, each sample's characterization as well as avalanche pulse amplitude distribution

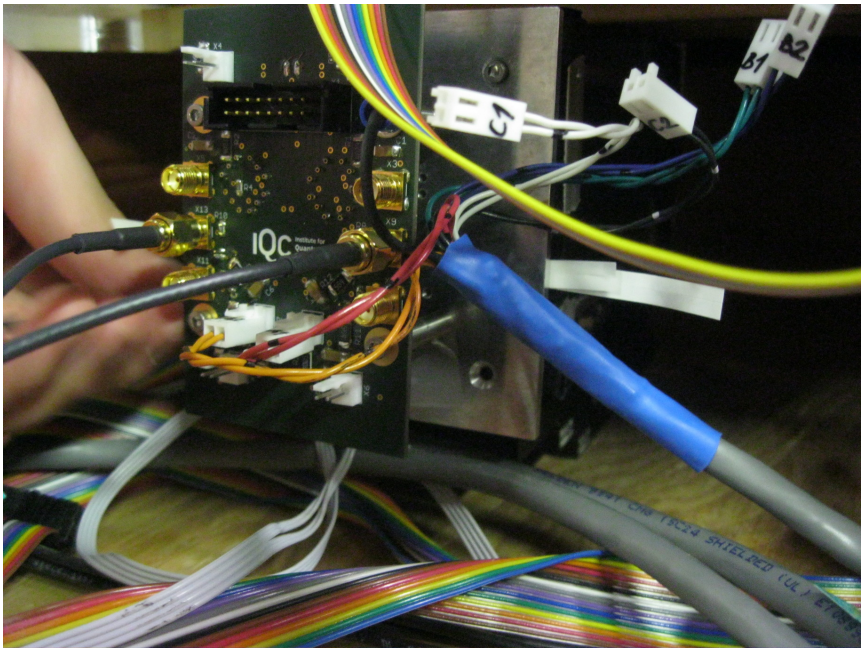

Figure 5.8: **Photo of the Laser component SPAD mounted on a detector module placed on a metal bracket.**

are performed and analyzed at room temperature to confirm this saturation effect and the samples are also characterized further at −20 °C, where SPADs are not saturated, to find the relationship between the dark count rate and proton radiation fluences. In Figure 5.9, the distribution at room temperature shifts toward 0 mV and it becomes wider, as SPADs are exposed to higher proton fluences. At −20 °C, all SPADs are not saturated, so the distribution curves are narrow and slopes are sharper.

Table 5.5 shows the characterization results at −20 °C. All samples are no longer saturated (See Section 4.3 for the explanation of the saturation effect); thus, the relationship between the dark count rate and the proton radiation fluences can be better analyzed from the data. For each proton radiation fluence, samples' dark count rates are averaged and these values are plotted in Figure 5.10.

In addition to these SAP300s irradiated and characterized at TRIUMF, NUS sent three SAP300s that were previously irradiated. Table 5.6 summarizes the characterization results taken by them and these samples are used for testing whether the laser annealing effect is permanent.

Table 5.4: **Characterization performed by IQC at TRIUMF.** Samples with highlighted cells seem to have their dark count rates reduced after proton irradiation, probably due to saturation. Mean pulse amplitude is measured with 100 mV trigger level at TRIUMF and with 20 mV at IQC to analyze the saturation effect. With 20 mV threshold, a more accurate mean pulse amplitude can be measured as SPADs with higher radiation dose saturates and triggers avalanche pulses more often during the recharge process, as explained in Section 4.3. V_{br}: Breakdown voltage, V_{bias}: Bias voltage, V_{ex}: Excess voltage ($V_{bias} - V_{br}$), DCR: Dark count rate, MPA: Mean pulse amplitude, OT: Operating temperature..

Module Identifier	May 3rd, 2017 (TRIUMF)						May 31st, 2017 (IQC)					
	OT (°C)	**V_{br} (V)**	**V_{bias} (V)**	**V_{ex} (V)**	**DCR (Hz)**	**MPA (mV)**	**OT (°C)**	**V_{br} (V)**	**V_{bias} (V)**	**V_{ex} (V)**	**DCR (Hz)**	**MPA (mV)**
LC-A	26.4	163.5	174	10.5	1593	117.4	22.3	161.2	171.7	10.5	79808	115.5
LC-B	26.4	164.4	174.9	10.5	84473	116.3	22.3	162.2	172.7	10.5	42699	109
LC-C	26.8	157	167.6	10.6	47011	124	23.5	154.7	165.3	10.6	84170	117
LC-D	26.8	167.5	178.2	10.7	113637	117	23.5	165.4	176.1	10.7	63848	112
LC-E	27	166.9	178	11.1	650	116.6	23.7	164.7	175.8	11.1	119525	99
LC-F	27	167.7	178.3	10.6	84288	114.6	23.4	165.9	176.5	10.6	62261	85
LC-G	27	160.8	171.9	11.1	27284	121.5	23.2	158.7	169.8	11.1	109819	111
LC-H	26.9	163	174.2	11.2	124526	116.8	23	160.7	171.9	11.2	103143	102.5
LC-I	27	157.7	168.3	10.6	3502	104	22.8	155.3	165.9	10.6	130997	97
LC-J	27	160.8	171.4	10.6	75534	116	22.8	158.1	168.7	10.6	72117	85.5
LC-K	27	161	172.1	11.1	5.87	109	23.3	158.8	169.9	11.1	96935	65
LC-L	27	157.1	168.2	11.1	27699	116.8	23.2	154.7	165.8	11.1	46580	65

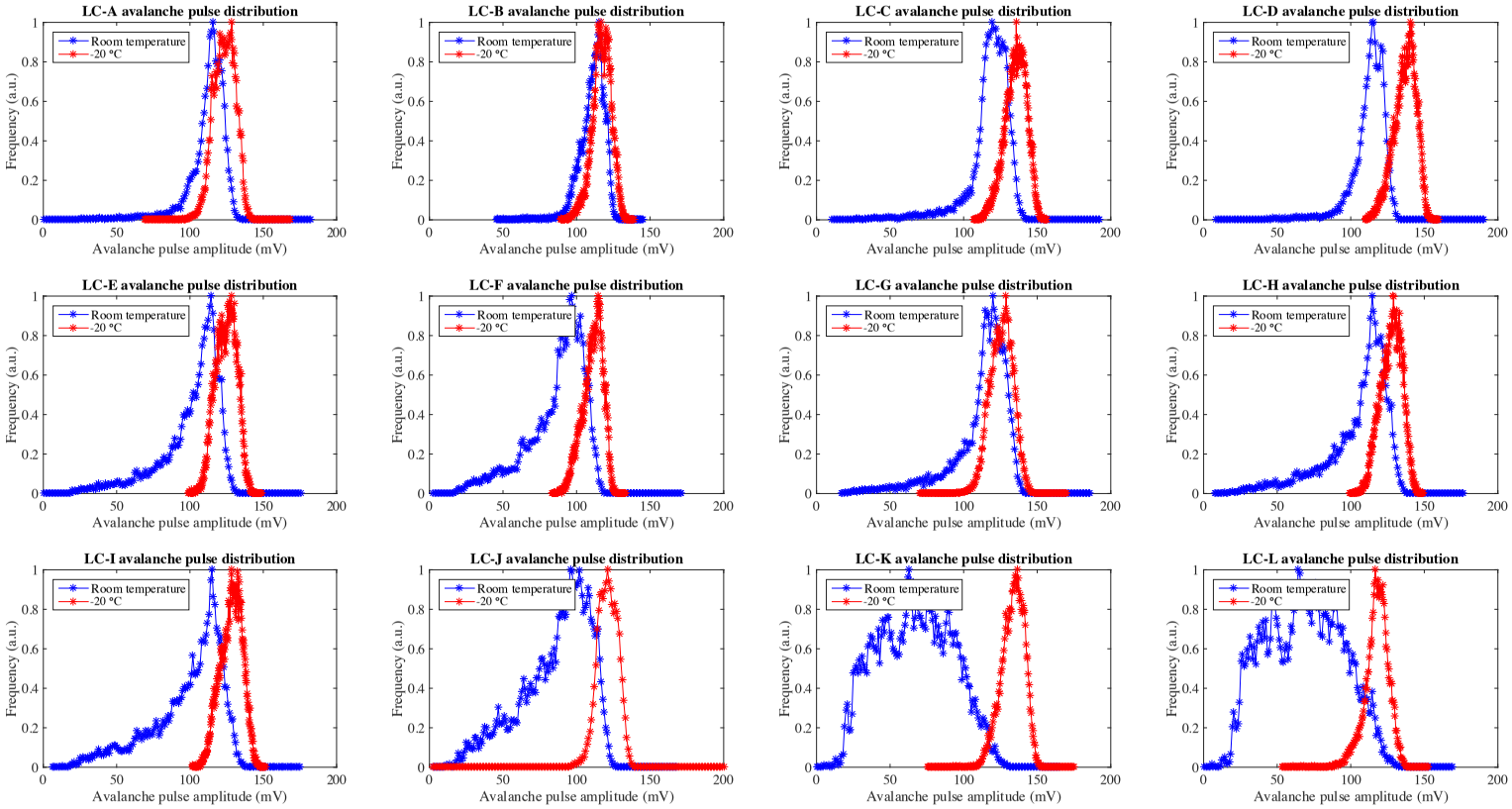

Figure 5.9: **Avalanche pulse distribution at room temperature and −20 °C from dark counts only.** Each avalanche pulse distribution curve is plotted from 20000 pulses. We can observe that the pulse amplitude distributions at −20 °C are all narrow because they are no longer saturated (see Table 5.5), while those at room temperature become wider and begin to have more smaller pulses as the radiation dose increases because newly created defect levels allow thermally excited electrons to trigger an avalanche pulse prematurely (see Section 4.3). These plots show why the reduced mean pulse amplitude informs that the detector has reached the saturation level or exceeded it. The pulse amplitude distribution measurement is a great method to verify whether the dark count rate reduction is real or whether the detector is over-saturated.

Table 5.5: **Characterization performed at −20 °C at IQC.** Platinum temperature sensor (Pt 100) connected to an industrial controller (JUMO dTRON) in 4-wire configuration monitors the temperature of the metal plate. The temperature during characterization is noted down as operating temperature. The trigger level is 20 mV for mean pulse amplitude measurement. V_{br}: Breakdown voltage, V_{bias}: Bias voltage, V_{ex}: Excess voltage ($V_{bias} - V_{br}$), DCR: Dark count rate, MPA: Mean pulse amplitude, OT: Operating temperature.

Module Identifier	IQC					
	Operating temperature (°C)	**V_{br} (V)**	**V_{bias} (V)**	**V_{ex} (V)**	**Dark count rate (Hz)**	**Mean pulse amplitude (mV)**
LC-A	−19.7	136.3	146.8	10.5	2677	123
LC-B	−19.7	137	147.5	10.5	1174	117
LC-C	−19.7	130.9	141.5	10.6	2159	134
LC-D	−19.7	140.2	150.9	10.7	1993	135
LC-E	−19.7	138.2	149.3	11.1	3854	125.5
LC-F	−19.7	139.2	149.8	10.6	5073	109
LC-G	−19.7	134.9	146	11.1	4303	125
LC-H	−19.7	135.3	146.5	11.2	5339	127
LC-I	−19.7	131	141.6	10.6	6149	127
LC-J	−19.7	133.3	143.9	10.6	8097	120.5
LC-K	−20.5	133	144.1	11.1	20249	132
LC-L	−20.5	131.1	142.2	11.1	17830	115

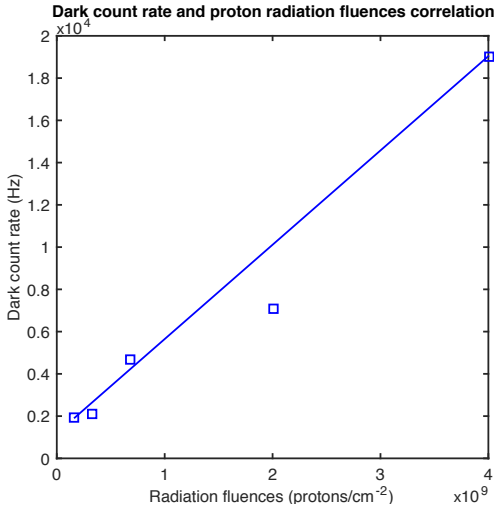

Figure 5.10: **Relationship between dark count rates and proton radiation fluences.** The solid line is a linear function that passes through the first and last data points. The dark count rate is characterized at $-20\,^{\circ}\mathrm{C}$.

Table 5.6: **Characterization of irradiated SAP300s performed by NUS.** These SAP300s were irradiated behind extra metal shielding. LC-M had 24 mm thick Aluminum was placed at the front of it, while LC-N and LC-O had 30 mm thick Titanium shielding in front of them.

Module Identifier	**DDD before extra shielding (MeV/g)**	**V_{br} (V)**		**V_{bias} (V)**		**Dark count rate (Hz)**	
		Before	After	Before	After	Before	After
LC-M	2.5×10^5	147.68	147.68	155.94	156.09	17373	18541
LC-N	5×10^5	148.97	148.71	157.18	158.04	16147	27241
LC-O	2.5×10^5	150.52	150.26	160.37	160.49	24647	27082

5.5 Conclusion

I estimated radiation dose for low-Earth-orbit missions for QEYSSat and ISS orbits. Through experiments, it is found that the dark count rate increase and proton fluences have a linear relationship and that proton radiation will eventually saturate silicon SPADs. Thus, radiation damage mitigation methods need to be developed. It is shown that cooling the detectors can exponentially decrease the dark count rate [70, 95, 98], but it does not undo radiation damages. The next chapter studies the feasibility of using silicon SPADs with built-in thermoelectric coolers for a 1-year mission inside one of the ISS vessels. The radiation test results by Anisimova *et al.* [70] and the SPENVIS software are utilized to analyze how much cooling is required and check if such cooling is practically feasible.

Chapter 6

Estimation of Radiation Damage inside the International Space Station for the Space-QUEST experiment

This chapter is based on a publication [107]. See Statement of Contributions.

6.1 Introduction

Space-QUEST [107] is a proposed fundamental physics experiment to test whether entangled photon pairs decohere when each photon travels at a different gravitational field gradient. The plan is to generate entangled photons on Earth and send one photon to a receiver located inside one of the International Space Station (ISS) vessels, where single-photon detectors are placed, and measure the other photon on Earth. Silicon Single-Photon Avalanche photoDiode (SPAD)s are potential candidates for single-photon detectors due to their performances and no need for cryogenic cooling. For the experiment, it is desirable to have Dark Count Rate (DCR) below 2000 Hz for useful data. However, in the previous chapter, it is shown that the space radiation environment damages silicon SPADs, so the radiation environment inside the ISS is estimated to study the feasibility of using them for the experiment. Although the mission duration is expected to be less than a year, a 2-year exposure is calculated to have a contingency margin.

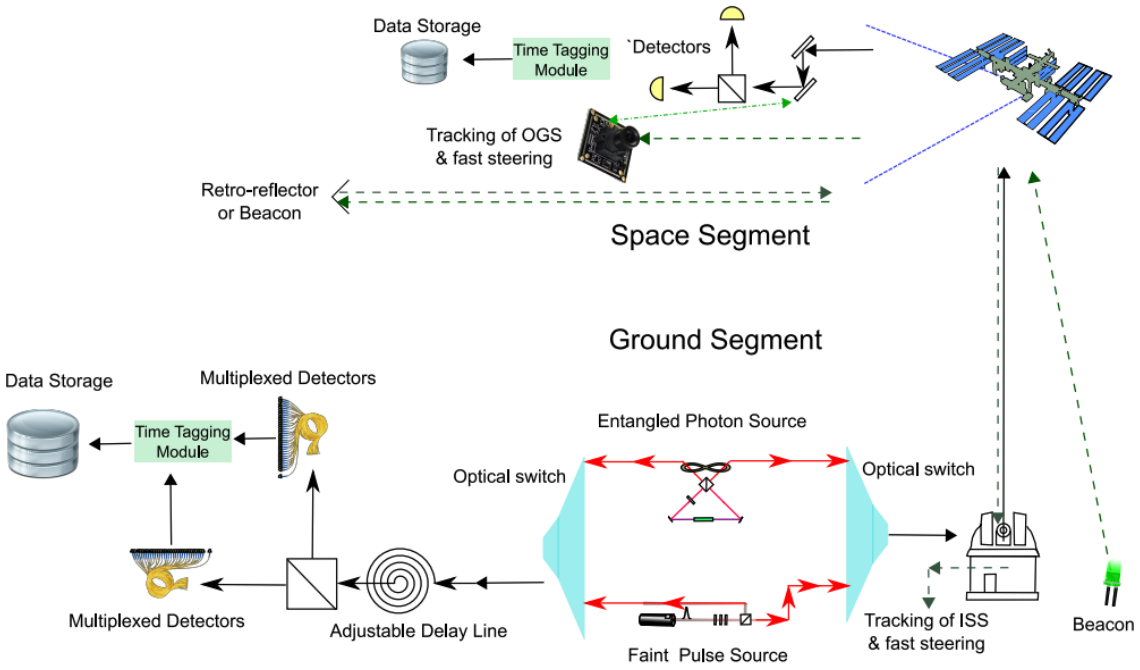

Figure 6.1: **Overall experiment scheme for Space-QUEST proposal [107].** The ground station prepares both entangled photon pairs and non-entangled faint pulse sources. A photon from the entangled pair is immediately measured at the ground station (in the same gravitational potential), and the other photon is transmitted to the ISS. Non-entangled faint pulse sources are also measured both at the ground station and at the ISS. The decoherence factor of the non-entangled faint pulse sources is zero, so if the entangled pairs exhibit gravitational potential decoherence, their results must be different from those of the non-entangled faint pulse sources.

6.2 Radiation dose calculation

The detector module with 20 mm thick spherical aluminum shielding is assumed. Storing it in a random place inside the ISS typically adds 10 mm additional shielding by the pressure vessel and micro-meteoroid orbital debris impact shield of the ISS [108, 109]. A total of 30 mm spherical aluminum shielding is considered. Using the SPENVIS software, total Displacement Damage Dose (DDD) after 2 years under these assumptions is calculated to be 1.27×10^6 MeV g^{-1}. While the calculated DDD monotonically decreases with increased shield thickness, it does not depend on it strongly for thicknesses that can reasonably be used in this mission. For example, doubling the total thickness to 60 mm would less than halve the DDD, while adding significant extra weight to the detector module.

The dark count rate estimates are based on proton irradiation tests reported by Anisi-

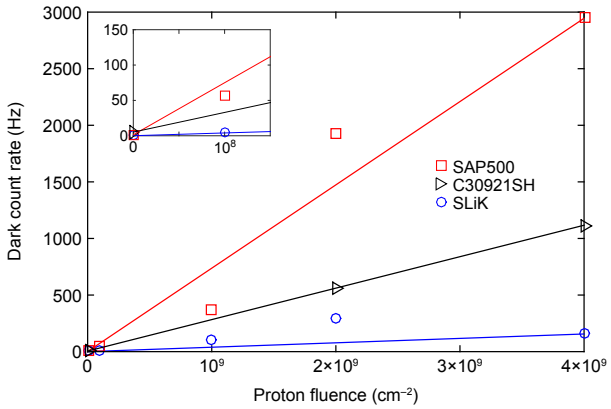

Figure 6.2: **Dark count rates of three different SPAD models at various radiation fluences at −86 °C [70].** Each data point is an average between the two samples tested. Linear fit lines pass through the first and last data points. The dark count rate increase appears to be linearly proportional to the proton fluence. Inset is a close-up of the first points.

mova *et al.* [70]. Test samples were irradiated by different proton fluences, as mentioned in Section 5.3.1. Two samples of each model were irradiated at each fluence, then their dark count rates were measured at 20 V above the breakdown voltages at several temperatures down to −86 °C (see Fig. 6.2). The increase of the dark count rate appeared to be roughly linear on the fluence, although some sample-to-sample variation was observed up to a factor of 2. Unpublished data at −60 °C yielded similar conclusions.

6.3 Estimation of required cooling temperatures

DDD value calculated above is equivalent to 5×10^8 cm^{-2} at 100 MeV monochromatic proton fluence using Eq. (5.2). For each fluence level, dark count rates of each silicon SPAD model is averaged out for −60 °C and −86 °C characterizations. Using the linear relationship found in Fig. 6.2, the dark count rate of each model is estimated for 5×10^8 cm^{-2} fluences for both temperatures. Taking into account the exponential dependence of the dark count rate on temperature [70], as shown in Fig. 6.3, the estimated dark count rates for each model for both temperatures are curved-fitted by the exponential function to estimate the SPAD temperatures required to reach the dark count rates of 200, 660, and 2000 Hz at the end of the 2-year mission. The results are listed in Table 6.1. However, sample-to-sample variations and uncertainty of radiation environment prediction [56] necessitate a reserve factor. The detector design needs to be able to cope with a factor of 3 worse dark count rates than predicted, which requires cooling by an additional ≈15 °C. Thus, to

guarantee dark count rate below 2000 Hz per SPAD, the detector module should be capable of cooling SLiK SPADs to −45 °C and C30921SH to −65 °C. At these temperatures, afterpulsing probability of SLiK and C30921SH is projected to stay below 1% [70]. These temperatures are achievable with thermoelectric cooling and forced-convection air radiator at room temperature [98]. However, cooling below −65 °C may require a more complex design, possibly using a compact Stirling cooler.

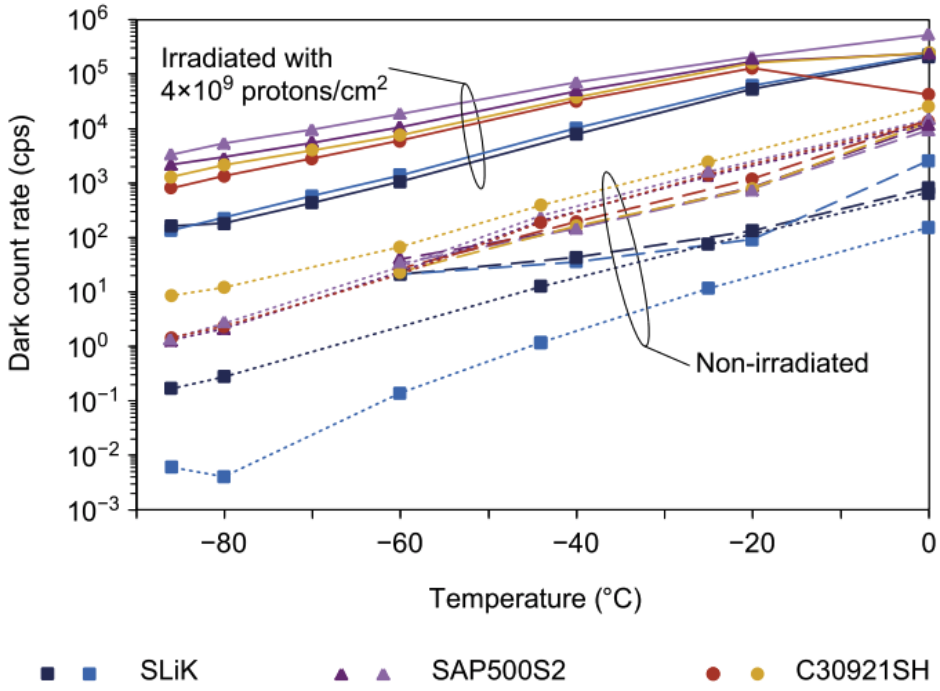

Figure 6.3: **Dark count rates of irradiated silicon SPADs as a function of operating temperatures (Reprinted from [70]).**

Table 6.1: **Estimated SPAD temperature required to reach various dark count rates after 2 years in orbit.**

SPAD model	200 Hz	660 Hz	2000 Hz
SLiK	−57.4 °C	−42.7 °C	−29.1 °C
C30921SH	−81.5 °C	−65.1 °C	−49.8 °C
SAP500	−95.6 °C	−77.1 °C	−59.9 °C

6.4 Conclusion

In summary, commercial thick-junction silicon SPAD chips from Excelitas appear to be a suitable choice for the ISS segment, given that Space-QUEST experiment can tolerate dark count rate of 1000–2000 Hz per detector. The detector module will need to use a custom thermal design and electronics [52, 98]. If a sufficient cooling system cannot be provided, implementing additional radiation damage mitigation methods can be considered. Anisimova *et al.* [70] showed that thermal annealing of irradiated silicon SPADs at up to 100 °C can repair some of the damage, resulting in up to 6.6-fold dark count rate reduction. In the following chapter, a new mitigation method called *laser annealing* is presented to heal radiation damages and achieve near pre-radiation dark count rates. The method is inspired by a separate study showing that a certain power range of focused laser illumination can lower non-irradiated SPAD dark count rates by up to 5.4 times [110].

Chapter 7

First Laser Annealing Experiments

This chapter is organized with the content from [111]. See Statement of Contributions.

7.1 Introduction

As described in Section 5.3.1 and Section 5.4.1, laser annealing is performed on nine irradiated Single-Photon Avalanche photoDiode (SPAD) (Excelitas SLiK, Excelitas C30902SH, and Laser Components SAP500S2). Laser annealing successfully decreases the dark count rates in all nine irradiated SPAD samples by a factor ranging from 5.3 to 758 when operated at −80 °C. Dark count rate reductions due to laser annealing can exceed those from thermal annealing. Notably, dark count rates are reduced even when laser annealing is applied to SPADs that were already thermally annealed. Laser annealing also affects other important photon counting parameters including photon detection efficiency, timing jitter, and afterpulsing probability, but the operation of quantum communications applications should not be significantly influenced by these changes.

7.2 Test samples

Some of Excelitas C30902SH, Excelitas SLiK, and Laser Components SAP500S2 devices used in the previous study [70] in Section 5.4.1 are tested. These were chosen as they are the only commercially available thick-junction SPAD models (thick-junction SPADs have higher detection efficiencies at the quantum signal wavelength around 785 nm, which makes them the most appealing for use on a quantum satellite receiver). All SPAD samples are hermetically sealed in glass-window packages and the photosensitive areas of C30902SH

Table 7.1: **Summary of detector samples, applied radiation, previous thermal annealing, and measured results of laser annealing.** The detectors are referred to by the given sample IDs throughout the paper. The highest reduction factor is the ratio between the reference dark count rate before any laser annealing and the lowest dark count rate after laser annealing—the corresponding laser power for this is also given. We include typical pre-radiation dark count rates of each model under the same bias and temperature conditions [70, 99].

Sample ID	**106 MeV proton fluence (cm^{-2})**	**Equivalent time in 600 km polar orbit (months)**	**Thermal annealing procedure**	**Dark count rate at −80 °C**				**Annealing power (W)**	**V_{excess} (V)**
				Before (Hz)	Lowest after (Hz)	Highest reduction factor	Typical for pre-radiation (Hz)		
C30902SH-1	10^9	6	None	347	2.3	150	∼ 5	0.8	14
C30902SH-2	10^9	6	None	363	2.64	137		1.5	14
SLiK-1	10^8	0.6	2 h @ 100 °C	6.71	0.16	41.7	< 1	1.4	14
SLiK-2	10^8	0.6	2 h @ 100 °C	2.19	0.42	5.3		0.8	14
SLiK-3	4×10^9	24	4 h @ 80 °C, 2 h @ 100 °C	43.1	2.09	21		1.4	14
SLiK-4	10^9	6	None	192	8.3	23		1.0	20
SLiK-5	4×10^9	24[a]	3 h @ 80 °C, 2 h @ 100 °C	447	58	7.7		1.0	20
SAP500S2-1	4×10^9	24	4 h @ 80 °C, 2 h @ 100 °C	1579	2.08	758	∼ 2	1.4	20
SAP500S2-2	10^8	0.6	2 h @ 100 °C	213	1.66	128		1.6	20

[a] Bias voltage is applied during proton irradiation.

and SAP500S2 are 500 µm in diameter, while that of SLiK is 180 µm in diameter. Table 7.1 presents the details of previous radiation testing and thermal annealing procedures performed on the test samples. These samples were stored in a −20 °C freezer before laser annealing experiments to prevent any spontaneous annealing at room temperature.

For every detector, the dark count rate after irradiation (and any thermal annealing) is so high that the devices are saturated when operating at room temperature. For this reason, all samples are characterized at −80 °C in the cold-temperature characterization apparatus. However, unlike the other devices, each Excelitas SLiK comes with a built-in thermistor and thermoelectric cooler (TEC), allowing additional testing to be performed in-situ in the laser annealing apparatus at an operating temperature of −30 °C.

The samples are held in detector modules, as shown in Fig. 5.6, with R1 replaced by 403 kΩ. (See Section 4.3 for the description of how the detector module works.) The dark count rate, relative changes in photon detection efficiency (P_{de}) (and absolute P_{de} for SLiKs characterized at −30 °C), and afterpulsing time distribution through the analysis of detection event times produced by a time-tagging unit with 156.25 ps resolution (UQDevices 16-channel model) are measured. Timing jitter (Δt_{jitter}) is measured using an oscilloscope (LeCroy 640Zi).

7.3 Experimental setup

Laser annealing apparatus

Figure 7.1(a) shows the laser annealing apparatus, which improves upon the laser annealing experimental setup of Ref. 110. Our apparatus allows us to laser-anneal SPADs, take pictures of their active areas, measure their dark count rates and P_{de}, and scan P_{de} across the entire active area to check whether laser annealing has produced any local damage.

Our setup consists of a single-mode (SM) continuous-wave 808 nm signal laser (QPhotonics QFLD-808-100S), and one multi-mode (MM) 0−30 W continuous-wave 808 nm annealing laser LD2 (Jenoptik JOLD-30-FC-12). The 808 nm wavelength is selected for the annealing laser to ensure that SPADs fully absorb photons in the depletion region and generate heat energy[1]. The output power from the weak coherent continuous-wave light

[1]Typical depletion region thickness of thick-junction silicon SPADs is 20−150 µm [95]. At 300 K, if the wavelength is too long (>1100 nm), the SPADs transmit most photons. If the wavelength is too short (<500 nm), most photons are absorbed only at the surface of the SPADs [112]. Absorption depth of 808 nm photons, at which the light intensity has fallen to $1/e$ of the initial value, is ∼10 µm [112].

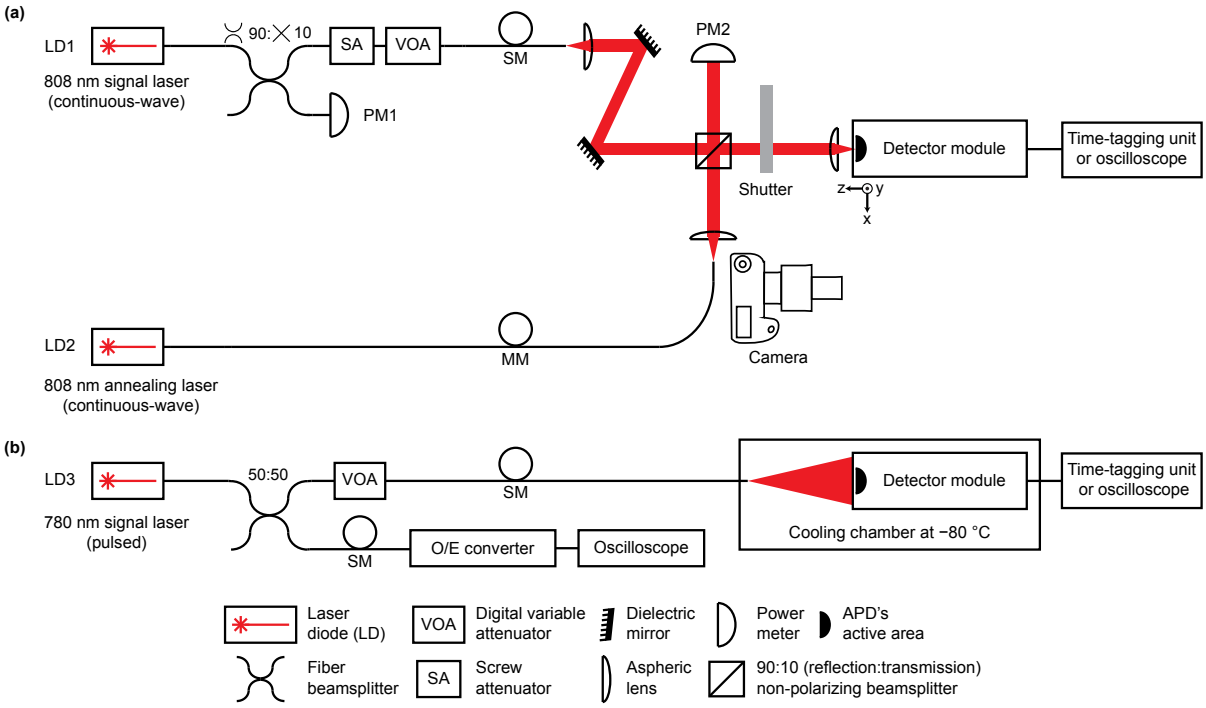

Figure 7.1: **Experimental setup.** (a) Setup for laser annealing and characterization at room temperature. (b) Setup for characterization at −80 °C. In (a), LD1 and LD2 are overlapped such that high-power laser from LD2 can be focused on the active area by focusing LD1 onto it. LD1 is also used for measuring SLiKs' photon detection efficiency. The detector module is mounted on an XYZ translation stage, which can move between the laser setup and camera. The free-space portion of the setup is enclosed in a light-tight box. In (b), diverging weak coherent pulses are applied on SPADs for full characterization. SM: single-mode optic fiber; MM: multi-mode optic fiber; O/E: optical-to-electrical.

source (LD1) is calibrated in the following way to apply the mean photon count rate of 48.8 kHz at the sample's active area. The pigtail of the signal laser LD1 is connected to a 90:10 fiber beamsplitter (Thorlabs FC780-90B FC). One output port is connected to a power meter (PM1; OZ Optics POM-300-VIS) to continuously monitor the output power from LD1, while the other output port is connected to two attenuators in series. First, by monitoring the optical power at the detector module, a screw attenuator (SA) is set to reduce the laser power to the nW range. The ratio of the power measured at PM1 and that at the detector module gives SA's attenuator amount. Then, a digital variable optical attenuator (VOA) (OZ Optics DA-100-35-770/830/850-5/125-5-40-LL) is set between 40−50 dB to bring the laser illumination down to the single-photon level. Now, the mean photon count rate at the detector module can be controlled by monitoring PM1 and VOA's attenuation amount. The attenuated continuous-wave laser beam is sent to a collimation setup in SM fiber, then collimated by an aspheric lens (Thorlabs C280TME-B) and reflected off two dielectric mirrors (Thorlabs BB1-E03-10) to provide four degrees of freedom for alignment. It then goes through 90:10 (reflection:transmission) non-polarizing beamsplitter (Thorlabs BS029 90:10), a mechanical shutter (Thorlabs SH05 with Thorlabs SC10 controller), a focusing lens (Thorlabs C220TME-B), and reaches the SPAD.

The continuous-wave annealing laser LD2 is coupled to a 200 µm diameter core MM fiber (RPMC Lasers OAL-200/220/245). The annealing laser beam is collimated by an aspheric lens (Thorlabs C220TME-B) and reflected at the 90:10 non-polarizing beamsplitter. The beams of the annealing and signal lasers overlap so that both can be focused on the same spot. A power meter (PM2; Thorlabs S142C) located in the transmission arm of the annealing laser allows us to accurately control the annealing power at the SPAD.

A camera (Canon 7D with macro lens MP-E 65 mm f/2.8 1–5x) and a light-emitting-diode photography illuminator are mounted beside the laser setup. The XYZ translation stage, on which the detector module is mounted, enables us to move the samples between the laser setup and the camera.

Cold-temperature characterization apparatus

A separate apparatus, shown in Fig. 7.1(b), is built to measure the dark count rate, relative changes in P_{de}, $\Delta t_{\mathrm{jitter}}$, and afterpulsing probability at −80 °C. The low temperature significantly suppresses thermally excited dark counts [70]. The detector module is extracted from the laser annealing apparatus and placed inside a cooling chamber (Delta Design 9023) at −80 °C.

The apparatus necessary to measure the absolute P_{de} cannot fit in the cooling chamber;

consequently, we measure P_{de} relative to a reference by sending diverging weak coherent pulses (WCPs) from the end of a fiber onto the SPADs. Each SPAD's active area is sufficiently small that it receives approximately uniformly distributed light intensity, despite the overall Gaussian profile of the incident optical mode. We use a 780 nm laser LD3 (PicoQuant LDH 8-1) as the WCP source, pulsed at 40 MHz with full width at half maximum (FWHM) of 188 ps. The laser pulses are split by a 50:50 fiber beamsplitter (Thorlabs FC780-50B-FC). One output port is connected to a digital variable attenuator (OZ Optics DA-100-35-770/830/850-5/125-5-40-LL) and sends the laser pulses through a fiber to the SPADs placed inside the cooling chamber. The other output port is connected to an optical-to-electrical converter (LeCroy OE455, DC–3.5 GHz) and the oscilloscope. Having oscilloscope access to both input laser pulses and output avalanche pulses allows us to measure Δt_{jitter} (which requires using a pulsed laser, as opposed to continuous-wave such as LD1).

7.4 Laser annealing process

To perform laser annealing, the detector module is positioned to ensure that the high-power annealing laser beam is focused on the active area of a SPAD. (The FWHM beam diameter is 92 µm.) Next, the desired annealing power is set by monitoring the power meter PM2 with the shutter closed. We then open the shutter and laser-anneal the SPAD for 60 s, immediately afterwards closing the shutter and letting the device cool down to the room temperature for another 60 s. We then perform characterization.

For most samples, we perform multiple stages of laser annealing and characterization, with laser power increased between each stage. To determine whether this stepwise laser annealing process has any additional effects, we apply only a single-shot power of 1 W to SLiK-4 and SLiK-5 for comparison (1 W is chosen based on observed results of the first three SLiKs to ensure a dark count rate reduction). Similarly, C30902SH-2 is laser-annealed at two specific powers, chosen based on C30902SH-1's observed results.

The temperatures reached by the SPADs during laser annealing are of interest because, for some temperature ranges, alternative heating methods may be more practical to implement on a satellite (e.g., using an electric heater). We can measure the temperature of SLiK samples using their integrated thermistor (mounted on the cold plate of TEC, close to the SPAD). The temperature of SLiK-1's thermistor is recorded at the end of the 60 s exposure, for most annealing powers. According to our measurements (see Chapter A), the thermal resistance between the photodiode chip and thermistor is negligible; thus, the

temperature reading by the thermistor provides an accurate reading of the temperature reached by the SPAD during laser annealing.

7.5 Characterization

All nine samples' parameters are measured at −80 °C in the cold-temperature characterization apparatus, while SLiKs are also characterized at −30 °C (reached using their built-in TECs) in the laser annealing apparatus.

Breakdown voltage. V_{br} is measured by observing avalanche pulses on an oscilloscope. As V_{bias} is gradually increased from 0 V, avalanche pulses begin to appear when V_{br} is reached. We estimate the accuracy of this V_{br} measurement to be better than ±0.3 V. This measurement is performed at the start of every full characterization. Both C30902SH samples and SLiK-1, SLiK-2, and SLiK-3 are subsequently biased 14 V above V_{br}, whereas SLiK-4, SLiK-5, and both SAP500S2 samples are biased 20 V above V_{br}. The choice of V_{excess} is arbitrary; however, we change V_{excess} values to explore its effects on laser-annealed SPADs.

Dark count rate. Dark counts are recorded with the time-tagging unit for 500 s. The mean dark count rate is calculated by dividing total number of recorded dark counts by 500 s. We define the dark count rate reduction factor as the ratio between the reference mean dark count rate before any laser annealing and the mean dark count rate after laser annealing. Some of the samples were already thermally annealed in another experiment [70]; thus, having further dark count rate reduction in those samples imply that laser annealing mitigates proton radiation damage better than thermal annealing.

Photon detection efficiency. To measure relative P_{de} at −80 °C in the cold-temperature characterization apparatus using diverging WCPs, we take the mean count rate over 500 s. Following the completion of laser annealing and measurements of the two C30902SH samples, it was discovered that the output power of LD3 varies over time. As the C30902SH samples have undergone laser annealing, measurements unfortunately cannot be retaken. Consequently, for all other samples, we normalize the count rate by the average laser power (measured at the oscilloscope immediately before and after a measurement). We then calculate the relative change in P_{de} by subtracting the mean dark count rate and then normalizing against the initial photon count rate.

For SLiKs we determine the absolute P_{de} while operating at −30 °C in the laser annealing apparatus. The continuous-wave signal laser LD1 is applied, with its photon rate calibrated via loss and laser power measurements in our optical setup. Then, we measure a

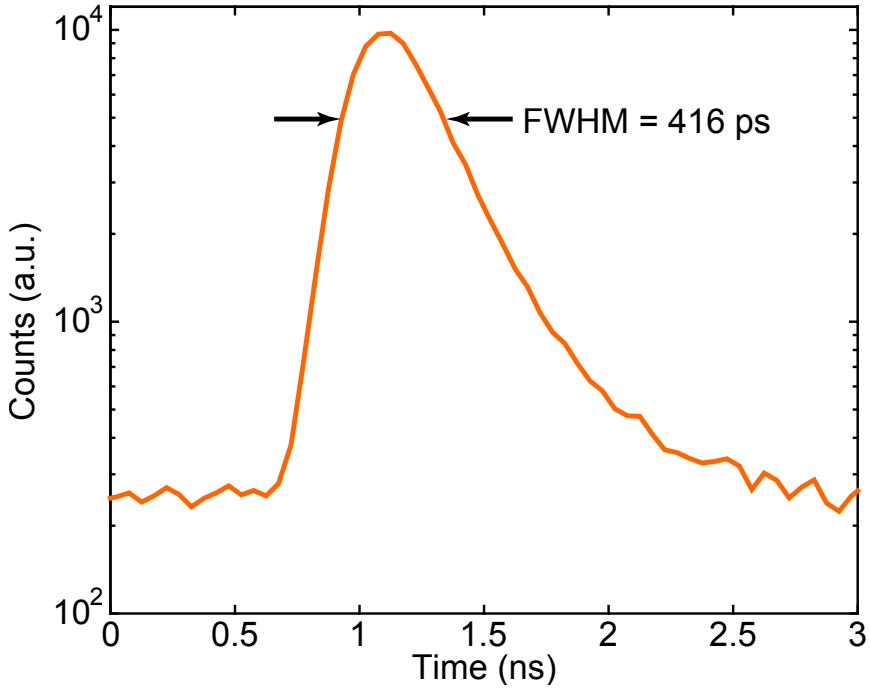

Figure 7.2: **Measuring the timing jitter of SAP500S2-2.** We measure the relative time difference between laser pulses and SPAD output pulses over at least 10^5 output pulses, and plot these as a histogram. Δt_{jitter} is the width of the pulse peak.

mean count rate over 500 s using the time-tagging unit. Subtracting the mean dark count rate from the mean count rate and dividing the difference by the calibrated input photon rate gives P_{de}.

Testing within the laser annealing apparatus also allows us to scan P_{de} at various points over the active area of the SLiK devices. We measure the signal laser's illumination spot size using a beam profiler—the beam waist is ∼20 µm (FWHM). We thus step the translation stages in 10 µm increments, such that P_{de} of the active area is fully and tightly covered. We scan a square region that covers the active area, with appropriate pauses at each step for vibration dissipation.

Timing jitter. To measure Δt_{jitter}, both the laser output pulses and the SPAD's avalanche pulses are connected to the oscilloscope. We then plot a histogram of the relative time difference between these two signals over at least 10^5 avalanche pulses (see example in Fig. 7.2), and measure the FWHM.

Afterpulsing probability. Afterpulsing probability is calculated from time-stamped counts. We typically use dark counts, but if the dark count rate for an SPAD is too low, we use a dim light pulsed at 100 Hz to facilitate a measurement. The extra light increases

the background count rate by a few Hz (otherwise, the background count rate tracks the SPAD's dark count rate), and does not influence the afterpulsing distribution. A detailed description of how the afterpulsing analysis software operates is explained in Section 4.4.4.

For a quantum communications protocol such as Quantum Key Distribution (QKD), the afterpulsing peak, shown in Fig. 4.8, contributes to the Quantum Bit Error Rate (QBER), and it is thus desirable to remove the peak by extending the dead time out to the flattened region [84, 85, 95]. In practice, this can be performed by discarding all counts before the end of a user-selected dead time in post-processing [113, 114] or by using an active quenching circuit [115]. Such additional dead time, however, limits the maximum detection rate [84, 86]. Because long distance transmissions reduce the expected detection rate [47], the amount of additional dead time could be optimized to balance the QBER with the detection rate to maximize the final key rate [99, 113, 114].

7.6 Results and Discussion

Right half of Table 7.1 summarizes the laser annealing results for the maximum dark count rate reduction. Detailed results for each SPAD model follow.

Excelitas SLiK. Figure 7.3 shows characterization results for the five SLiKs. The maximum dark count rate reduction ranges from 1.3 to 10 times when operating at −30 °C, and from 5.3 to 41.7 times at −80 °C. Importantly, the SLiKs that were previously thermally annealed exhibit further dark count rate reduction after laser annealing. SLiK-4 and SLiK-5, after a single exposure at 1 W, still show a significant decrease in the dark count rate. 1 W may not give the highest reduction factor but it shows that the single exposure and stepwise annealing processes induce comparable dark count rate reduction factors. Thus, the stepwise process can be used on a SLiK to find the optimal annealing power and a single exposure at this power on other SLiKs under similar conditions should achieve comparable dark count rate reduction.

P_{de} of each SLiK did not change significantly, and a spatial scan in Fig. 7.4 shows that photosensitivity across the active area is not altered by high-power laser annealing. V_{br} and $\Delta t_{\mathrm{jitter}}$ also do not fluctuate much after laser annealing. SLiK-4's and SLiK-5's $\Delta t_{\mathrm{jitter}}$ are lower than those of other SLiKs due to the 6 V difference in V_{excess} [95].

The afterpulsing probability results are interesting. Proton radiation mainly causes displacement damage in SPADs [116]. Highly energetic protons displace atoms from their lattice structures, producing extra energy levels in the bandgap (defects). The defects near the mid-bandgap contribute to thermally generated dark counts, while those near the

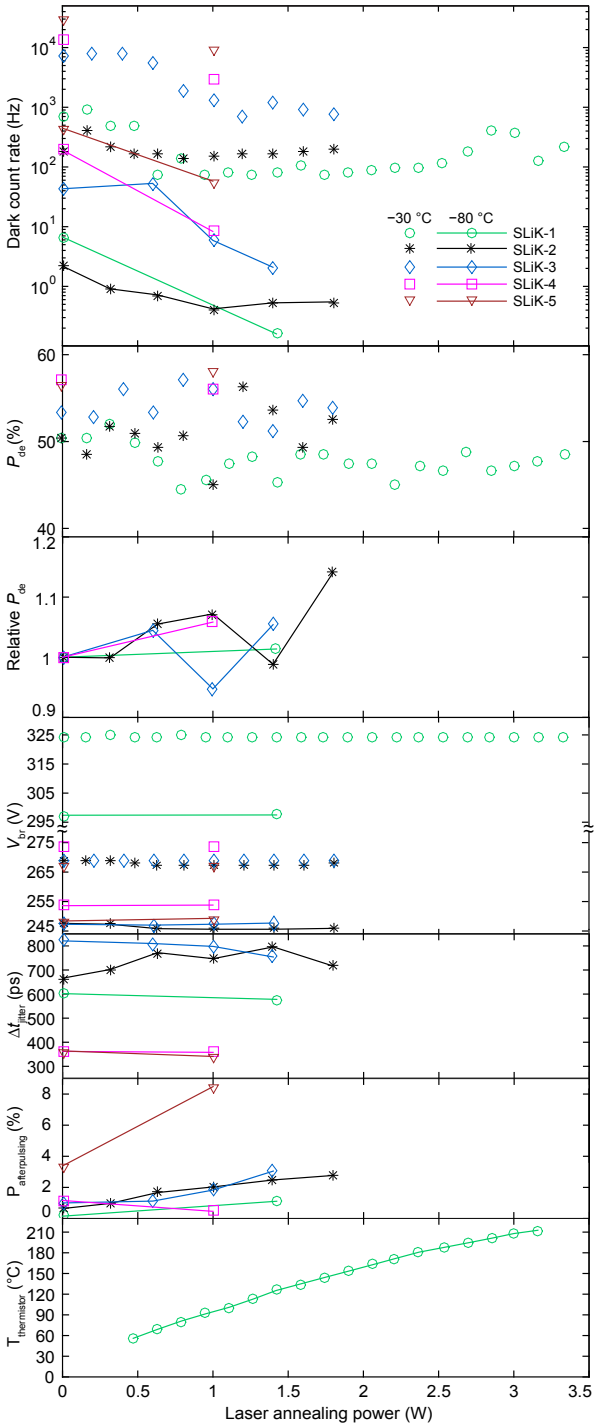

Figure 7.3: **Characteristics of SLiK SPADs after laser annealing.** Points at zero power show the initial characteristics before laser annealing. The samples have been characterized at −30 °C after every annealing stage (data represented by points without lines), and additionally characterized at −80 °C after some of the steps (points connected with lines). The dark count rate is averaged over 500 s only once, but it is known to follow the Poisson distribution so the standard deviation is simply the square root of the mean value.

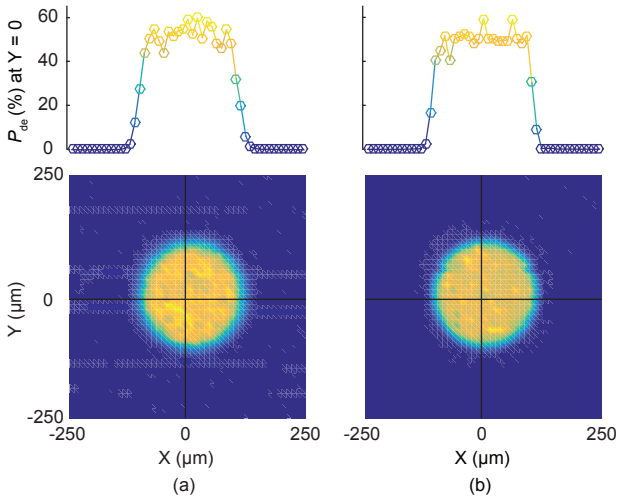

Figure 7.4: **Detection efficiency scan of SLiK-1.** (a) Prior to annealing, and (b) after 3.3 W annealing. The spatial profile is essentially unchanged, proving that focused high-power laser illumination does not degrade photosensitivity in the active region of the SPAD for the power range we tested. The plots at the top are the cross sections at Y = 0.

conduction band are called trap levels that cause afterpulses. After proton irradiation, SLiKs' dark count rates are significantly increased but the afterpulsing probabilities are still low [70], implying that the displacement damage by 106 MeV protons at the depletion region mainly produces thermal generation centers [116]. Although the dark count rate is reduced in all samples after laser annealing, the afterpulsing probability increases in most of them. This also implies that laser annealing not only removes thermal generation centers but also simultaneously creates extra trap levels. The increased afterpulsing probability can be handled by imposing additional dead time (see Section 7.5).

When the high-power laser is applied to SLiK-1, its thermistor temperature rapidly increases in the first 30 s. The temperature continues to rise at a slower rate in the second half of the 60 s exposure until it reaches the peak temperature in the last 2–3 s. The peak thermistor temperature at each annealing power is plotted in Fig. 7.3. The SLiKs we have tested experience a significant dark count rate reduction at annealing power of 1 W. Assuming the thermal resistance between SLiK-1's thermistor and the SPAD is negligible (see Chapter A), 1 W of power anneals the SPAD at peak temperature of ∼90 °C. The peak temperature is reached only in the last few seconds, but we speculate that it determines the dark count rate reduction factor. If this is the case, our results imply that laser-annealing of irradiated SLiKs at the peak temperature of ∼90 °C for 60 s leads to a higher dark count rate reduction than thermally annealing them at 100 °C for two hours [70] (see Table 7.1). The observed discrepancy in the dark count rate reduction suggests that light

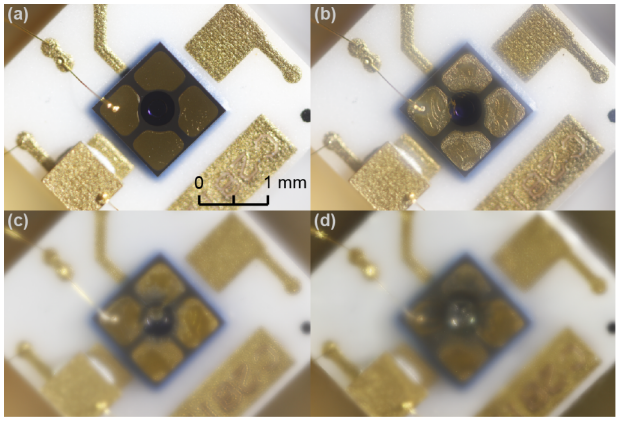

Figure 7.5: **Progressive destruction of SLiK-1.** The sample is exposed to laser power of (a) 3.5 W, (b) 5.2 W, (c) 7.7 W, and (d) 9.0 W. The photodiode stopped working as a single-photon detector after annealing at 3.5 W. From 3.6 W, the gold plating surrounding the active area of the SPAD begins to degrade and flow into the active area at higher powers. The package window becomes foggy from 4.9 W. The SPAD chip starts shifting downwards from 6 W and has moved by ≈30 µm overall.

may play a greater role than simply providing the heat energy in improving irradiated SLiKs' performance.

For SLiK-1, we continue to test at higher powers. Fig. 7.5 shows the gradual change in the appearance of SLiK-1's active area. Fig. 7.5(a) does not show any visible physical destruction, but the device has already stopped working as a single-photon detector after annealing at 3.5 W. In Fig. 7.5(b)–(d), damage becomes visible. It appears that an epoxy layer between two ceramic plates has boiled and condensed on the package window, causing it to become opaque. We did not remove the blurry detector window because it may change illumination power calibration and cause oxidation due to exposure of the hermetically sealed package (filled with nitrogen gas) to the atmosphere. (SLiK's detailed mechanical structure can be seen in Fig. 5 of Ref. 117. Clear images of C30902SH's physical destruction are shown in Fig. 4 of Ref. 110.)

Excelitas C30902SH. Figure 7.6 shows characterization results for the two irradiated C30902SHs. Similar to the SLiKs, C30902SH-1 is laser-annealed and characterized at multiple stages, but C30902SH-2 is treated at two specific powers, chosen based on C30902SH-1's results. The samples experience the maximum dark count rate reduction of 150 times and 137 times at −80 °C. They recover typical pre-radiation dark count rates. Again, the stepwise process does not show any additional improvements on the dark count rate when compared to the single exposure process.

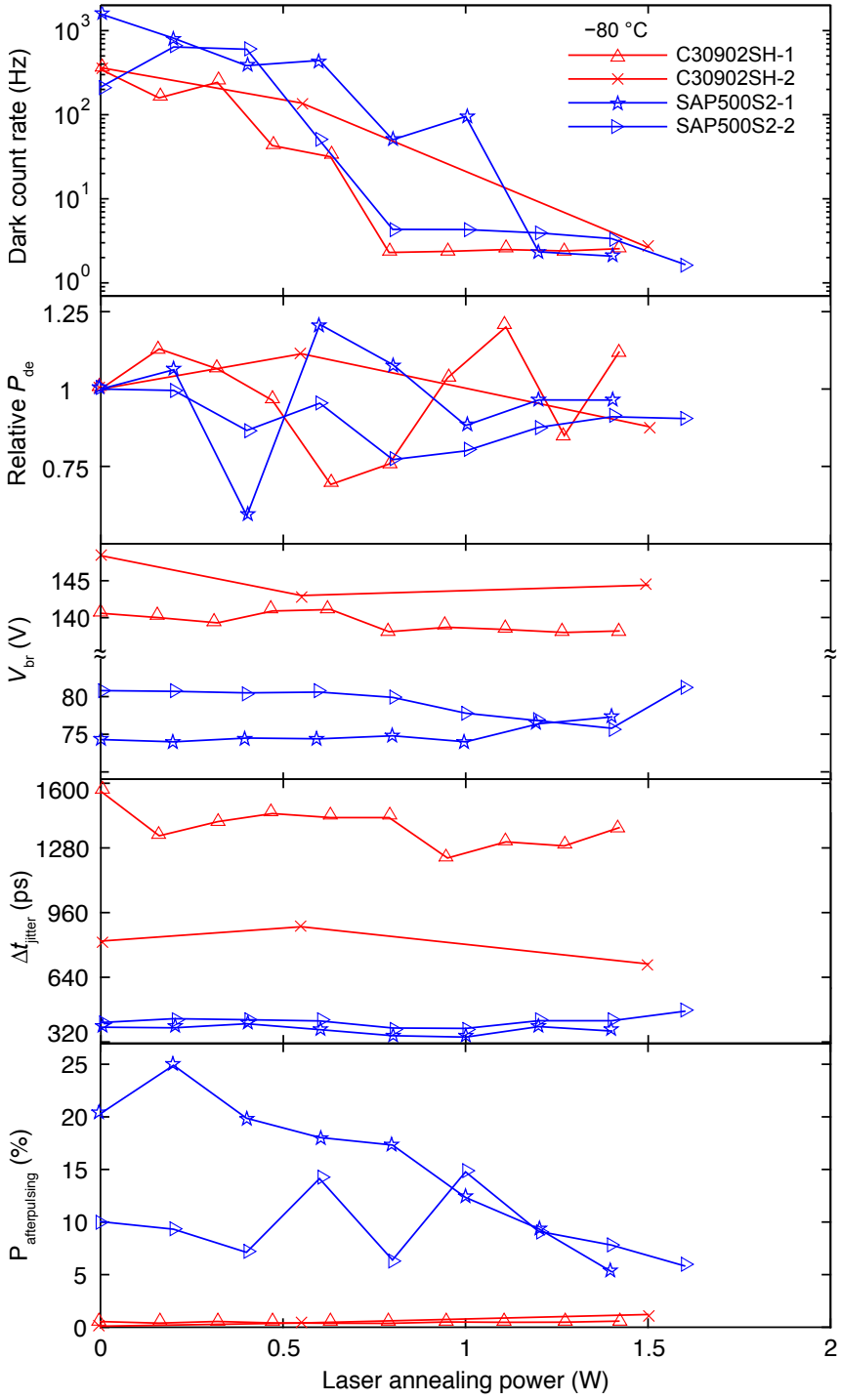

Figure 7.6: **Characteristics of C30902SH and SAP500S2 SPADs after laser annealing.** Points at zero power show the initial characteristics before laser annealing. Each point shows a measurement after successive laser illumination power. The dark count rate is averaged over 500 s only once, but it is known to follow the Poisson distribution so the standard deviation is simply the square root of the mean value.

Relative P_{de} measurement for C30902SHs is inaccurate due to the fluctuation of the laser output power (which we normalize out for measurements of the other devices; see Section 7.5). Due to the variation observed, it is difficult to draw any conclusions. V_{br} and Δt_{jitter} do not change significantly. Afterpulsing probabilities are negligible in C30902SHs, which also implies that thermal generation centers are the main contributors to dark counts after irradiation. We stop testing these C30902SHs before they show signs of damage—testing non-irradiated C30902SHs at higher powers was done in Ref. 110.

Laser Components SAP500S2. Unlike SLiKs, SAP500S2s cannot withstand high-power illumination. SAP500S2-1 and SAP500S2-2 fail to work as single-photon detectors after laser annealing at 1.6 W and 1.8 W, respectively. Both SAP500S2s (see Fig. 7.6) exhibit the maximum dark count rate reduction just before they stop working as a single-photon detector (the reduction factor of 758 times for SAP500S2-1 and 128 times for SAP500S2-2). SAP500S2s have the highest dark count rate after proton irradiation [70] and such high reduction factors prove that laser annealing is more effective than thermal annealing. The lowest dark count rates after laser annealing ($\approx$2 Hz) are at typical pre-radiation values.

Relative P_{de} varies for different laser annealing powers. Unlike C30902SH measurements, the photon count rate here is normalized to the laser source's average power for every characterization, so the observed variation is real. To avoid P_{de} fluctuation and achieve sufficiently low dark count rate, one should perform laser annealing around 1 W.

V_{br} seems to decrease slightly, and then increase just before each SAP500S2 stops working as a single-photon detector. An increase in V_{br} may be an indication that the maximum laser annealing power is reached. Δt_{jitter} remains almost constant and it is low compared to C30902SHs because SAP500S2s are biased an extra 6 V (for a $V_{\text{excess}} = 20$ V) above a significantly lower V_{br}.

While SLiKs and C30902SHs display a marginal increase in afterpulsing probability as the laser power increases, the afterpulsing probability is reduced in SAP500S2s (afterpulsing probability did not change much after proton irradiation [70]). Although these reductions are insignificant compared to the highest dark count rate reduction factor in Table 7.1, the results imply that laser annealing reduces both trap levels and thermal generation centers at the same time. The overall results suggest that the materials used to manufacture SAP500S2s are more susceptible to the high energy damages induced by protons and the annealing laser.

Although high-power laser exposure can be helpful for reducing SPAD dark counts, it also has the potential to damage components, such as classical photodiodes and pinholes,

in quantum communication systems [118]. Such changes to the apparatus may invalidate assumptions—most notably, within the security analysis for implementations of QKD, which could lead to exploitable side-channels. However, having a reduction in dark counts does not benefit the eavesdropper because QKD security proofs attribute all losses and errors to the eavesdropper while assuming Bob's apparatus to be error-free [119].

The laser annealing apparatus could be reduced in complexity for implementation as part of a satellite payload; however, a high-power laser is still required. Further research is needed to understand the physical phenomena behind the dark count rate reduction, and determine whether the specific properties of laser light are fundamentally necessary to achieve the gains observed here.

7.7 Conclusion

Our experimental results demonstrate that laser annealing can remedy calculated low Earth orbit radiation damage for three different types of SPADs. The dark count rate of all samples, including the samples that were previously thermally annealed, is greatly reduced. Several of them have their dark count rates recovered to typical pre-radiation levels. This suggests that laser annealing is a more effective method than thermal annealing. The observed fluctuations in other photon counting parameters should not degrade the performance of quantum communication applications. We speculate that laser annealing heals the crystal lattice structure defects, thermal generation centers in particular, created by proton radiation. The following chapter explores different laser annealing methods to try to understand the mechanisms of the laser annealing effect and directly compares the reference, post-irradiation and post-laser-annealing dark count rates of silicon SPADs.

Chapter 8

Second Laser Annealing Experiments

8.1 Introduction

In our second round of laser annealing experiments, we explored different aspects of laser annealing. First, by performing full cycle of characterizations and tests from pre-radiation state to post-irradiation to laser annealing procedure, the dark count rate can be directly compared to verify whether it returns to pre-radiation values. Second, different laser annealing methods are explored in an attempt to identify the causes of the laser annealing effect and to seek methods that would give a similar dark count rate reduction factor with lower optical power. Next, one sample is annealed with forward-bias current for 1 hour at a time to check if it can also reduce the dark count rate. Finally, a few samples are characterized several times over ≈60 hours after each laser annealing exposure to observe if the effect is permanent.

8.2 Test samples

The conditions of 12 samples are described in Section 5.3.2 and Section 5.4.2. Of 12 samples that were irradiated at TRIUMF in Table 5.3, 10 samples, excluding LC-J and LC-L, are tested. LC-A, LC-C, LC-E, LC-I, and LC-K are laser-annealed in the same way as the initial laser annealing: applying the high-power continuous-wave laser for 60 s. LC-G is laser-annealed for 180 s continuously. LC-B, LC-D, and LC-H are laser-annealed in duty cycle mode, in which the high-power laser is modulated by an optical chopper with 50% duty cycle at 1.5 kHz, placed before the beam splitter in Fig. 7.1(a). LC-F is

annealed by forward-bias current. In addition, LC-M, LC-N, and LC-O that were irradiated by Prof. Alexander Ling's group at the National University of Singapore (NUS) are also laser-annealed using the 60 s illumination method and are tested for permanency by characterizing them every 2 hours for the first 6 hours and then every 8−13 hours for the following two days, after each laser annealing exposure.

8.3 Experimental setup

Experimental setups used for laser annealing and characterization are the same as Fig. 7.1.

8.4 Characterization

The cold-temperature apparatus shown in Fig. 7.1(b) is used to characterize the detectors at 22 °C, −20 °C, and −80 °C.

Breakdown voltage. Breakdown voltage (V_{br}) is measured by observing avalanche pulses on an oscilloscope as described in Section 7.5. However, instead of having a fixed V_{excess}, each detector has a different value as it was chosen in the initial characterization performed by NUS in Table 5.3 and Table 5.6 .

Dark count rate. Dark counts are recorded with SR-400 photon counter from Stanford Research Systems for 600 s. The mean dark count rate is then calculated by dividing the total count by 600 s. The dark count rate reduction factor is defined as the ratio between the reference mean dark count rate before any laser annealing and the mean dark count rate after laser annealing.

Mean avalanche pulse amplitude. Mean avalanche pulse amplitude is measured over 2000 pulses on an oscilloscope with 5 mV trigger level to quickly check if a detector is saturated or not.

Avalanche pulse amplitude distribution. 20000 avalanche pulses' amplitudes are categorized in a histogram to confirm detector saturation with 5 mV threshold level.

8.5 Results and Discussion

Table 8.1 shows proton radiation damage level for the samples treated with 60 s continuous laser annealing. A sample from each fluence group is selected to check if the annealing effect

is applicable to all fluence groups. Figure 8.1 shows V_{br} and dark count rate measurements after each annealing power. Laser annealing was not performed at higher power because LC-A, LC-E, LC-I, and LC-K became foggy after 1200 mW exposure. For operations at 22 °C and −20 °C, LC-A, LC-C, LC-E, and LC-I reach similar dark count rates after 800 mW or 1000 mW annealing, but the dark count rate of LC-K cannot be reduced to that level. Therefore, it is recommended to laser-anneal detectors before exceeding total radiation damage of 4×10^9 proton fluences @ 100 MeV. For −80 °C, the dark count rate of every sample after laser annealing is below 0.1 Hz, so the detectors should be laser-annealed at any time for better performance.

Table 8.2 summarizes the results of full radiation and laser annealing cycle. The dark count rate of all samples are reduced to a level close to pre-radiation values. Figure 8.2 proves that the dark count rate has truly returned to pre-radiation values because the shape of the pulse distribution is no longer distorted. For these samples, 800 mW would be the best choice for 22 °C and −20 °C, while 1200 mW is good for −80 °C.

Table 8.1: **Characteristics of SAP300s tested for 60 s continuous laser annealing.** ISS orbit is 400 km low Earth orbit with the inclination angle of 51.64°, while QEYSSat orbit is a heliosynchronous 600 km noon-midnight orbit. 1.8 mm aluminum shielding is chosen for the ISS orbit, while 10 mm aluminum shielding is selected for the QEYSSat orbit.

Module Identifier	**Target fluence @ 100 MeV (p/cm²)**	**Equivalent mission duration at ISS orbit (months)**	**Equivalent mission duration at QEYSSat orbit (months)**
LC-A	1.66×10^8	3	1
LC-C	3.32×10^8	6	2
LC-E	6.73×10^8	12	4
LC-I	2×10^9	36	12
LC-K	4×10^9	72	24

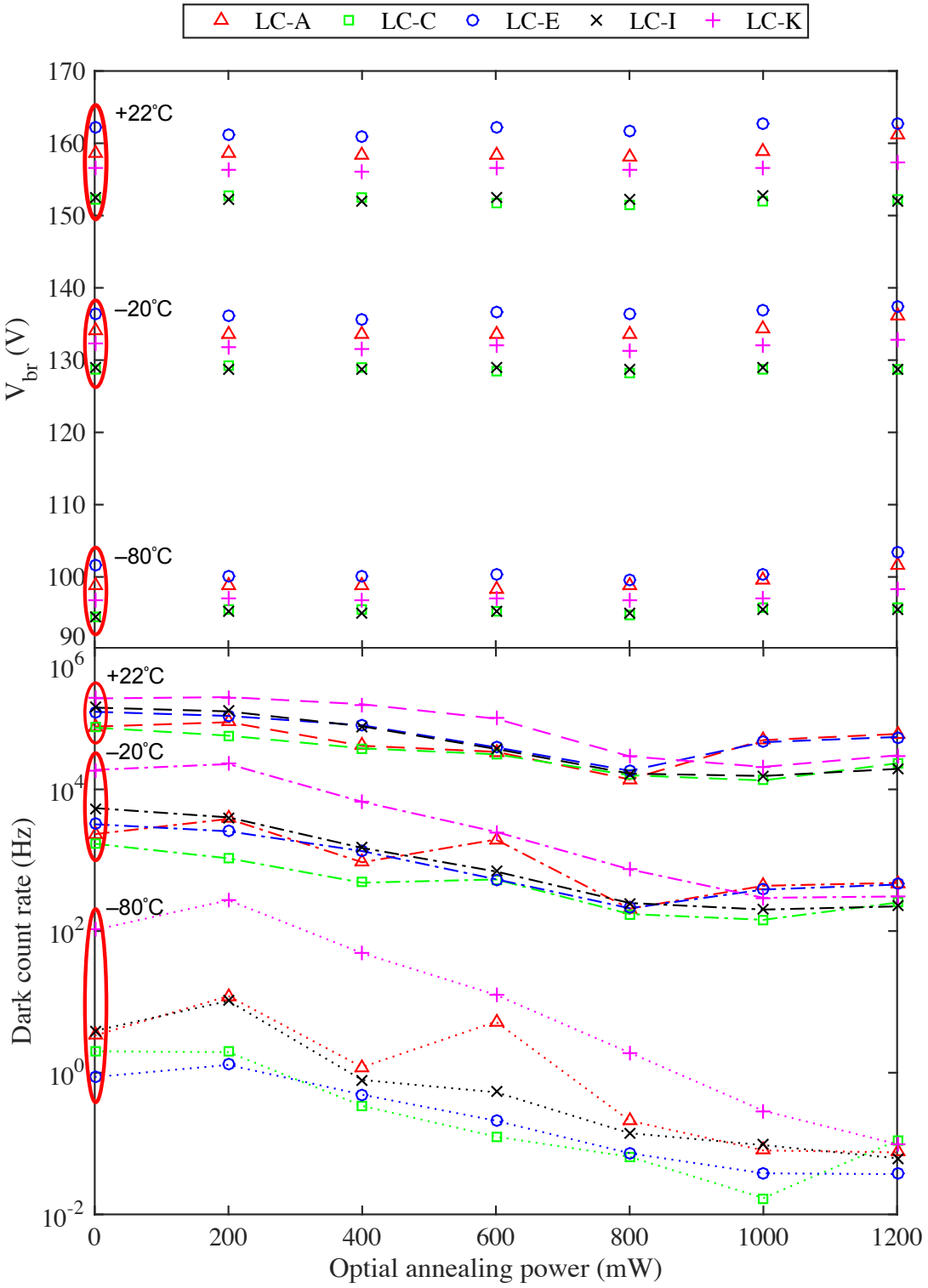

Figure 8.1: **Breakdown voltage (V_{br}) and dark count rate measurement after each 60 s laser annealing cycle as a function of the optical power.** V_{br} is measured at the beginning of every characterization after laser annealing. Data at 0 mW are measurements after proton irradiation.

Table 8.2: **Characteristics of SAP300s tested for 60 s continuous laser annealing.**

Module Identifier		**22 °C**	**−20 °C**	**−80 °C**
LC-A	Pre-radiation DCR (Hz)	10518	-	-
	Post-radiation DCR (Hz)	79808	2677	3.34
	Lowest DCR after laser annealing(Hz)	13832	206.7	0.075
	Corresponding optical power (mW)	800	800	1200
LC-C	Pre-radiation DCR (Hz)	15243	-	-
	Post-radiation DCR (Hz)	84170	2159	2.01
	Lowest DCR after laser annealing(Hz)	12630	144.1	0.017
	Corresponding optical power (mW)	1000	1000	1000
LC-E	Pre-radiation DCR (Hz)	14612	-	-
	Post-radiation DCR (Hz)	119525	3854	0.87
	Lowest DCR after laser annealing(Hz)	18326	209.9	0.037
	Corresponding optical power (mW)	800	800	1200
LC-I	Pre-radiation DCR (Hz)	13632	-	-

	Post-radiation DCR (Hz)	130997	6149	3.9
	Lowest DCR after laser annealing(Hz)	15466	201	0.062
	Corresponding optical power (mW)	1000	1000	1200
LC-K	Pre-radiation DCR (Hz)	15107	-	-
	Post-radiation DCR (Hz)	96935	20249	103.8
	Lowest DCR after laser annealing(Hz)	20768	294.3	0.098
	Corresponding optical power (mW)	1000	1000	1200

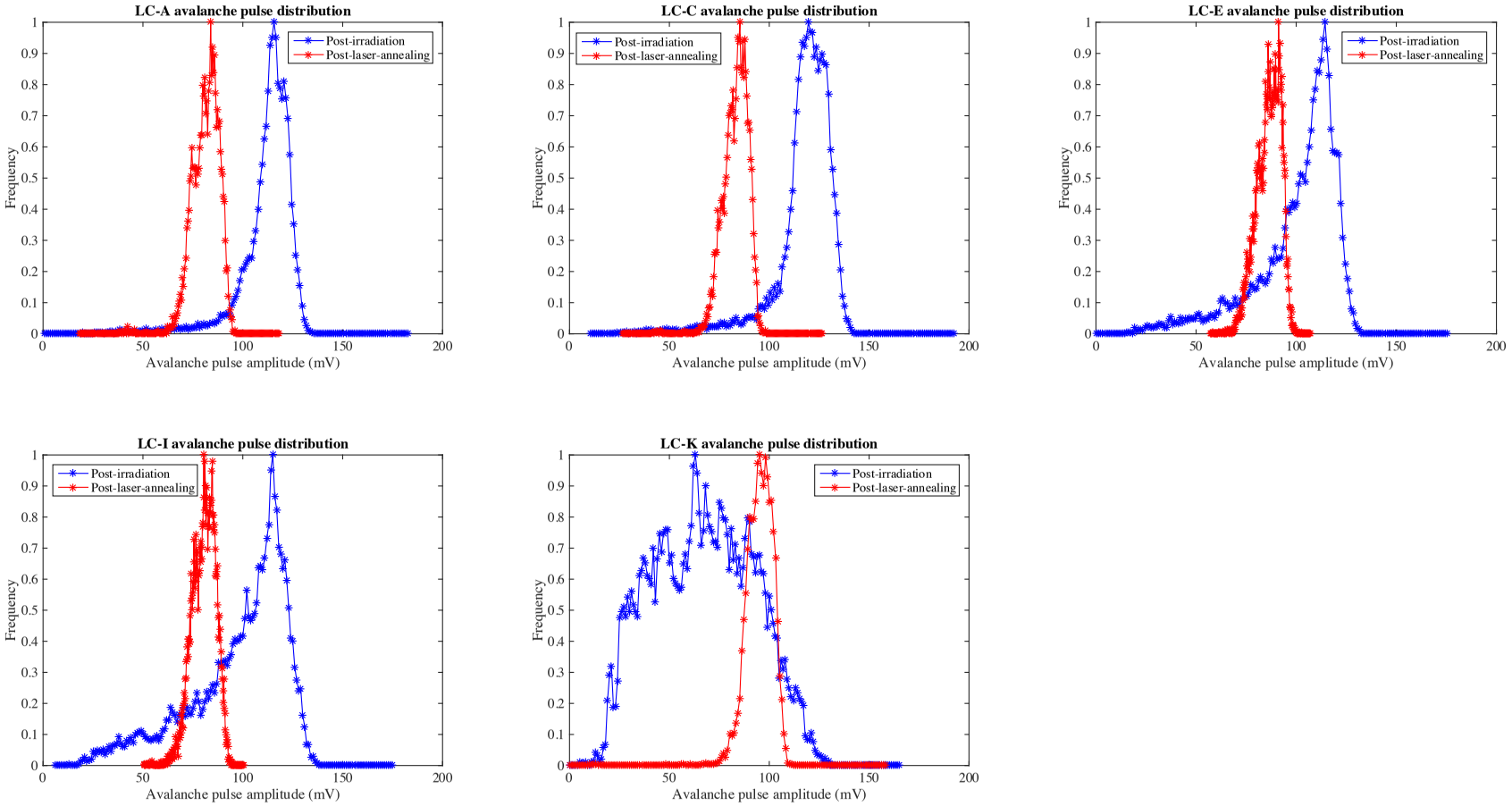

Figure 8.2: **Pulse distribution before (blue) and after (red) laser annealing at 22 °C.** This plot is similar to Fig. 5.9 but the differences are the following. Narrow distribution widths for the red curves here are achieved after laser annealing, instead of cooling the detectors down ot −20 °C. These indicate that the detectors are no longer saturated and that the reduced dark count rates are real. Another difference is that the red curves are shifted to the left relative to the blue curves. This effect occurred because for laser annealing experiment, I used a smaller triggering voltage level for the breakdown voltage measurement, so all detectors' bias voltages are 1−2 V lower than those used at TRIUMF.

8.6 Exploring different laser annealing methods

Two additional laser annealing methods are compared to the initial 60 s continuous laser annealing method. One is 180 s continuous laser annealing, and the other is 50% duty cycle pulses for 60 s. The 180 s laser annealing method should reach similar peak temperatures as the initial method because it was reached in the last few seconds of 60 s, as mentioned in Section 7.6. Thus, if the dark count rate reduction is due to the thermal effect, it may have a similar dark count rate reduction as 60 s laser annealing method. If electrons play an important role, the dark count rate may possibly be reduced further. The purpose of 50% duty cycle method is the opposite of 180 s method. The objective is to maintain the same peak temperature, while only 50% of photons are absorbed to limit electron excitation. The optical chopper's frequency of 1.5 kHz is the fastest frequency I could get, but it is necessary to get modulation frequency >1 MHz such than heat dissipation is slower than laser exposure on the sample.

Figure 8.3 shows V_{br} and dark count rate measurements. All three samples' dark count rates are recovered close to their pre-radiation levels. For characterizations at 22 °C and −20 °C, the maximum dark count rate reduction occurs at the same optical power (800 mW) for 60 s and 180 s laser annealing methods. This result seems to indicate that the laser annealing effect is due to local thermal annealing. However, the 180 s laser annealing method has a higher dark count rate reduction from 267 mW to 800 mW which implies that there could be other effects. If a high-power laser cannot be equipped on a satellite, 180 s laser annealing at an optical power between 267 mW and 800 mW would be better than the initial 60 s laser annealing.

For 50% duty cycle method, the lowest dark count rate is recovered at 2000 mW. This may mean that electrons actually play a role in dark count rate reduction but this power is equivalent to average power of 1000 mW. The optimal average power for the highest dark count rate reduction is the same as that of 60 s laser annealing method. The same peak temperature may have been reached at 2000 mW because it became foggy after 2400 mW exposure. (Both samples for 60 s and 180 s laser annealing methods became foggy after 1200 mW.) Therefore, it is necessary to measure the temperature of the photodiode chips for better analysis for finding the causes of the laser annealing effect. Regardless of the causes of the laser annealing effect, the duty cycle method is not a suitable method in space because it requires much higher optical power.

Table 8.3 summarizes the best dark count rate reduction occurrences. Once again, Fig. 8.4 proves that the dark count rates are indeed recovered because the pulse shapes show that the dark count rates are not saturated anymore.

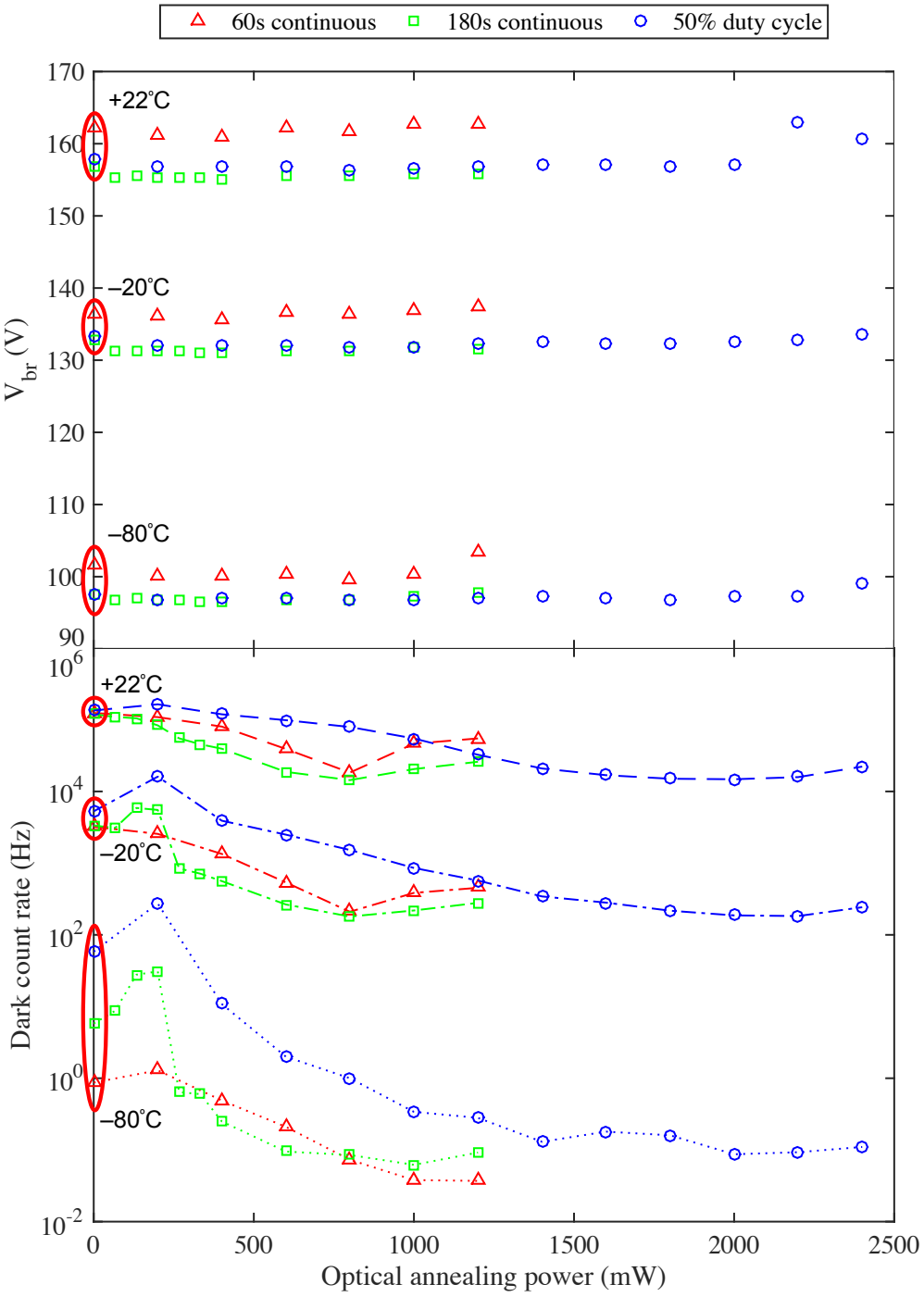

Figure 8.3: **Breakdown voltage ($V_{\mathbf{br}}$) and dark count rate measurement after each optical power for different laser annealing methods comparison.** V_{br} is measured at the beginning of every characterization after laser annealing. Data at 0 mW are measurements after proton irradiation. 60 s laser annealing data are from LC-E, 180 s laser annealing data from LC-G, and 50% duty cycle method data from LC-H.

Table 8.3: **Characteristics of SAP300s tested comparing different laser annealing methods.**

Module Identifier		**22 °C**	**−20 °C**	**−80 °C**
60 s continuous laser annealing (LC-E)	Pre-radiation DCR (Hz)	14612	-	-
	Post-radiation DCR (Hz)	119525	3854	0.87
	Lowest DCR after laser annealing(Hz)	18326	209.9	0.037
	Corresponding optical power (mW)	800	800	1200
180 s continuous laser annealing (LC-G)	Pre-radiation DCR (Hz)	15617	-	-
	Post-radiation DCR (Hz)	109819	3356.7	5.8
	Lowest DCR after laser annealing(Hz)	14388.9	180	0.062
	Corresponding optical power (mW)	800	800	1000
50% duty cycle laser annealing method (LC-H)	Pre-radiation DCR (Hz)	16262	-	-
	Post-radiation DCR (Hz)	103143	5284.5	58.3
	Lowest DCR after laser annealing(Hz)	14796.2	182.9	0.087
	Corresponding optical power (mW)	2000	2200	2000

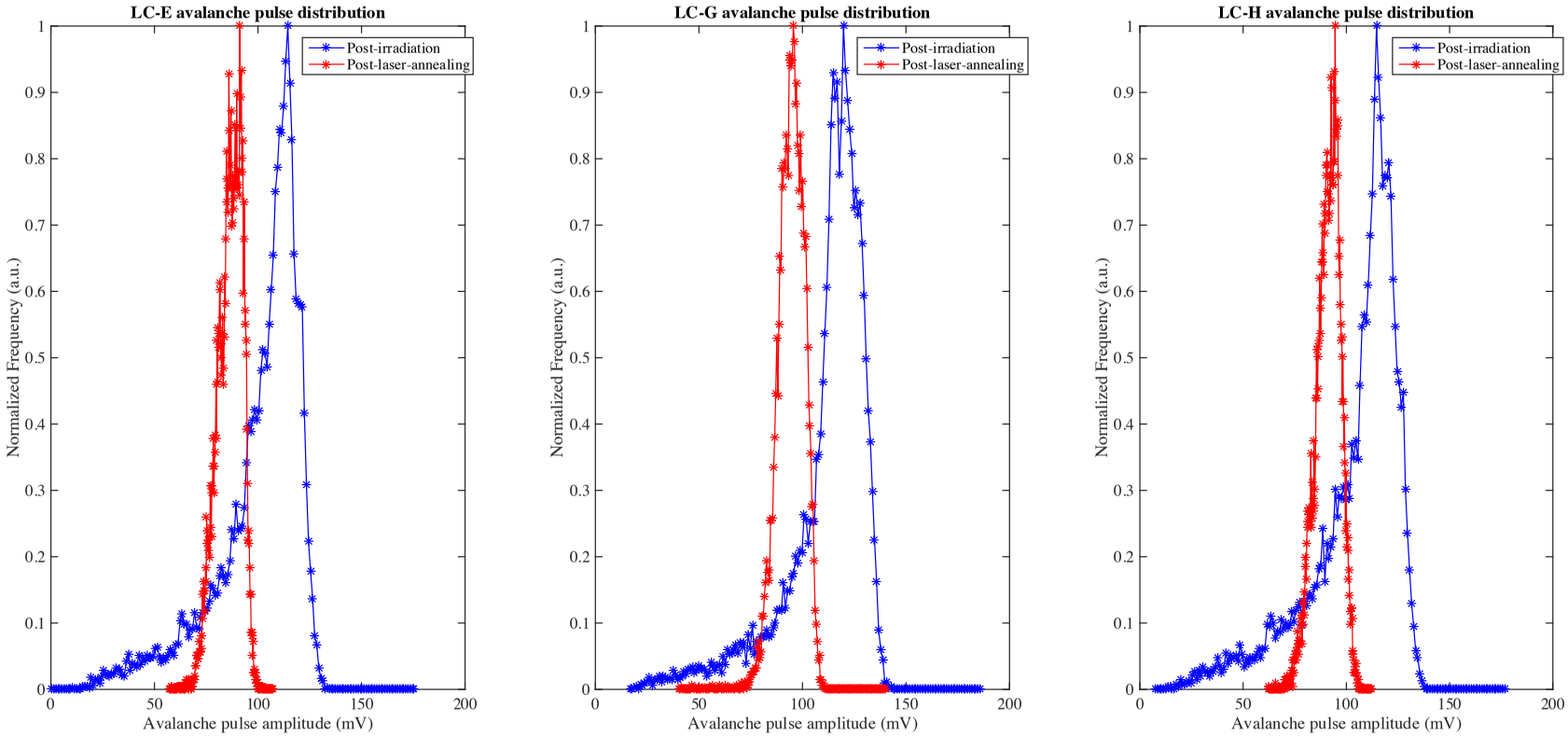

Figure 8.4: **Pulse distribution before and after laser annealing at 22 °C for three different methods.** 60 s laser annealing method: LC-E, 180 s laser annealing method: LC-G, 50% duty cycle method: LC-H. Results are the same as Fig. 8.2. Narrow distribution widths for the red curves here are achieved after laser annealing, instead of cooling the detectors down ot −20 °C. These indicate that the detectors are no longer saturated and that the reduced dark count rates are real. The red curves are shifted to the left relative to the blue curves. This effect occurred because for laser annealing experiment, I used a smaller triggering voltage level for the breakdown voltage measurement, so all detectors' bias voltages are 1−2 V lower than those used at TRIUMF.

50% duty cycle method showed higher dark count rate reduction factor than 180 s method. Thus, LC-B and LC-D are laser-annealed with 50% duty cycle method and the results are compared to those of LC-A and LC-C. Based on the results of LC-H, LC-B and LC-D are only laser-annealed at 1600 mW, 2000 mW, and 2400 mW, where the highest dark count reduction occurred previously. Figure 8.5 shows characterization results. Similar to LC-H, the dark count rates of LC-B and LC-D are the lowest when the average optical power is 800 mW or 1000 mW. All of them were not saturated after proton irradiation, so the dark count rate reduction is real.

Exploring different methods seems to imply that the main cause of laser annealing effect is localized thermal annealing. Thus, in order to verify this hypothesis, LC-F is annealed by forward-biased current only. The results are discussed in the following section.

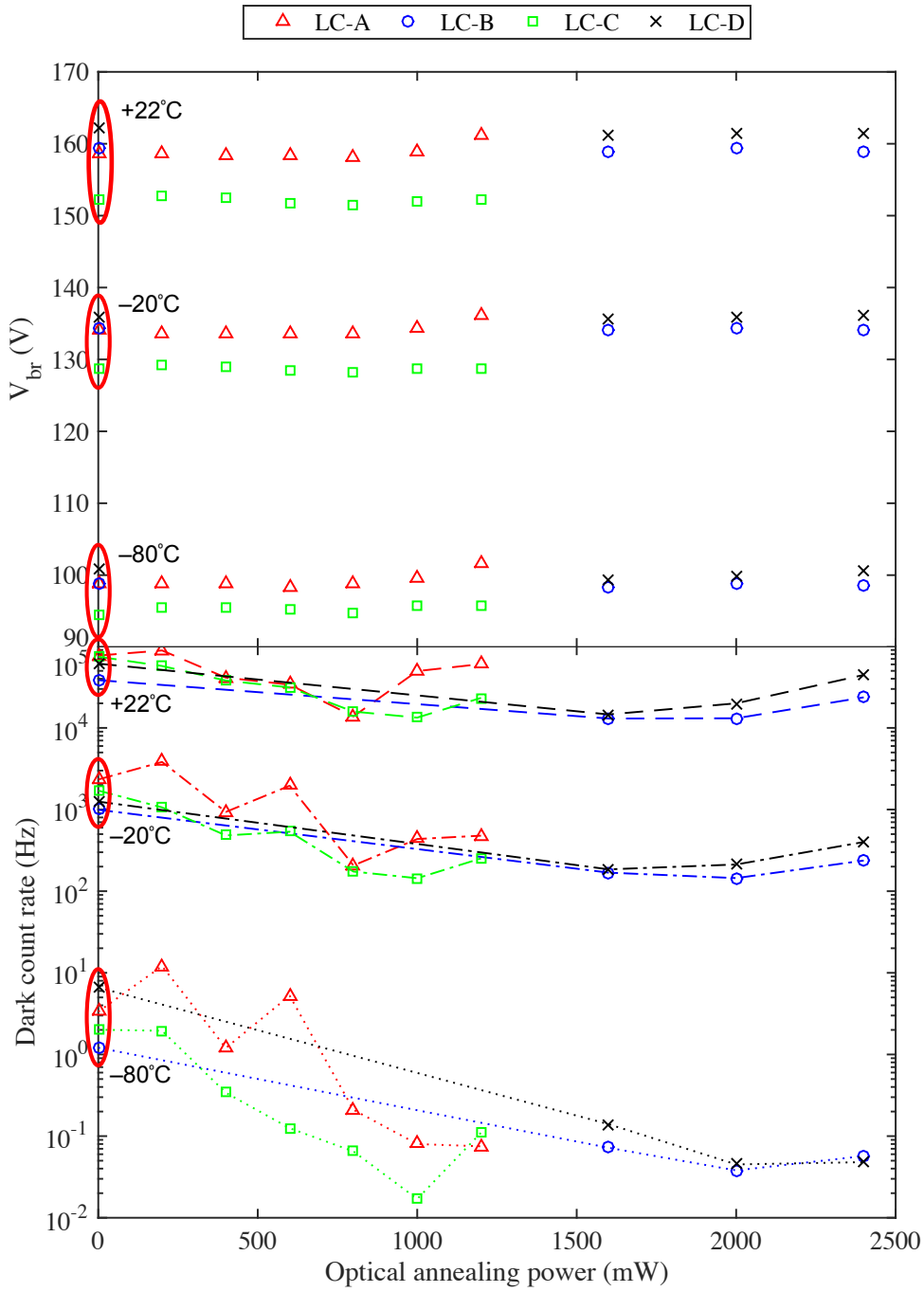

Figure 8.5: **Breakdown voltage (V_{br}) and dark count rate measurement after each optical power for comparing 50% duty cycle method and 60 s laser annealing method.** V_{br} is measured at the beginning of every characterization after laser annealing. Data at 0 mW are measurements after proton irradiation. LC-A and LC-C are laser-annealed by 60 s laser annealing method, while LC-B and LC-D are laser-annealed by 50% duty cycle method. (LC-A, LC-B) and (LC-C, LC-D) pairs have the same proton radiation damage.

8.7 Forward-current annealing

LC-F is annealed for 1 hour at each forward-bias current. A current source is directly connected to the sample and an ammeter and a voltmeter are also connected.

Figure 8.6 shows that the V_{br} remains constant after annealing at different powers and that the dark count rate gradually decreases. After 135 mW was consumed at the diode for an hour, the dark count rate is halved compared to the reference post-irradiation value at 0 mW. (The forward-bias current stopped flowing during annealing at 180 mW.) This dark count rate reduction is interesting because it implies that electrons may play a role in the laser annealing effect.

Figure 8.7 compares the dark count rate of LC-E, LC-F, LC-G, and LC-H that were damaged by the same displacement damage dose. It shows that forward-bias current has steeper dark count rate reduction before it stopped working, although laser annealing of three different methods can reach much lower dark count rates. It is feasible that LC-F is thermally annealed at this power, so thermal images of it are taken shortly after forward-bias current annealing began and shortly before it ended for 147 mW. Figure 8.8 shows that the aluminum package is heated up to ≈33 °C, but when Single-Photon Avalanche photoDiode (SPAD) temperature plot in Fig. 7.3 is extrapolated to ≈33 °C, the corresponding laser power should be somewhere in the range between 250−300 mW. Given this, the forward-bias current annealing method shows better dark count rate reduction that laser annealing at those optical powers, which implies that an electric current also significantly contributes to the dark count rate reduction. However, it is also feasible that the thermal resistance between the photodiode chip and the aluminum package is high such that the temperature of the photodiode chip is much higher and that the thermal annealing effect could be the dominant factor. However, I think the thermal resistance is negligible as the device is very small.

For the next rounds of experiments, it would be interesting to compare the radiation damage mitigation of thermal annealing and forward-bias current annealing to observe which method performs better. While running forward-bias current annealing, the samples should be stored in a cold temperature chamber to exclude any thermal annealing effects.

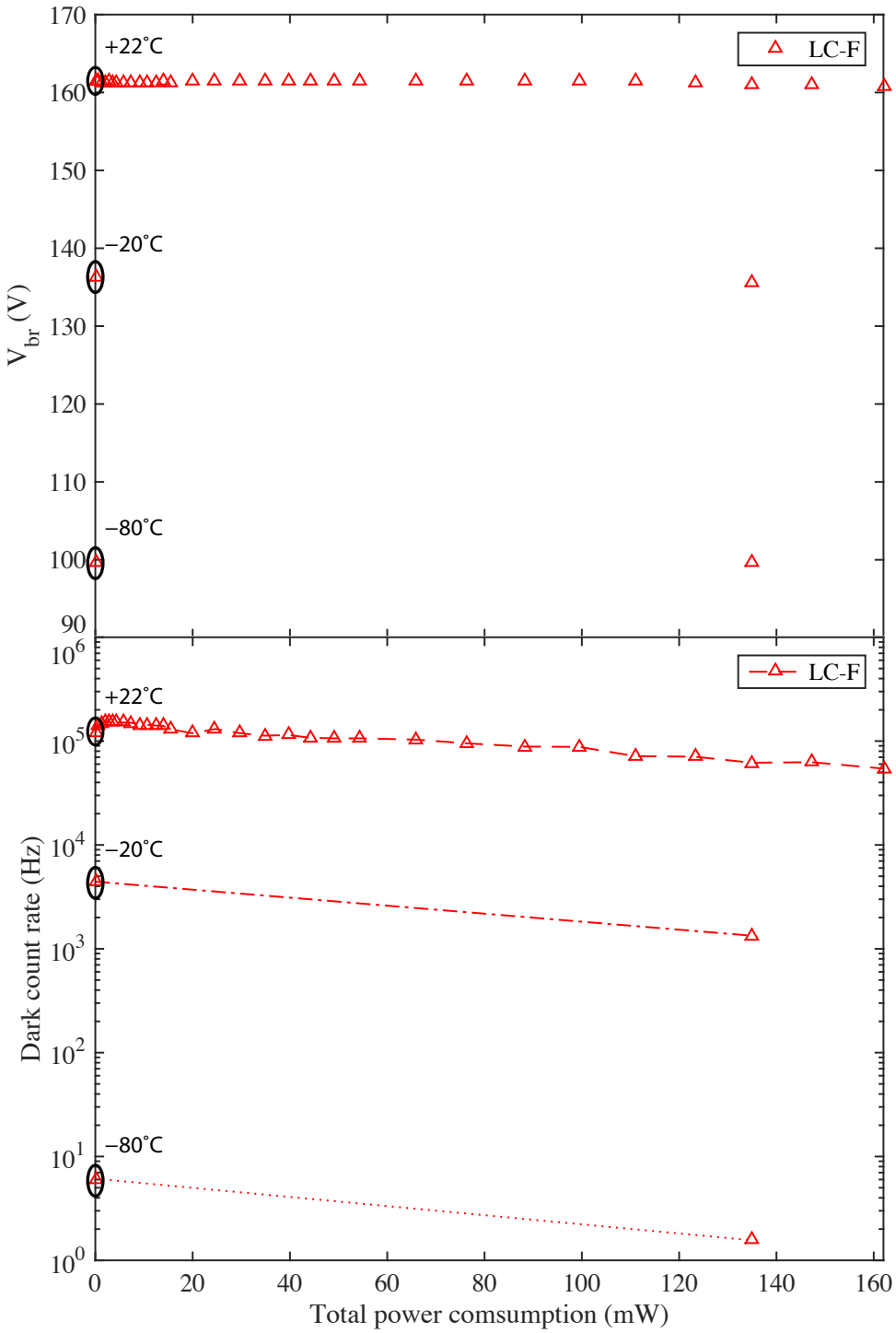

Figure 8.6: **Breakdown voltage ($V_{\mathbf{br}}$) and dark count rate measurement after each forward current annealing.** The forward current was controlled in this measurement, and total power consumption at each forward current is calculated and used as x-axis.

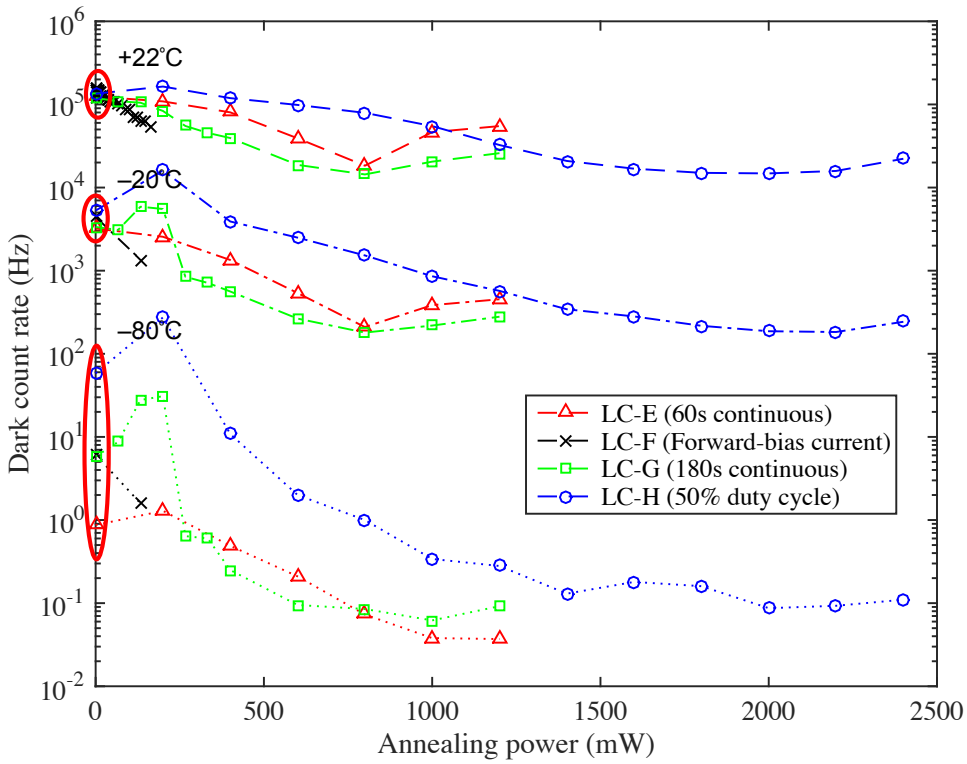

Figure 8.7: **Dark count rate measurement comparison of all different methods.** LC-E, LC-G, and LC-H are annealed by a high-power laser, while LC-F is annealed electrically. LC-F is annealed for 1 hour and LC-H is illuminated by the high-power laser for 60 s.

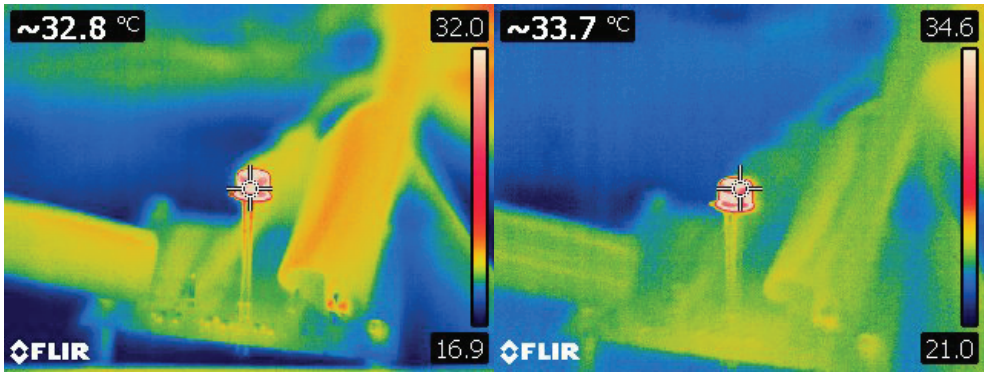

(a) A few minutes after annealing began. (b) After 1 hour

Figure 8.8: **Thermal images of LC-F during forward-bias current annealing at 147 mW.** Images of the photodiode chip could not be taken because a glass window in front blocks light for imaging. As a result, photos are taken from the side. (FLIR E60 is used for the images.)

8.8 Permanence testing

It is investigated whether the laser annealing is effective on samples with low proton radiation damage and whether the effect is permanent when stored under 3 different conditions: LC-M at room temperature with bias off, LC-N at room temperature with reverse-bias on, and LC-O at $-20\,^{\circ}\mathrm{C}$ with bias off. After each laser annealing exposure, the samples are stored in their conditions for next 58-59 hours. For the first six hours, the samples are characterized every two hours, then twice per day for the rest with the storage interval varying between 8-13 hours.

LC-M and LC-O, respectively, have 1000 Hz and 2000 Hz dark count rates increase after proton irradiation. Their dark count rates are minuscule so their states should be similar to those of to non-irradiated samples, so we expected these samples to also experience dark count rate reduction in $400-800\,\mathrm{mW}$ range, as shown in [110]. However, they both have no significant changes $<1\,\mathrm{W}$. On the other hand, LC-N has higher proton radiation damage and it shows a similar behaviour as the one in [110]. The dark count rate increases after 200 mW, and then it is 1.6 times lower than the reference dark count rate after 600 mW. These results lead to a conclusion that laser annealing should be performed when the dark count rate is significantly increased. Fluctuations in the dark count rates during permanence test are mainly caused by the operating temperature fluctuation.

For LC-N and LC-O, V_{br} increases after 1.2 W laser annealing. In [111], it was shown that when V_{br} begins to increase, the SAP500s stopped working if laser-annealed at $1400-1600\,\mathrm{mW}$ optical power. SAP300s are manufactured from the same company and these samples also became foggy when V_{br} increased. All samples from NUS became foggy after 1.2 W exposure, shown in Fig. 8.10, so we stopped laser annealing at 1.2 W. The mean pulse amplitude remains fairly constant for the most of the time. Laser annealing effect appears to be permanent when stored in any of three different conditions.

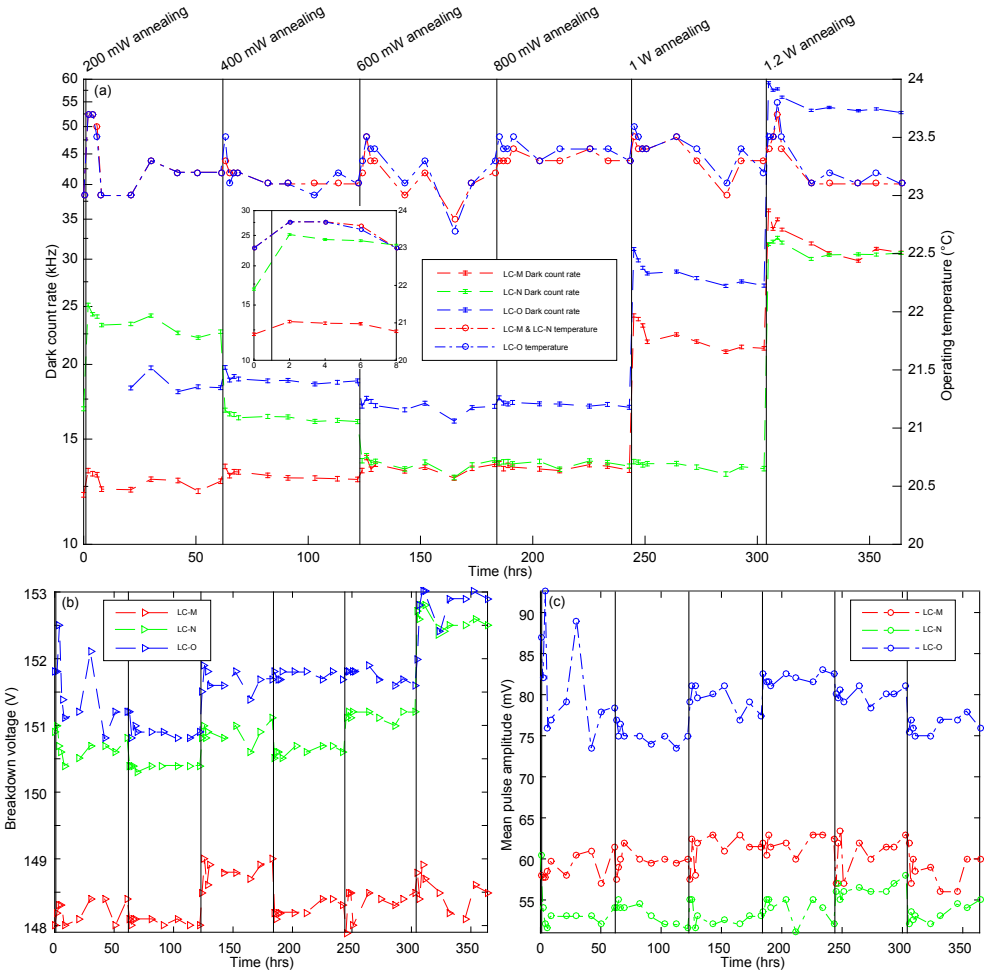

Figure 8.9: **LC-M, LC-N, LC-O characterization results.** The errorbars for the dark count rate represent one standard deviation of the value following Poissonian distribution. Inset of the dark count rate is data points for first 8 hours. For dark count rate measurement, a time-tagging unit (UQDevices 16-channel) was planned to be used, but it could not pick up the small avalanche pulses of LC-M and LC-N, so a counting device to Stanford Research Systems SR 400 two channel gated photon counter, operating at 10 MHz with threshold value at 40 mV, was used instead for these samples. The overvoltage of LC-O is higher than the other, so we could collect counts using the time-tagging unit, so we proceeded to use it just for LC-O. However, after 200 mW annealing and six hours into permanence test, we noticed that the time-tagging unit's discriminator functions poorly, causing the count rate to fluctuate. From this point, we used SR 400 even for LC-O. This is why Figure 8.9 is missing first few dark count rate data points for LC-O. Characterization results of LC-M, LC-N, and LC-O after proton irradiation are provided in Table 5.6.

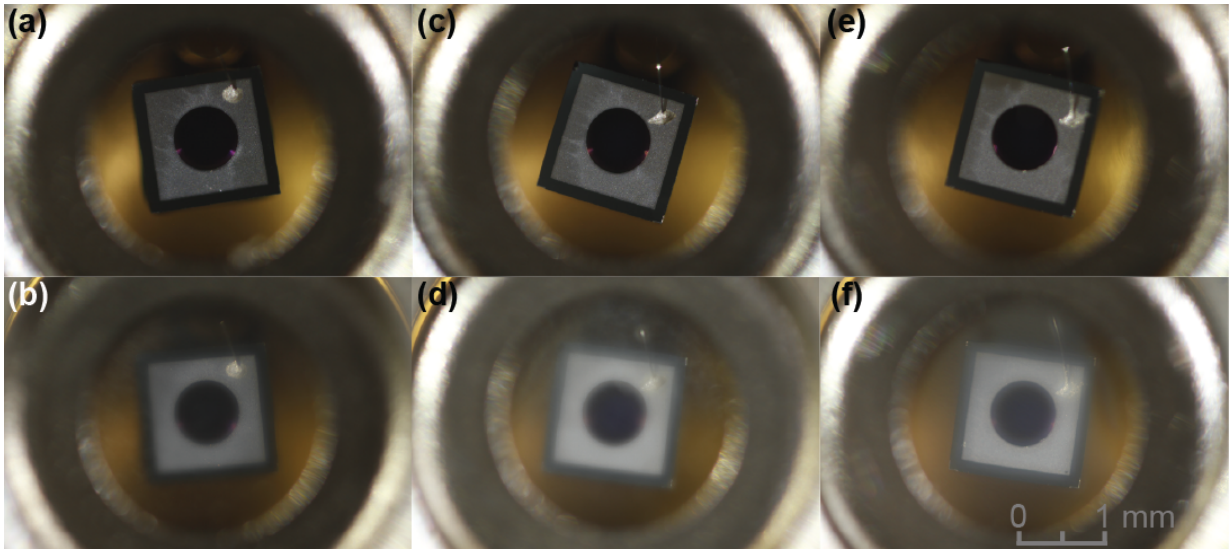

Figure 8.10: **Pictures of LC-M, LC-N, LC-O.** (a) LC-M prior to laser annealing, (b) LC-M after 1.2 W, (c) LC-N prior to laser annealing, (d) LC-N after 1.2 W, (e) LC-O prior to laser annealing, (f) LC-O after 1.2 W.

8.9 Conclusion

The second round of laser annealing of irradiated SAP300s showed that the dark count rate can be recovered to the level close to the pre-radiation values. This is the first full cycle of radiation tests and laser annealing for directly comparing the dark count rates of pre-radiation, post-radiation, and post-laser-annealing. For operations at between $-20\,^{\circ}\mathrm{C}$ and $22\,^{\circ}\mathrm{C}$, the best laser power is $800-1000\,\mathrm{mW}$ and SAP300s should be laser annealed before the accumulative radiation damage is below 4×10^9 proton fluences @ 100 MeV proton energy. For operations at $-80\,^{\circ}\mathrm{C}$, SAP300s can be laser-annealed any time using the optical power at 1200 mW. For new annealing methods in space, the forward-bias current annealing and 180 s continuous laser annealing method could be considered. From our tests with different approaches - forward-bias current annealing, 180 s continuous laser annealing, and 50% duty cycle method - it appears that electrons may play a role in reducing the dark count rate but more testing will be required for finding the exact causes of laser annealing effect. Finally, our observations indicate that the laser annealing improvement seems to be permanent.

Chapter 9

Conclusions and Outlook

In this Thesis, I presented the results of four projects I participated in. In Chapter 5, I calculated radiation dose for ISS orbit and performed proton radiation test on Laser Components SAP300s. We found that the dark count rate increase and proton fluences have a linear relationship and that after staying at the simulated ISS orbit for more than 6 months, SAP300s are all saturated at room temperature.

In Chapter 6, I estimated the radiation dose inside an ISS pressure vessel to study the feasibility of using silicon Single-Photon Avalanche photoDiode (SPAD)s for Space-QUEST experiment for 1-year mission time. We showed that Excelitas SLiK, Excelitas C30902SH, and Laser Components SAP500 should be able to be cooled down to $-45\,^{\circ}\mathrm{C}$, $-65\,^{\circ}\mathrm{C}$, and $-75\,^{\circ}\mathrm{C}$, respectively, to reach the dark count rate of 2000 Hz.

In Chapter 7, research in laser annealing of irradiated silicon SPADs was performed. Our results demonstrated that high-power continuous-wave laser annealing for 60 s can remedy simulated low-Earth-orbit radiation damage for three different types of SPADs: Excelitas SLiK, Excelitas C30902SH, and Laser Components SAP500. The dark count rate of all samples, including the samples that were previously thermally annealed, is greatly reduced. Several of them have their dark count rates recovered to typical pre-radiation levels.

In Chapter 8, research in laser annealing of irradiated SAP300s was performed. Having the pre-radiation characterization results, unlike the previous project, we could show that the dark count rate is indeed recovered to the pre-radiation level after laser annealing. We also explored additional annealing methods and showed that laser annealing for 180 s and forward-bias current annealing can be investigated further for use in space if it is not possible to equip a satellite with a high-power laser ($\geq$1 W). We also showed that laser

annealing is a permanent effect. However, more tests need to be performed to find the exact causes of the laser annealing effect.

Thermal annealing had been performed on silicon SPADs before [66, 69, 70, 100] to counteract the radiation damage. As far as we know, it is the first time to perform high-power laser annealing on silicon SPADs for quantum communications to reduce the background noise, produced by radiation damage. Either method can lengthen the lifespan of a quantum satellite. However, there are still two limitations in our laser annealing research. One is that the radiation dose calculation using SPENVIS has a factor of $2-3$ error when compared to real space radiation environment [105]. The other is the statistical fluctuations between samples. Only one or two samples with the same radiation dose were tested and shown in this thesis. Thus, more samples with the same radiation dose need to be tested for statistical variations research. To resolve the first limitation, the University of Illinois, Urbana-Champagne, the University of Waterloo, and NASA are working together to launch a cube satellite to test both thermal annealing and laser annealing on silicon SPADs in low Earth orbit [91]. This project will verify whether laser annealing is indeed more effective at mitigating radiation damage in space and whether it can be practical over thermal annealing using a built-in thermoelectric cooler. If this project concludes that laser annealing is a better method to implement for future quantum satellites, more samples can then be tested to resolve the statistical variation limitation. Furthermore, the project can quantify the lifespan of the satellite when radiation damage mitigation methods are implemented. In the meantime, studies on the laser annealing effect mechanisms can be investigated further.

References

[1] G. E. Moore. Cramming more components onto integrated circuits, Reprinted from Electronics, volume 38, number 8, April 19, 1965, pp.114 ff. *IEEE Solid-State Circuits Society Newsletter*, 11(5):33–35, 2006.

[2] Denis Mamaluy and Xujiao Gao. The fundamental downscaling limit of field effect transistors. *Applied Phys. Lett.*, 106(19):193503, 2015.

[3] Richard Feynman. Simulating physics with computers. *Int'l J. Theor. Phys.*, 21:467–488, 1982.

[4] Peter W. Shor. Polynomial-time algorithms for prime factorization and discrete logarithms on a quantum computer. *SIAM J. Comput.*, 26(5):1484–1509, 1997.

[5] R. L. Rivest, A. Shamir, and L. Adleman. A method for obtaining digital signatures and public-key cryptosystems. *Commun. ACM*, 21(2):120–126, 1978.

[6] W. Diffie and M. Hellman. New directions in cryptography. *IEEE Trans. Inf. Theor.*, 22(6):644–654, 2006.

[7] Victor S. Miller. *Use of Elliptic Curves in Cryptography*, pages 417–426. Springer Berlin Heidelberg, 1986.

[8] Neal Koblitz. Elliptic curve cryptosystems. *Mathematics of Computation*, 48(177):203–209, 1987.

[9] Lov K. Grover. A fast quantum mechanical algorithm for database search. arXiv:quant-ph/9605043.

[10] Joan Daemen and Vincent Rijmen. AES Proposal: Rijndael, 1999.

[11] Michele Mosca. Cybersecurity in an era with quantum computers: will we be ready? Cryptology ePrint Archive, Report 2015/1075, 2015. http://eprint.iacr.org/2015/1075.

[12] C. H. Bennett and G. Brassard. Quantum cryptography: Public key distribution and coin tossing. In *Proceedings of the IEEE International Conference on Computers, Systems, and Signal Processing*, pages 175–179, Bangalore, India, December 1984.

[13] A. K. Ekert. Quantum Cryptography Based on Bell's Theorem. *Phys. Rev. Lett.*, 67(6):661–663, 1991.

[14] Oded Regev. On lattices, learning with errors, random linear codes, and cryptography. In *Proceedings of the Thirty-seventh Annual ACM Symposium on Theory of Computing*, STOC '05, pages 84–93. ACM, 2005.

[15] Jacques Kipnis, Aviadand Patarin and Louis Goubin. *Unbalanced Oil and Vinegar Signature Schemes*, pages 206–222. Springer Berlin Heidelberg, 1999.

[16] Jintai Ding and Dieter Schmidt. *Rainbow, a New Multivariable Polynomial Signature Scheme*, pages 164–175. Springer Berlin Heidelberg, 2005.

[17] David Jao and Luca De Feo. *Towards Quantum-Resistant Cryptosystems from Supersingular Elliptic Curve Isogenies*, pages 19–34. Springer Berlin Heidelberg, 2011.

[18] Simon Singh. *The Code Book: The Evolution of Secrecy from Mary, Queen of Scots, to Quantum Cryptography*. Doubleday, New York, NY, USA, 1st edition, 1999.

[19] W. K. Wootters and W. H. Zurek. A single quantum cannot be cloned. *Nature*, 299:802, 1982.

[20] W. Heisenberg. Über den anschaulichen inhalt der quantentheoretischen kinematik und mechanik. *Zeitschrift für Physik*, 43(3):172–198, Mar 1927.

[21] C. E. Shannon. Communication theory of secrecy systems. *Bell Syst. Tech. J*, 28(4):656–715, 1949.

[22] P. D. Townsend, J. G. Rarity, and P. R. Tapster. Enhanced single photon fringe visibility in a 10 km-long prototype quantum cryptography channel. *Electron. Lett.*, 29(14):1291–1293, July 1993.

[23] J. Breguet, A. Muller, and N. Gisin. Quantum cryptography with polarized photons in optical fibres. *J. Mod. Opt.*, 41(12):2405–2412, 1994.

[24] J.D. Franson and H. Ilves. Quantum cryptography using polarization feedback. *J. Mod. Opt.*, 41(12):2391–2396, 1994.

[25] W. T. Buttler, R. J. Hughes, P. G. Kwiat, S. K. Lamoreaux, G. G. Luther, G. L. Morgan, J. E. Nordholt, C. G. Peterson, and C. M. Simmons. Practical free-space quantum key distribution over 1 km. *Phys. Rev. Lett.*, 81:3283, 1998.

[26] Richard J. Hughes, William T. Buttler, Paul G. Kwiat, Steve K. Lamoreaux, Gabriel G. Luther, George L. Morgan, Jane E. Nordholt, and C. Glen Peterson. Quantum cryptography for secure free-space communications. In *Proc. SPIE*, volume 3615, pages 3615–3616, 1999.

[27] H.-J. Briegel, W. Dür, J. I. Cirac, and P. Zoller. Quantum repeaters: the role of imperfect local operations in quantum communication. *Phys. Rev. Lett.*, 81(26):5932–5935, 1998.

[28] M. Peev, C. Pacher, R. Alléaume, C. Barreiro, J. Bouda, W. Boxleitner, T. Debuisschert, E. Diamanti, M. Dianati, J. F. Dynes, S. Fasel, S. Fossier, M. Fürst, J.-D. Gautier, O. Gay, N. Gisin, P. Grangier, A. Happe, Y. Hasani, M. Hentschel, H. Hübel, G. Humer, T. Länger, M. Legré, R. Lieger, J. Lodewyck, T. Lorünser, N Lütkenhaus, A. Marhold, T. Matyus, O. Maurhart, L. Monat, S. Nauerth, J.-B. Page, A. Poppe, E. Querasser, G. Ribordy, S. Robyr, L. Salvail, A. W. Sharpe, A. J. Shields, D. Stucki, M. Suda, C. Tamas, T. Themel, R. T. Thew, Y. Thoma, A. Treiber, P. Trinkler, R. Tualle-Brouri, F. Vannel, N. Walenta, H. Weier, H. Weinfurter, I. Wimberger, Z. L. Yuan, H. Zbinden, and A. Zeilinger. The SECOQC quantum key distribution network in Vienna. *New J. Phys.*, 11(7):075001, 2009.

[29] Qiang Zhang. Recent progress of quantum key distribution in china. 2014. (presented at Qcrypt 2014, Paris, France).

[30] Sung hyun Lim. SK Telecom develops long-range quantum communication technology. *Pulse*, 2017.

[31] M. Sasaki, M. Fujiwara, H. Ishizuka, W. Klaus, K. Wakui, M. Takeoka, S. Miki, T. Yamashita, Z. Wang, A. Tanaka, K. Yoshino, Y. Nambu, S. Takahashi, A. Tajima, A. Tomita, T. Domeki, T. Hasegawa, Y. Sakai, H. Kobayashi, T. Asai, K. Shimizu, T. Tokura, T. Tsurumaru, M. Matsui, T. Honjo, K. Tamaki, H. Takesue, Y. Tokura, J. F. Dynes, A. R. Dixon, A. W. Sharpe, Z. L. Yuan, A. J. Shields, S. Uchikoga, M. Legré, S. Robyr, P. Trinkler, L. Monat, J.-B. Page, G. Ribordy, A. Poppe, A. Allacher, O. Maurhart, T. Länger, M. Peev, and A. Zeilinger. Field test of quantum key distribution in the Tokyo QKD Network. *Opt. Express*, 19(11):10387–10409, May 2011.

[32] Matin Durrani. UK splashes out 270m on quantum technology. *Physics World*, 2014.

[33] D. Stucki, M. Legré, F. Buntschu, B. Clausen, N. Felber, N. Gisin, L. Henzen, P. Junod, G. Litzistorf, P. Monbaron, L. Monat, J.-B. Page, D. Perroud, G. Ribordy, A. Rochas, S. Robyr, J. Tavares, R. Thew, P. Trinkler, S. Ventura, R. Voirol, N. Walenta, and H. Zbinden. Long-term performance of the SwissQuantum quantum key distribution network in a field environment. *New J. Physics*, 13(12):123001, 2011.

[34] Chip Elliott. The DARPA Quantum Network. arXiv:quant-ph/0412029.

[35] Richard J. Hughes, Jane E. Nordholt, Kevin P. McCabe, Raymond T. Newell, Charles G. Peterson, and Rolando D. Somma. Network-centric quantum communications with application to critical infrastructure protection. arXiv:1305.0305.

[36] Don Hayford. Quantum-based Product Development at Battelle. 2014. (presented at Qcrypt 2014, Paris, France).

[37] J. E. Nordholt, Richard J. Hughes, George L. Morgan, C. Glen Peterson, and Christopher C. Wipf. Present and future free-space quantum key distribution. In *Proc. of SPIE on Free-Space Laser Communication Technologies*, volume 4635, pages 116–126, 2002.

[38] J. G. Rarity, P. R. Tapster, P. M. Gorman, and P. Knight. Ground to satellite secure key exchange using quantum cryptography. *New J. Phys.*, 4(1):82, 2002.

[39] M. Aspelmeyer, T. Jennewein, M. Pfennigbauer, W. R. Leeb, and A. Zeilinger. Long-distance quantum communication with entangled photons using satellites. *IEEE J. Sel. Top. Quantum Electronics*, 9(6):1541–1551, 2003.

[40] C. Bonato, A. Tomaello, V. Da Deppo, G. Naletto, and P. Villoresi. Feasibility of satellite quantum key distribution. *New J. Phys.*, 11(4):045017, 2009.

[41] J.-P. Bourgoin, E. Meyer-Scott, B. L. Higgins, B. Helou, C. Erven, H. Hübel, B. Kumar, D. Hudson, I. D'Souza, R. Girard, R. Laflamme, and T. Jennewein. A comprehensive design and performance analysis of low earth orbit satellite quantum communication. *New J. Phys.*, 15:023006, 2013.

[42] T. Schmitt-Manderbach, H. Weier, M. Fürst, R. Ursin, F. Tiefenbacher, T. Scheidl, J. Perdigues, Z. Sodnik, C. Kurtsiefer, J. G. Rarity, A. Zeilinger, and H. Weinfurter. Experimental demonstration of free-space decoy-state quantum key distribution over 144 km. *Phys. Rev. Lett.*, 98(1):010504, 2007.

[43] R. Ursin, F. Tiefenbacher, T. Schmitt-Manderbach, H. Weier, T. Scheidl, M. Lindenthal, B. Blauensteiner, T. Jennewein, J. Perdigues, P. Trojek, B. Ömer, M. Fürst, M. Meyenburg, J. Rarity, Z. Sodnik, C. Barbieri, H. Weinfurter, and A. Zeilinger. Entanglement-based quantum communication over 144 km. *Nat. Phys.*, 3(7):481–486, 2007.

[44] Matthew P Peloso, Ilja Gerhardt, Caleb Ho, Anta Lamas-Linares, and Christian Kurtsiefer. Daylight operation of a free space, entanglement-based quantum key distribution system. *New J. Physics*, 11(4):045007, 2009.

[45] Evan Meyer-Scott, Zhizhong Yan, Allison MacDonald, Jean-Philippe Bourgoin, Hannes Hübel, and Thomas Jennewein. How to implement decoy-state quantum key distribution for a satellite uplink with 50-dB channel loss. *Phys. Rev. A*, 84:062326, Dec 2011.

[46] Juan Yin, Ji-Gang Ren, He Lu, Yuan Cao, Hai-Lin Yong, Yu-Ping Wu, Chang Liu, Sheng-Kai Liao, Fei Zhou, Yan Jiang, Xin-Dong Cai, Ping Xu, Ge-Sheng Pan, Jian-Jun Jia, Yong-Mei Huang, Hao Yin, Jian-Yu Wang, Yu-Ao Chen, Cheng-Zhi Peng, and Jian-Wei Pan. Quantum teleportation and entanglement distribution over 100-kilometre free-space channels. *Nature*, 488(7410):185–188, 2012.

[47] Jean-Philippe Bourgoin, Nikolay Gigov, Brendon L. Higgins, Zhizhong Yan, Evan Meyer-Scott, Amir K. Khandani, Norbert Lütkenhaus, and Thomas Jennewein. Experimental quantum key distribution with simulated ground-to-satellite photon losses and processing limitations. *Phys. Rev. A*, 92:052339, 2015.

[48] Jean-Philippe Bourgoin, Brendon L. Higgins, Nikolay Gigov, Catherine Holloway, Christopher J. Pugh, Sarah Kaiser, Miles Cranmer, and Thomas Jennewein. Free-space quantum key distribution to a moving receiver. *Opt. Express*, 23(26):33437–33447, Dec 2015.

[49] Sheng-Kai Liao, Hai-Lin Yong, Chang Liu, Guo-Liang Shentu, Dong-Dong Li, Jin Lin, Hui Dai, Shuang-Qiang Zhao, Bo Li, Jian-Yu Guan, Wei Chen, Yun-Hong Gong, Yang Li, Ze-Hong Lin, Ge-Sheng Pan, Jason S. Pelc, FejerM. M., Wen-Zhuo Zhang, Wei-Yue Liu, Juan Yin, Ji-Gang Ren, Xiang-Bin Wang, Qiang Zhang, Cheng-Zhi Peng, and Jian-Wei Pan. Long-distance free-space quantum key distribution in daylight towards inter-satellite communication. *Nat. Photonics*, 11(8):509–513, 2017.

[50] Sebastian Nauerth, Florian Moll, Markus Rau, Christian Fuchs, Joachim Horwath,

Stefan Frick, and Harald Weinfurter. Air-to-ground quantum communication. *Nat. Photonics*, 7:382, 2013.

[51] Jian-Yu Wang, Bin Yang, Sheng-Kai Liao, Liang Zhang, Qi Shen, Xiao-Fang Hu, Jin-Cai Wu, Shi-Ji Yang, Hao Jiang, Yan-Lin Tang, Bo Zhong, Hao Liang, Wei-Yue Liu, Yi-Hua Hu, Yong-Mei Huang, Bo Qi, Ji-Gang Ren, Ge-Sheng Pan, Juan Yin, Jian-Jun Jia, Yu-Ao Chen, Kai Chen, Cheng-Zhi Peng, and Jian-Wei Pan. Direct and full-scale experimental verifications towards groundsatellite quantum key distribution. *Nat. Photonics*, 7:387–393, 2013.

[52] Christopher J Pugh, Sarah Kaiser, Jean-Philippe Bourgoin, Jeongwan Jin, Nigar Sultana, Sascha Agne, Elena Anisimova, Vadim Makarov, Eric Choi, Brendon L Higgins, and Thomas Jennewein. Airborne demonstration of a quantum key distribution receiver payload. *Quantum Sci.Technol.*, 2(2):024009, 2017.

[53] Morio Toyoshima, Hideki Takenaka, Yozo Shoji, Yoshihisa Takayama, Yoshisada Koyama, and Hiroo Kunimori. Polarization measurements through space-to-ground atmospheric propagation paths by using a highly polarized laser source in space. *Opt. Express*, 17(25):22333–22340, Dec 2009.

[54] Juan Yin, Yuan Cao, Shu-Bin Liu, Ge-Sheng Pan, Jin-Hong Wang, Tao Yang, Zhong-Ping Zhang, Fu-Min Yang, Yu-Ao Chen, Cheng-Zhi Peng, and Jian-Wei Pan. Experimental quasi-single-photon transmission from satellite to earth. *Opt. Express*, 21(17):20032–20040, Aug 2013.

[55] Giuseppe Vallone, Davide Bacco, Daniele Dequal, Simone Gaiarin, Vincenza Luceri, Giuseppe Bianco, and Paolo Villoresi. Experimental satellite quantum communications. *Phys. Rev. Lett.*, 115:040502, Jul 2015.

[56] Zhongkan Tang, Rakhitha Chandrasekara, Yue Chuan Tan, Cliff Cheng, Luo Sha, Goh Cher Hiang, Daniel K. L. Oi, and Alexander Ling. Generation and analysis of correlated pairs of photons aboard a nanosatellite. *Phys. Rev. Applied*, 5:054022, May 2016.

[57] Daniele Dequal, Giuseppe Vallone, Davide Bacco, Simone Gaiarin, Vincenza Luceri, Giuseppe Bianco, and Paolo Villoresi. Experimental single-photon exchange along a space link of 7000 km. *Phys. Rev. A*, 93:010301, Jan 2016.

[58] Giuseppe Vallone, Daniele Dequal, Marco Tomasin, Francesco Vedovato, Matteo Schiavon, Vincenza Luceri, Giuseppe Bianco, and Paolo Villoresi. Interference at the

single photon level along satellite-ground channels. *Phys. Rev. Lett.*, 116:253601, Jun 2016.

[59] Hideki Takenaka, Alberto Carrasco-Casado, Mikio Fujiwara, Mitsuo Kitamura, Masahide Sasaki, and Morio Toyoshima. Satellite-to-ground quantum-limited communication using a 50-kg-class microsatellite. *Nat. Photonics*, 11:502508, 2017.

[60] Kevin Günthner, Imran Khan, Dominique Elser, Birgit Stiller, Ömer Bayraktar, Christian R. Müller, Karen Saucke, Daniel Tröndle, Frank Heine, Stefan Seel, Peter Greulich, Herwig Zech, Björn Gütlich, Sabine Philipp-May, Christoph Marquardt, and Gerd Leuchs. Quantum-limited measurements of optical signals from a geostationary satellite. *Optica*, 4(6):611–616, Jun 2017.

[61] Sheng-Kai Liao, Wen-Qi Cai, Wei-Yue Liu, Liang Zhang, Yang Li, Ji-Gang Ren, Juan Yin, Qi Shen, Yuan Cao, Zheng-Ping Li, Feng-Zhi Li, Xia-Wei Chen, Li-Hua Sun, Jian-Jun Jia, Jin-Cai Wu, Xiao-Jun Jiang, Jian-Feng Wang, Yong-Mei Huang, Qiang Wang, Yi-Lin Zhou, Lei Deng, Tao Xi, Lu Ma, Tai Hu, Qiang Zhang, Yu-Ao Chen, Nai-Le Liu, Xiang-Bin Wang, Zhen-Cai Zhu, Chao-Yang Lu, Rong Shu, Cheng-Zhi Peng, Jian-Yu Wang, and Jian-Wei Pan. Satellite-to-ground quantum key distribution. *Nature*, 549:43–47, 2017.

[62] Juan Yin, Yuan Cao, Yu-Huai Li, Sheng-Kai Liao, Liang Zhang, Ji-Gang Ren, Wen-Qi Cai, Wei-Yue Liu, Bo Li, Hui Dai, Guang-Bing Li, Qi-Ming Lu, Yun-Hong Gong, Yu Xu, Shuang-Lin Li, Feng-Zhi Li, Ya-Yun Yin, Zi-Qing Jiang, Ming Li, Jian-Jun Jia, Ge Ren, Dong He, Yi-Lin Zhou, Xiao-Xiang Zhang, Na Wang, Xiang Chang, Zhen-Cai Zhu, Nai-Le Liu, Yu-Ao Chen, Chao-Yang Lu, Rong Shu, Cheng-Zhi Peng, Jian-Yu Wang, and Jian-Wei Pan. Satellite-based entanglement distribution over 1200 kilometers. *Science*, 356(6343):1140–1144, 2017.

[63] Ji-Gang Ren, Ping Xu, Hai-Lin Yong, Liang Zhang, Sheng-Kai Liao, Juan Yin, Wei-Yue Liu, Wen-Qi Cai, Meng Yang, Li Li, Kui-Xing Yang, Xuan Han, Yong-Qiang Yao, Ji Li, Hai-Yan Wu, Song Wan, Lei Liu, Ding-Quan Liu, Yao-Wu Kuang, Zhi-Ping He, Peng Shang, Cheng Guo, Ru-Hua Zheng, Kai Tian, Zhen-Cai Zhu, Nai-Le Liu, Chao-Yang Lu, Rong Shu, Yu-Ao Chen, Cheng-Zhi Peng, Jian-Yu Wang, and Jian-Wei Pan. Ground-to-satellite quantum teleportation. *Nature*, 549:70–73, 2017.

[64] T. Jennewein, J. P. Bourgoin, B. Higgins, C. Holloway, E. Meyer-Scott, C. Erven, B. Heim, Z. Yan, H. Hübel, G. Weihs, E. Choi, I. D'Souza, D. Hudson, and R. Laflamme. QEYSSAT: a mission proposal for a quantum receiver in space. volume 8997, 2014.

[65] Xiaoli Sun, D. Reusser, H. Dautet, and J. B. Abshire. Measurement of proton radiation damage to Si avalanche photodiodes. *IEEE Trans. Electron Devices*, 44(12):2160–2166, Dec 1997.

[66] Xiaoli Sun and H. Dautet. Proton radiation damage of Si APD single photon counters. In *Proceedings of Radiation Effects Data Workshop, IEEE*, pages 146–150, 2001.

[67] J.-P. Bourgoin, E. Meyer-Scott, B. L. Higgins, B. Helou, C. Erven, H. Hübel, B. Kumar, D. Hudson, I. D'Souza, R. Girard, R. Laflamme, and T. Jennewein. A comprehensive design and performance analysis of low earth orbit satellite quantum communication. *New J. Phys.*, 15:023006, 2013.

[68] Xiaoli Sun, Michael A. Krainak, James B. Abshire, James D. Spinhirne, Claude Trottier, Murray Davies, Henri Dautet, Graham R. Allan, Alan T. Lukemire, and James C. Vandiver. Space-qualified silicon avalanche-photodiode single-photon-counting modules. *J. Mod. Opt.*, 51(9-10):1333–1350, 2004.

[69] Yue Chuan Tan, Rakhitha Chandrasekara, Cliff Cheng, and Alexander Ling. Silicon avalanche photodiode operation and lifetime analysis for small satellites. *Opt. Express*, 21(14):16946–16954, Jul 2013.

[70] Elena Anisimova, Brendon L. Higgins, Jean-Philippe Bourgoin, Miles Cranmer, Eric Choi, Danya Hudson, Louis P. Piche, Alan Scott, Vadim Makarov, and Thomas Jennewein. Mitigating radiation damage of single photon detectors for space applications. *EPJ Quantum Technol.*, 4(10), 2017.

[71] J. S. Bell. On the problem of hidden variables in quantum mechanics. *Rev. Mod. Phys.*, 38:447–452, 1966.

[72] John F. Clauser, Michael A. Horne, Abner Shimony, and Richard A. Holt. Proposed experiment to test local hidden-variable theories. *Phys. Rev. Lett.*, 23:880–884, Oct 1969.

[73] Alain Aspect, Philippe Grangier, and Gérard Roger. Experimental Realization of Einstein-Podolsky-Rosen-Bohm Gedankenexperiment: A New Violation of Bell's Inequalities. *Phys. Rev. Lett.*, 49:91–94, Jul 1982.

[74] Charles H. Bennett, Gilles Brassard, Claude Crépeau, Richard Jozsa, Asher Peres, and William K. Wootters. Teleporting an unknown quantum state via dual classical and Einstein-Podolsky-Rosen channels. *Phys. Rev. Lett.*, 70:1895–1899, Mar 1993.

[75] A. Einstein, B. Podolsky, and N. Rosen. Can quantum-mechanical description of physical reality be considered complete? *Phys. Rev.*, 47:777–780, May 1935.

[76] ScienceDaily. https://www.sciencedaily.com/terms/quantum_entanglement.htm, 2018.

[77] Richard Cleve. Lecture notes in Quantum Information Processing (QIC710), September 2016.

[78] Wolfgang Tittel, Grégoire Ribordy, and Nicolas Gisin. Quantum cryptography. *Physics World*, 11(3):41, 1998.

[79] Charles H. Bennett, François Bessette, Louis Brassard, Gillesand Salvail, and John Smolin. Experimental quantum cryptography. *J. Cryptology*, 5(1):3–28, Jan 1992.

[80] B. C. Jacobs and J. D. Franson. Quantum cryptography in free space. *Opt. Lett.*, 21(22):1854–1856, Nov 1996.

[81] W. T. Buttler, R. J. Hughes, S. K. Lamoreaux, G. L. Morgan, J. E. Nordholt, and C. G. Peterson. Daylight quantum key distribution over 1.6 km. *Phys. Rev. Lett.*, 84:5652–5655, Jun 2000.

[82] Richard J Hughes, Jane E Nordholt, Derek Derkacs, and Charles G. Peterson. Practical free-space quantum key distribution over 10 km in daylight and at night. *New J. Physics*, 4(1):43, 2002.

[83] C. Kurtsiefer, P. Zarda, M. Halder, H. Weinfurter, P. M. Gorman, P. R. Tapster, and J. G. Rarity. Quantum cryptography: A step towards global key distribution. *Nature*, 419(6906):450, 2002.

[84] R. H. Hadfield. Single-photon detectors for optical quantum information applications. *Nat. Photonics*, 3:696–705, 2009.

[85] M. D. Eisaman, J. Fan, A. Migdall, and S. V. Polyakov. Invited review article: Single-photon sources and detectors. *Rev. Sci. Instrum.*, 82(7):071101, 2011.

[86] S. Cova, M. Ghioni, A. Lotito, I. Rech, and F. Zappa. Evolution and prospects for single-photon avalanche diodes and quenching circuits. *J. Mod. Opt.*, 51(9):1267–1288, 2004.

[87] A. A. M. Saleh. 9.4 - An investigation of laser wave depolarization due to atmospheric transmission. *IEEE J. Quantum Electron.*, 3(11):540–543, November 1967.

[88] Xiao-Song Ma, Thomas Herbst, Thomas Scheidl, Daqing Wang, Sebastian Kropatschek, William Naylor, Bernhard Wittmann, Alexandra Mech, Johannes Kofler, Elena Anisimova, Vadim Makarov, Thomas Jennewein, Rupert Ursin, and Anton Zeilinger. Quantum teleportation over 143 kilometres using active feed-forward. *Nature*, 489:269–273, 2012.

[89] Sandu Popescu. Bell's inequalities versus teleportation: What is nonlocality? *Phys. Rev. Lett.*, 72:797–799, Feb 1994.

[90] Jeongwan Jin, Sascha Agne, Jean-Philippe Bourgoin, Yanbao Zhang, Norbert Lütkenhaus, and Thomas Jennewein. Efficient time-bin qubit analyzer compatible with multimode optical channels. arXiv:quant-ph/1509.07490.

[91] Illionis wins NASA awards for three cubesat missions: https://aerospace.illinois.edu/news/illinois-wins-nasa-awards-three-cubesat-missions.

[92] Robert Bedington, Xueliang Bai, Edward Truong-Cao, Yue Chuan Tan, Kadir Durak, Aitor VillarZafra, James A. Grieve, Daniel KL Oi, and Alexander Ling. Nanosatellite experiments to enable future space-based QKD missions. *EPJ Quantum Technol.*, 3(1):12, Oct 2016.

[93] Kenneth R. Spring and Michael W. Davidson. Avalanche photodiodes. http://hamamatsu.magnet.fsu.edu/articles/avalanche.html.

[94] SparkFun Electronics. https://learn.sparkfun.com/tutorials/diodes/real-diode-characteristics.

[95] S. Cova, M. Ghioni, A. Lacaita, C. Samori, and F. Zappa. Avalanche photodiodes and quenching circuits for single-photon detection. *Appl. Opt.*, 35(12):1956–1976, 1996.

[96] O. Rubel and A. Darbandi. First-principle prediction of single-carrier avalanche multiplication in chalcopyrite semiconductors. *J. App. Phys.*, 113(20):203104, 2013.

[97] R. H. Haitz. Mechanisms contributing to the noise pulse rate of avalanche diodes. *J. Appl. Phys.*, 36:3123–3131, 1965.

[98] Yong-Su Kim, Youn-Chang Jeong, Sebastien Sauge, Vadim Makarov, and Yoon-Ho Kim. Ultra-low noise single-photon detector based on Si avalanche photodiode. *Rev. Sci. Instrum.*, 82(9):093110, 2011.

[99] E. Anisimova, D. Nikulov, S. S. Hu, M. Bourgon, R. Ursin, T. Jennewein, and V. Makarov. Low-noise single-photon detector for long-distance free-space quantum communication. 2015. (presented at Qcrypt 2015, Tokyo, Japan); manuscript in preparation.

[100] Yue Chuan Tan, Rakhitha Chandrasekara, Cliff Cheng, and Alexander Ling. Radiation tolerance of opto-electronic components proposed for space-based quantum key distribution. *J. Mod. Opt.*, 62(20):1709–1712, 2015.

[101] Wikipedia. https://en.wikipedia.org/wiki/South_Atlantic_Anomaly, 2018.

[102] A. H. Johnston. Radiation damage of electronic and optoelectronic devices in space. In *4th International Workshop on Radiation Effects on Semiconductor Devices for Space Applications*, 2000.

[103] SparkFun Electronics. https://www.spenvis.oma.be/.

[104] D. M. Sawyer and J. I. Vette. AP-8 trapped proton environment for solar maximum and solar minimum. Technical Report NASA-TM-X-72605, NASA Goddard Space Flight Center, 1976. https://ntrs.nasa.gov/search.jsp?R=19770012039.

[105] AP8MIN and AP8MAX Trapped Proton Models. https://creme.isde.vanderbilt.edu/CREME-MC/help/ap8min-and-ap8max-trapped-proton-models, 2018.

[106] TRIUMF. http://www.triumf.ca/, 2018.

[107] S. K. Joshi, Jacques Pienaar, Timothy C. Ralph, Luigi Cacciapuoti, Will McCutcheon, John Rarity, Dirk Giggenbach, Jin Gyu Lim, Vadim Makarov, Ivette Fuentes, Thomas Scheidl, Erik Beckert, Mohamed Bourennane, David Edward Bruschi, Adan Cabello, Jose Capmany, Alberto Carrasco-Casado, Eleni Diamanti, Miloslav Duusek, Dominique Elser, Angelo Gulinatti, Robert H. Hadfield, Thomas Jennewein, Rainer Kaltenbaek, Michael A. Krainak, Hoi-Kwong Lo, Christoph Marquardt, Gerard Milburn, Momtchil Peev, Andreas Poppe, Valerio Pruneri, Renato Renner, Christophe Salomon, Johannes Skaar, Nikolaos Solomos, Mario Stipčević, Juan P. Torres, Morio Toyoshima, Paolo Villoresi, Ian Walmsley, Gregor Weihs, Harald Weinfurter, Anton Zeilinger, Marek Żukowski, and Rupert Ursin. Space QUEST mission proposal: Experimentally testing decoherence due to gravity. 2018. arXiv:quant-ph/1703.08036.

[108] Eric L. Christiansen. Meteoroid/Debris Shielding. Technical Report NASA/TP-2003-210788, NASA Johnson Space Center, 2003. https://ntrs.nasa.gov/search.jsp?R=20030068423.

[109] Eric L. Christiansen, Kornel Nagy, Dana M. Lear, and Thomas G. Prior. Space station MMOD shielding. *Acta Astronaut.*, 65(7):921–929, 2009.

[110] Audun Nystad Bugge, Sebastien Sauge, Aina Mardhiyah M. Ghazali, Johannes Skaar, Lars Lydersen, and Vadim Makarov. Laser damage helps the eavesdropper in quantum cryptography. *Phys. Rev. Lett.*, 112:070503, Feb 2014.

[111] Jin Gyu Lim, Elena Anisimova, Brendon L. Higgins, Jean-Philippe Bourgoin, Thomas Jennewein, and Vadim Makarov. Laser annealing heals radiation damage in avalanche photodiodes. *EPJ Quantum Technol.*, 4(1):11, Jun 2017.

[112] Martin A. Green and Mark J. Keevers. Optical properties of intrinsic silicon at 300 K. *Prog. Photovolt. Res. Appl.*, 3:189–192, 1995.

[113] A. Yoshizawa, R. Kaji, and H. Tsuchida. A method of discarding after-pulses in single-photon detection for quantum key distribution. *Jpn. J. Appl. Phys.*, 41(10):6016–6017, 2002.

[114] A. Yoshizawa, R. Kaji, and H. Tsuchida. After-pulse-discarding in single-photon detection to reduce bit errors in quantum key distribution. *Opt. Express*, 11(11):1303–1309, Jun 2003.

[115] N. Sultana and T. Jennewein. A novel readout system for free-running negative feedback avalanche diodes to significantly suppress afterpulsing effect. 2016. (presented at Qcrypt 2016, Washington, D.C., U.S.A.); manuscript in preparation.

[116] J. R. Srour and J. M. McGarrity. Radiation effects on microelectronics in space. *Proc. IEEE*, 76(11):1443–1469, 1988.

[117] S. Sauge, L. Lydersen, A. Anisimov, J. Skaar, and V. Makarov. Controlling an actively-quenched single photon detector with bright light. *Opt. Express*, 19:23590–23600, 2011.

[118] Vadim Makarov, Jean-Philippe Bourgoin, Poompong Chaiwongkhot, Mathieu Gagné, Thomas Jennewein, Sarah Kaiser, Raman Kashyap, Matthieu Legré, Carter Minshull, and Shihan Sajeed. Creation of backdoors in quantum communications via laser damage. *Phys. Rev. A*, 94:030302, Sep 2016.

[119] V. Scarani, H. Bechmann-Pasquinucci, N. J. Cerf, M. Dušek, N. Lütkenhaus, and M. Peev. The security of practical quantum key distribution. *Rev. Mod. Phys.*, 81(3):1301–1350, 2009.

Appendix A

Laser Annealing Temperature Measurement

We measure the thermal resistance between the Single-Photon Avalanche photoDiode (SPAD) and the thermistor of SLiK-2, in order to estimate temperatures achieved by laser annealing. The thermistor mounted on the cold plate of the thermoelectric cooler (TEC) (see Fig. 5 in Ref. 117) allows us to measure the cold plate's temperature during the laser annealing process. Thus, by finding the thermal resistance between the SPAD and the cold plate, we can predict the actual temperature produced by each annealing power.

Alternatively, measuring V_{br} provides an indirect measure of an SPAD's temperature. This method is convenient because we can easily measure V_{br} with the experimental setup. Before measurements, we find the relationship between V_{br} and temperature by setting the TEC controller to temperatures from $-30\,^{\circ}\mathrm{C}$ to $20\,^{\circ}\mathrm{C}$ in $10\,^{\circ}\mathrm{C}$ increments and measuring V_{br} at each point. The fit line in Fig. A.1 shows that V_{br} linearly depends on temperature.

For the thermal resistance measurement, we turn off the TEC current but keep measuring thermistor temperature. We also vary the bias voltage over the range of 50 V to 90 V above V_{br} at room temperature. Such high bias voltages cause a high dark count rate, resulting in a constant current flow in the circuit. Consequently, the voltage across the SPAD is approximately V_{br} because of continuous quenching process, and V_{br} increases at high bias voltages owing to higher heat dissipation. When applying each bias voltage, we wait for the thermistor temperature to stabilize, and measure the voltage across the $1\,\mathrm{k}\Omega$ readout resistor in the passive quenching circuit (replacing R2 in Fig. 5.6 for more accurate avalanche current measurement). From this voltage value, we deduce V_{br} and the SPAD's power dissipation. Power dissipation of the SPAD is calculated by multiplying the avalanche current (on the order of a few hundred µA) and V_{br}. Using the linear relationship found in Fig. A.1, we find the SPAD's temperature and compare it to the thermistor temperature. The temperature difference divided by the SPAD's power dissipation gives

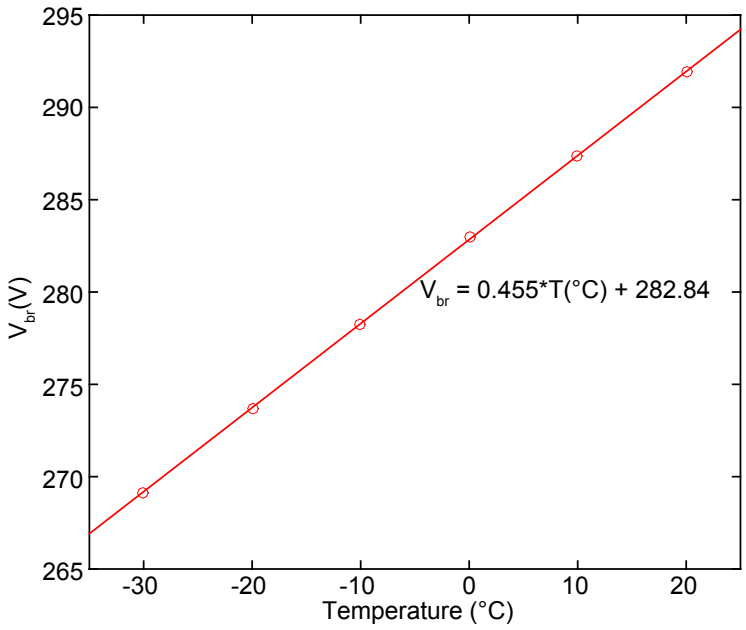

Figure A.1: **Breakdown voltage (V_{br}) of SLiK-2 at various temperatures.** The relationship between V_{br} and temperature is linear. The coefficient of determination, R^2, is 0.99994.

Table A.1: **Measurement of thermal resistance between SPAD and cold plate.**

V_{bias} (V)	V_{br} (V)	ΔT (°C)	Power dissipation (mW)	Thermal resistance ($\mathrm{K\,W^{-1}}$)
340	294.65	−0.16	33.4	−4.8
350	295.05	−0.44	40.5	−10.8
360	295.82	0.11	47.4	2.3
370	296.74	0.98	54.3	18.0
380	297.10	0.54	61.5	8.8

us the thermal resistance. Table A.1 summarizes thermal resistance test results. Although the results are somewhat noisy, making it difficult to find the exact thermal resistance, it is clear that the thermal resistance is sufficiently small that the thermistor temperature approximately matches that of the SPAD itself. This assumption is used to estimate laser annealing temperature in conjunction with SLiK-1's thermistor temperature measurements during laser annealing procedure.

Our passive quenching circuit is designed to have the Single-Photon Avalanche photoDiode (SPAD) reverse-biased only, but if it can be forward-biased during the laser annealing procedure, the temperature of the SPAD can be directly explored by checking the IV curve. The forward bias current follows

$$I_F \sim e^{\frac{qV_d}{k_B T}} \tag{A.1}$$

where q is the electric charge, V_d the diode voltage, k_B the Boltzmann constant, and T the diode temperature. By keeping the same forward diode voltage for different laser illumination powers and measuring the corresponding output forward current, the diode temperature (T) can be accurately found.